

DOT/FAA/PM-87-28

**Project Report
ATC-149**

Clutter Suppression for Doppler Weather Radars with Multirate Sampling Schemes

M. Goldberg

11 December 1990

Lincoln Laboratory
MASSACHUSETTS INSTITUTE OF TECHNOLOGY
LExINGTON, MASSACHUSETTS



Prepared for the Federal Aviation Administration,
Washington, D.C. 20591

This document is available to the public through
the National Technical Information Service,
Springfield, VA 22161

This document is disseminated under the sponsorship of the Department of Transportation in the interest of information exchange. The United States Government assumes no liability for its contents or use thereof.

1. Report No. ATC-149		2. Government Accession No. DOT/FAA/PM-87-28		3. Recipient's Catalog No.	
4. Title and Subtitle Clutter Suppression for Doppler Weather Radars with Multirate Sampling Schemes				5. Report Date 11 December 1990	
				6. Performing Organization Code	
7. Author(s) Marc Goldberg				8. Performing Organization Report No. ATC-149	
9. Performing Organization Name and Address Lincoln Laboratory, MIT P.O. Box 73 Lexington, MA 02173-9108				10. Work Unit No. (TRAIS)	
				11. Contract or Grant No. DTFA-01-L-83-4-10579	
12. Sponsoring Agency Name and Address Department of Transportation Federal Aviation Administration Systems Research and Development Service Washington, DC 20591				13. Type of Report and Period Covered Project Report	
				14. Sponsoring Agency Code	
15. Supplementary Notes This report is based on studies performed at Lincoln Laboratory, a center for research operated by Massachusetts Institute of Technology under Air Force Contract F19628-90-C-0002					
16. Abstract Reliable weather parameter estimates are required of radars such as the Terminal Doppler Weather Radar (TDWR) — a Federal Aviation Administration project — which will automatically detect hazardous weather phenomena in the vicinity of an airport. Velocity and range aliasing will degrade the quality of these estimates, as will contamination by ground clutter. For radars which operate at short ranges and at low elevation angles, as the TDWR will to detect windshears at the airport surface, clutter contamination is an especially severe problem. Multirate pulse trains — pulse trains containing multiple intersample spacings — can extend both the unambiguous velocity and range of a Pulsed Doppler Radar beyond those afforded by pulse trains with a constant intersample spacing; but the usual properties of conventional clutter filter architectures change radically when applied to data collected with a multirate sampling scheme. A brief introduction to the systems and weather considerations for Doppler Weather Radars is provided and the Pulse-Pair spectral moment estimators are presented. This introduction is followed by a discussion of frequency domain clutter rejection techniques for Batch PRT (Pulse Repetition Time) sequences — blocks of equispaced samples with the PRT alternating from block to block. The main topic of the report is clutter suppression for Staggered PRT sequences in which the PRT alternates from pulse to pulse. The Staggered PRT scheme has the advantage over the Batch PRT scheme of spatial coherency for estimates of the radar return signal's autocorrelation function at the lags corresponding to the two PRT's. A time-varying filter architecture with multiple transfer functions is presented and analyzed, and its interaction with the Pulse-Pair estimators is explored. Three design techniques for Staggered PRT filters are described and assessed in the context of clutter suppression. The final section of the report summarizes the results for the Batch and Staggered PRT schemes and provides suggestions for further research.					
17. Key Words TDWR staggered PRT clutter filtering velocity dealiasing filter design Doppler weather radars multirate sampling			18. Distribution Statement Document is available to the public through the National Technical Information Service, Springfield, VA 22161.		
19. Security Classif. (of this report) Unclassified		20. Security Classif. (of this page) Unclassified		21. No. of Pages 136	22. Price

Abstract

Reliable weather parameter estimates are required of radars such as the Terminal Doppler Weather Radar (TDWR) – a Federal Aviation Administration project – which will automatically detect hazardous weather phenomena in the vicinity of an airport. Velocity and range aliasing will degrade the quality of these estimates, as will contamination by ground clutter. For radars which operate at short ranges and at low elevation angles, as the TDWR will to detect windshears at the airport surface, clutter contamination is an especially severe problem. Multirate pulse trains – pulse trains containing multiple intersample spacings – can extend both the unambiguous velocity and range of a Pulsed Doppler Radar beyond those afforded by pulse trains with a constant intersample spacing; but the usual properties of conventional clutter filter architectures change radically when applied to data collected with a multirate sampling scheme.

A brief introduction to the systems and weather considerations for Doppler Weather Radars is provided and the *Pulse-Pair* spectral moment estimators are presented. This introduction is followed by a discussion of frequency domain clutter rejection techniques for Batch PRT (Pulse Repetition Time) sequences – blocks of equispaced samples with the PRT alternating from block to block. The main topic of the report is clutter suppression for Staggered PRT sequences in which the PRT alternates from pulse to pulse. The Staggered PRT scheme has the advantage over the Batch PRT scheme of spatial coherency for estimates of the radar return signal's autocorrelation function at the lags corresponding to the two PRT's. A time-varying filter architecture with multiple transfer functions is presented and analyzed; and its interaction with the Pulse-Pair estimators is explored. Three design techniques for Staggered PRT filters are described and assessed in the context of clutter suppression.

The final section of the report summarizes the results for the Batch and Staggered PRT schemes and provides suggestions for further research.

Acknowledgements

The author benefited from discussions with several people in the course of preparing this report. At Lincoln Laboratory, Dr. James Evans provided countless valuable insights and suggestions, while discussions with Dr. Les Novak contributed to the development of section 4.3. Useful discussions were also held with Dr. Dusan Zrnić of the National Severe Storms Laboratory and Mr. Zoran Banjanin of the Cooperative Institute for Mesoscale Meteorological Studies at the University of Oklahoma.

The author is grateful to Messrs. Paul Biron, Robert Hallowell, Mark Isaminger and J. Patrick Sanford, all of Lincoln Laboratory, for compiling the gust front spectrum width data presented in Appendix A.

Table of Contents

Abstract	iii
Acknowledgements	v
List of Illustrations	ix
List of Tables	xiii
List of Acronyms	xv
1.0 INTRODUCTION	1
1.1 Background	1
1.2 Doppler Power Spectrum and Pulse-Pair Estimators	2
1.3 Weather Characteristics	4
1.4 Range De-Aliasing	7
1.5 Velocity De-Aliasing	9
1.6 Absolute Velocity De-Aliasing	9
1.7 The Clutter Challenge	12
1.8 Summary of the Issues and Outline of the Report	12
2.0 CLUTTER SUPPRESSION FOR BATCH PRT SEQUENCES	15
2.1 Data Taper Selection for Frequency Domain Clutter Suppression	17
3.0 CLUTTER SUPPRESSION FOR STAGGERED PRT SEQUENCES	25
3.1 Staggered PRT Filter Structure	25
3.2 Staggered PRT Filter Response	30
3.2.1 Average Power Transfer Function	31
3.2.2 Convolutions of Staggered PRT Sequences	32
3.2.3 Lag c_1 and Lag c_2 Power Transfer Functions	34
3.3 Properties of the $C_i(z)$ and Effective Power Transfer Functions	37
3.3.1 Z-Plane Zero Distribution of $ G(\omega) ^2$	37
3.3.2 Phase Responses of $C_0^*(e^{j\omega\delta_T})C_1(e^{j\omega\delta_T})$ and $C_0(e^{j\omega\delta_T})C_1^*(e^{j\omega\delta_T})$	37
3.3.3 Uncontrollable Zeroes in the $C_i(z)$	54
4.0 STAGGERED PRT FILTER DESIGN TECHNIQUES	75
4.1 Design Technique: Coefficient Selection	75
4.2 Design Technique: Maximally Flat Response	87
4.3 Design Technique: Output Signal to Clutter Ratio Maximization	93
5.0 CONCLUSIONS	106

5.1 Batch PRT	106
5.2 Staggered PRT	107
5.3 Further Research	108
APPENDIX A: GUST FRONT SPECTRUM WIDTH DATA	116
REFERENCES	118

List of Illustrations

Figure		Page
1.1	Unambiguous doppler velocity versus unambiguous range	3
1.2a	Standard deviation of pulse-pair velocity estimate	5
1.2b	Standard deviation of pulse-pair spectrum width estimate	6
1.3	Vertical profile of 1° beam at 0.5° elevation versus ground range	8
1.4	Velocity de-aliasing with multiple sample rates	11
2.1	Batch PRT sampling scheme	16
2.2	Clutter rejection via the windowed periodogram, 33 point window	19
2.3	Clutter rejection via the windowed periodogram, 25 point window	21
2.4	Clutter rejection via the windowed periodogram, 17 point window	23
2.5	Clutter rejection via the windowed periodogram, 17 point window	24
3.1	Staggered PRT sampling scheme	26
3.2	Staggered PRT intersample delays	27
3.3	Staggered PRT filter architecture	29
3.4	$ G(\omega) ^2$ for a staggered PRT filter, $N=3$	40
3.5	Magnitude and phase functions for $C_0C_1^*$, $N=3$	41
3.6	$ G(\omega) ^2$ for a staggered PRT filter, $N=4$	42
3.7	Magnitude and phase functions for $C_0C_1^*$, $N=4$	43
3.8a	$ G(\omega) ^2$ for an OSCRM design, $c_1=1$, $c_2=2$ and $N=2$	45
3.8b	Lag c_1 transfer function for OSCRM design of figure 3.8a	46
3.9a	Uncorrected lag c_1 and c_2 velocity estimates from filter of figure 3.8, $\sigma_v=1$ m/s	47
3.9b	Corrected lag c_1 and c_2 velocity estimates from filter of figure 3.8, $\sigma_v=1$ m/s	48
3.10	Errors in final de-aliased estimates generated from lag c_1 and c_2 estimates of figure 3.9b, $\sigma_v=1$ m/s	49

3.11	Lag c_1 transfer function for OSCR design, $c_1=2$, $c_2=3$ and $N=4$	51
3.12	"Corrected" lag c_1 and c_2 velocity estimates from filter of figure 3.11, $\sigma_v=1$ m/s	52
3.13	Errors in final de-aliased estimates generated from lag c_1 and c_2 estimates of figure 3.12, $\sigma_v=1$ m/s	53
3.14a	Z-Plane zeroes of $ G(\omega) ^2 - c_1=2$, $c_2=3$, $N=3$ and all controllable zeroes at $z=1$	56
3.14b	$ G(\omega) ^2 - c_1=2$, $c_2=3$, $N=3$ and all controllable zeroes at $z=1$	57
3.15a	Z-Plane zeroes of $ G(\omega) ^2 - c_1=3$, $c_2=4$, $N=3$ and all controllable zeroes at $z=1$	58
3.15b	$ G(\omega) ^2 - c_1=3$, $c_2=4$, $N=3$ and all controllable zeroes at $z=1$	59
3.16a	Z-Plane zeroes of $ G(\omega) ^2 - c_1=5$, $c_2=6$, $N=3$ and all controllable zeroes at $z=1$	60
3.16b	$ G(\omega) ^2 - c_1=5$, $c_2=6$, $N=3$ and all controllable zeroes at $z=1$	61
3.17a	Z-Plane zeroes of $ G(\omega) ^2 - c_1=5$, $c_2=7$, $N=3$ and all controllable zeroes at $z=1$	63
3.17b	Z-Plane zeroes of $ G(\omega) ^2 - c_1=5$, $c_2=7$, $N=4$ and all controllable zeroes at $z=1$	64
3.17c	Z-Plane zeroes of $ G(\omega) ^2 - c_1=5$, $c_2=7$, $N=5$ and all controllable zeroes at $z=1$	65
3.17d	Z-Plane zeroes of $ G(\omega) ^2 - c_1=5$, $c_2=7$, $N=6$ and all controllable zeroes at $z=1$	66
3.17e	Z-Plane zeroes of $ G(\omega) ^2 - c_1=5$, $c_2=7$, $N=7$ and all controllable zeroes at $z=1$	67
3.17f	Z-Plane zeroes of $ G(\omega) ^2 - c_1=5$, $c_2=7$, $N=8$ and all controllable zeroes at $z=1$	68
3.18a	$ G(\omega) ^2$ versus Doppler velocity - $c_1=5$, $c_2=7$, $N=3$ and all controllable zeroes at $z=1$	69
3.18b	$ G(\omega) ^2$ versus Doppler velocity - $c_1=5$, $c_2=7$, $N=4$ and all controllable zeroes at $z=1$	70

3.18c	$ G(\omega) ^2$ versus Doppler velocity - $c_1=5, c_2=7, N=5$ and all controllable zeroes at $z=1$	71
3.18d	$ G(\omega) ^2$ versus Doppler velocity - $c_1=5, c_2=7, N=6$ and all controllable zeroes at $z=1$	72
3.18e	$ G(\omega) ^2$ versus Doppler velocity - $c_1=5, c_2=7, N=7$ and all controllable zeroes at $z=1$	73
3.18f	$ G(\omega) ^2$ versus Doppler velocity - $c_1=5, c_2=7, N=8$ and all controllable zeroes at $z=1$	74
4.1	Equispaced FIR clutter filter impulse response, M odd	78
4.2a	Z-Plane zeroes of squared-magnitude response for 17 point equispaced FIR filter	80
4.2b	Squared-Magnitude response for 17 point equispaced FIR filter	81
4.3a	Z-Plane zeroes of $ G(\omega) ^2$ for coefficient selection design - $c_1=3, c_2=5$ and $N=5$	82
4.3b	$ G(\omega) ^2$ for coefficient selection design - $c_1=3, c_2=5$ and $N=5$	83
4.4a	Z-Plane zeroes of $ G(\omega) ^2$ for coefficient selection design - $c_1=2, c_2=4$ and $N=6$	84
4.4b	$ G(\omega) ^2$ for coefficient selection design - $c_1=2, c_2=4$ and $N=6$	85
4.5a	Z-Plane zeroes of $ G(\omega) ^2$ for MFR design - $c_1=4, c_2=5$ and $N=6$	88
4.5b	$ G(\omega) ^2$ for MFR design - $c_1=4, c_2=5$ and $N=6$	89
4.5c	$ G(\omega) ^2$ for MFR design - $c_1=4, c_2=5$ and $N=6$	90
4.6	$ G(\omega) ^2$ for MFR design - $c_1=4, c_2=5$ and $N=10$	92
4.7	Doppler domain input parameters for OSCRM design technique	96
4.8a	Z-Plane zeroes of $ G(\omega) ^2$ for OSCRM design - $c_1=2, c_2=3$ and $N=3$	97
4.8b	$ G(\omega) ^2$ for OSCRM design - $c_1=2, c_2=3$ and $N=3$	98
4.9	Distributed clutter rejection for OSCRM design of figure 4.8	100
4.10	Discrete clutter rejection for OSCRM design of figure 4.8	101

4.11a	Reflectivity estimate bias for OSCRM design of figure 4.8 - $\sigma_v = 4$ m/s	102
4.11b	Reflectivity estimate bias for OSCRM design of figure 4.8 - $\sigma_v = 7$ m/s	103
4.12	$ G(\omega) ^2$ for OSCRM design - $c_1=5$, $c_2=7$ and $N=3$	104
5.1	Sample association for composite pulse sequence - $c_1=2$, $c_2=3$ and $d_e=3$	110
5.2	Composite filter transfer functions - $c_1=2$, $c_2=3$, $d_e=3$, $N=3$ and an equispaced filter with 29 coefficients	111
5.3	Composite filter structure for velocity estimation	112
5.4	Combining staggered and equispaced velocity estimates	114
5.5	Velocity estimate errors for composite filter of figure 5.2, $\sigma_v=1$ m/s, lag c_1 and c_2 transfer functions replaced by $ G(\omega) ^2$	115

List of Tables

Table		Page
3.1	Values of l satisfying equation 3.5	33
3.2	Folding table: $c_1=2$, $c_2=3$ and $v_u=1$ m/s	44
A.1	Gust front spectrum width data	116

List of Acronyms

dBZ	Effective reflectivity factor expressed in decibels
DFT	Discrete Fourier Transform
FAA	Federal Aviation Administration
FIR	Finite Impulse Response
FL-2	FAA-Lincoln S-Band Doppler weather radar testbed
GHz	Gigahertz
Hz	Hertz
IDFT	Inverse Discrete Fourier Transform
IIR	Infinite Impulse Response
LCM	Least Common Multiple
MFR	Maximally Flat Response
NSSL	National Severe Storms Laboratory
OSCRM	Output Signal-to-Clutter Ratio Maximization
PRF	Pulse Repetition Frequency
PRT	Pulse Repetition Time
RPM	Revolutions per Minute
SCR	Signal-to-Clutter Ratio
SNR	Signal-to-Noise Ratio
TDWR	Terminal Doppler Weather Radar

1.0 INTRODUCTION

Reliable weather parameter estimates are required of radars such as the Terminal Doppler Weather Radar (TDWR) – a Federal Aviation Administration project – which will automatically detect hazardous weather phenomena in the vicinity of an airport. Velocity and range aliasing will degrade the quality of these estimates, as will contamination by ground clutter. For radars which operate at short ranges and at low elevation angles, as the TDWR will to detect windshears at the airport surface, clutter contamination is an especially severe problem. Multirate pulse trains – pulse trains containing multiple intersample spacings – can extend both the unambiguous velocity and range of a Pulsed Doppler Radar beyond those afforded by pulse trains with a constant intersample spacing; but the usual properties of conventional clutter filter architectures change radically when applied to data collected with a multirate sampling scheme. The topics of this report are clutter suppression techniques for multirate pulse sequences and their interaction with the estimation of weather parameters.

1.1 BACKGROUND

The spatial scale for the discrete weather phenomena of interest in the TDWR system ranges from tens of kilometers, in the case of gust fronts, to sub-kilometer scales for wind shear events such as microbursts or for tornadoes. Sub-kilometer resolution within 50 km of the radar requires a beamwidth on the order of 1° . A 1° conical beam corresponds to a parabolic, axially-fed, antenna whose diameter is 10 m at S-Band (3 GHz) and 5 m at C-band (6 GHz). The requirements for angular resolution of the weather radar serve to bound the radar frequency from below. As the radar frequency is decreased below S-Band, it becomes increasingly difficult and costly to manufacture both the reflector and a pedestal capable of executing appropriate scanning strategies, due to the increased size and inertia of the antenna. Frequency bands below S-Band are not practical for most ground-based weather radar applications.

The radar frequency is bounded from above by considerations of atmospheric attenuation of the radar signal, as it would be unacceptable for storms near the radar to block the view of storms farther away from the radar. If the two-way path loss due to atmospheric attenuation is to be held below, say, 5 dB, the radar frequency must not exceed 7 GHz [Nathanson69a]. So, weather radars for applications such as TDWR are either C-Band or S-Band devices. An additional constraint on the radar frequency is the availability of frequency allocations – C-Band is currently the preferred option for TDWR in this context.

For Doppler weather radars transmitting an equispaced pulse train, the Pulse Repetition Time (PRT), or intersample period, determines the radar's maximum unambiguous range r_u and Nyquist velocity v_u . Denoting the speed of light by c , the PRT by δ_T , and the radar wavelength by λ , the following expressions for r_u and

v_u may be easily derived.

$$v_u = \frac{\lambda}{4\delta_T} \quad \text{and} \quad r_u = \frac{c\delta_T}{2}$$

Combining these two expressions to eliminate δ_T , we obtain

$$v_u r_u = \frac{c\lambda}{8} \tag{1.1}$$

Equation 1.1 represents the fundamental relationship between Nyquist velocity and unambiguous range as a function of radar frequency. Figure 1.1 provides a graph of this relationship for radar frequencies of 3 GHz and 6 GHz.

1.2 DOPPLER POWER SPECTRUM AND PULSE-PAIR ESTIMATORS

The Doppler power spectrum of a radar resolution cell represents the aggregate statistics of the literally millions of hydrometeors or other particulates within that volume. The average horizontal velocity of these particulates is approximately the horizontal windspeed. A combination of spectral broadening mechanisms including shear within the resolution volume, turbulence, scan modulation by the antenna pattern and the distribution of particle sizes results in a Doppler spectrum with Gaussian shape

$$S_w(v) \triangleq \frac{S}{\sqrt{2\pi}\sigma_v} e^{-(v-\bar{v})^2/2\sigma_v^2} \tag{1.2a}$$

and its Fourier Transform partner, the weather autocorrelation function

$$R_w(m\delta_T) = S e^{-8\left(\pi\sigma_v m\delta_T/\lambda\right)^2} e^{-j\left(4\pi\bar{v}m\delta_T/\lambda\right)} \tag{1.3a}$$

evaluated at lag m , where \bar{v} is the mean Doppler velocity, σ_v is the spectrum's standard deviation or *spectrum width*, and S is the power of the weather echo process.

The three spectral parameters of interest in weather radar applications are the first three moments of the Doppler power spectrum: the power S , which is related to the liquid water density in the atmosphere; the mean velocity \bar{v} ; and the spectrum width σ_v which is an indicator of atmospheric turbulence. Frequency domain estimation of these parameters is rarely employed, since the small number of samples per azimuth (typically ≈ 50) offers poor frequency resolution and since peak-finding algorithms are generally sensitive to estimation errors resulting from measurement noise (which is not included in equation 1.2). Instead, time domain estimation of the spectral parameters is employed via the autocorrelation function. These estimators were initially developed in the late 1960's [Miller70a] and are commonly referred to as *pulse-pair* estimators. One version of these estimators makes use of the autocorrelation at lags zero and one, only, and is referred to as the 0/1 estimator. It is

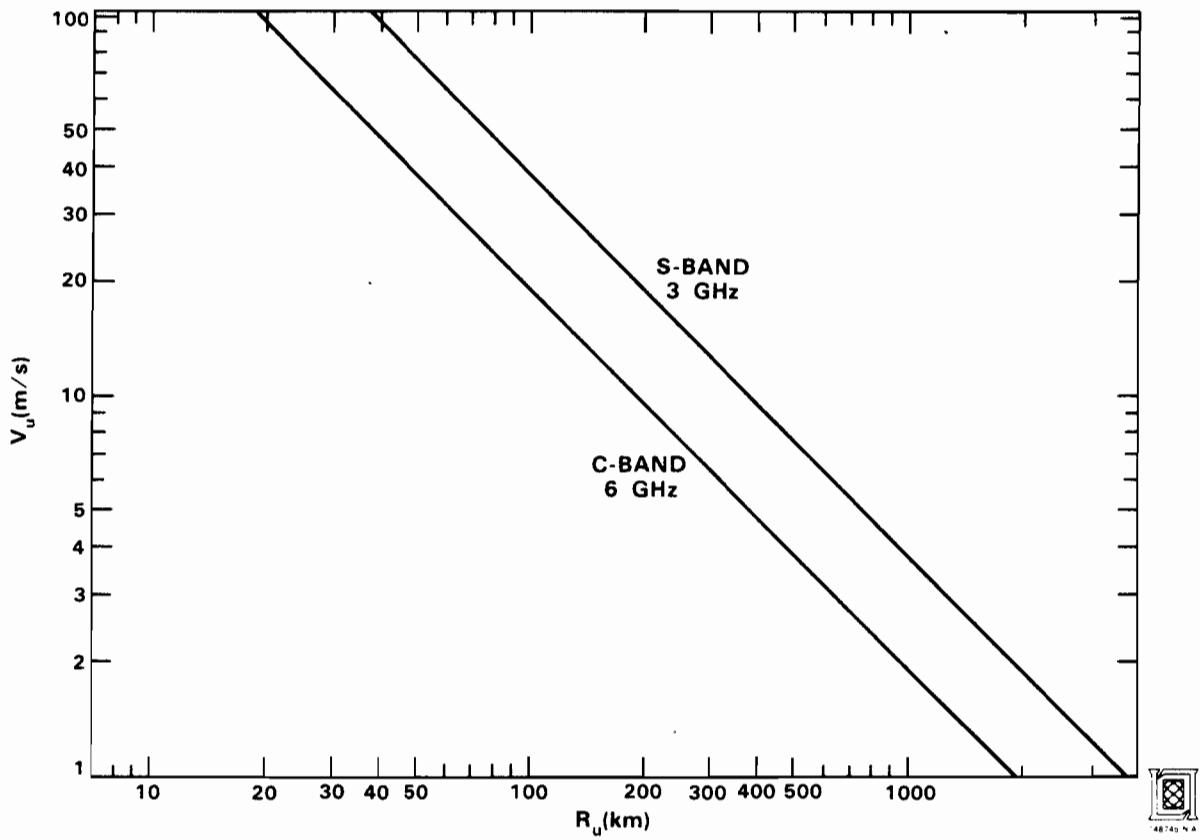


Figure 1.1: Unambiguous doppler velocity versus unambiguous range

given by equations 1.4 [Doviak84a] .

$$\hat{R}_w(0) \triangleq \hat{R}_t(0) - \frac{N_s}{2} ; \hat{R}_w(\delta_T) \triangleq \hat{R}_t(\delta_T) \quad (1.4a)$$

$$\hat{S} \triangleq \hat{R}_w(0) \quad (1.4b)$$

$$\hat{v} \triangleq \frac{-\lambda}{4\pi\delta_T} \arg[\hat{R}_w(\delta_T)] \quad (1.4c)$$

$$\hat{\sigma}_v \triangleq \frac{\lambda}{2\sqrt{2}\pi\delta_T} \left| \ln \left[\frac{\hat{R}_w(0)}{|\hat{R}_w(\delta_T)|} \right] \right|^{1/2} \operatorname{sgn} \left\{ \ln \left[\frac{\hat{R}_w(0)}{|\hat{R}_w(\delta_T)|} \right] \right\} \quad (1.4d)$$

In these equations, $\hat{R}_t(0)$ and $\hat{R}_t(\delta_T)$ represent the estimated autocorrelation at lags zero and one of the total received signal – consisting of weather signal plus system noise – and $N_s/2$ is the variance of the system noise. The system noise is assumed to be white and independent of the weather returns. $N_s/2$ is a measurable quantity. These estimators are popular for weather radar applications, as their implementation is straightforward.

Figures 1.2a and 1.2b [Doviak84a] display the standard deviations of the estimators of equations 1.4c and 1.4d, respectively, in the absence of Nyquist aliasing. The abscissa is normalized spectrum width, $\sigma_v/2v_u$, the ordinate is the standard deviation of the estimate normalized by the Nyquist interval and the number of pulse pairs per dwell time, M . The curves in the figures are parameterized by Signal-to-Noise ratio (SNR) – 10 dB is a representative figure for a radar such as the TDWR.

As an S-Band example, consider the case where $\lambda=10$ cm , $\sigma_v=6$ m/s, $\delta_T=2$ ms ($\sigma_v/2v_u \approx 0.25$), an azimuth dwell time of 50 ms and an SNR of 20 dB. Figure 1.2a indicates a standard deviation of 2.0 m/s – almost one-tenth of the Nyquist interval – for estimates of \hat{v} ; while Figure 1.2b indicates a standard deviation of 1.1 m/s for the estimate of $\hat{\sigma}_v$. Note that with $\text{SNR} \geq 0$ dB, these standard deviations increase rapidly as the spectrum width increases beyond $0.5v_u$. δ_T should be selected so that $v_u \geq 2\sigma_v$ for all spectrum widths at which reliable Doppler estimates are required.

1.3 WEATHER CHARACTERISTICS

The radar signatures of meteorological phenomena are diverse. Stratiform precipitation may produce nearly uniform reflectivity and velocity fields with small spectrum width values. Tornado signatures are often evident in all three fields: a hook-shaped increased reflectivity due to spiraling inflow of precipitation and airborne debris; high values of spectrum width; and a velocity vortex signature if the tornado is within 50 km of the radar. The signatures of thunderstorm outflow events such as the microburst and gustfront are most prominent in the velocity and spectrum

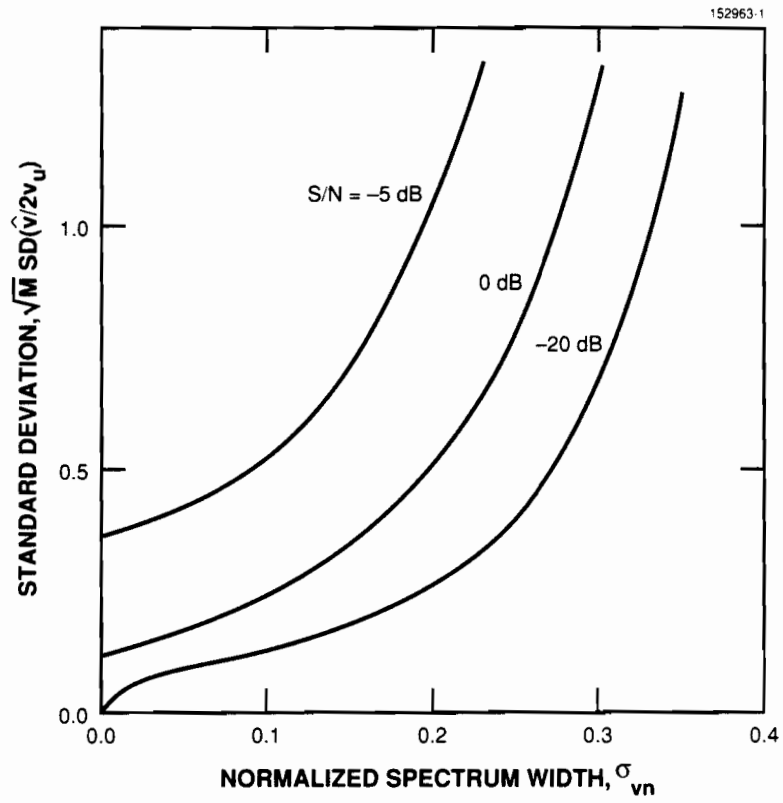


Figure 1.2a: Standard deviation of pulse-pair velocity estimate

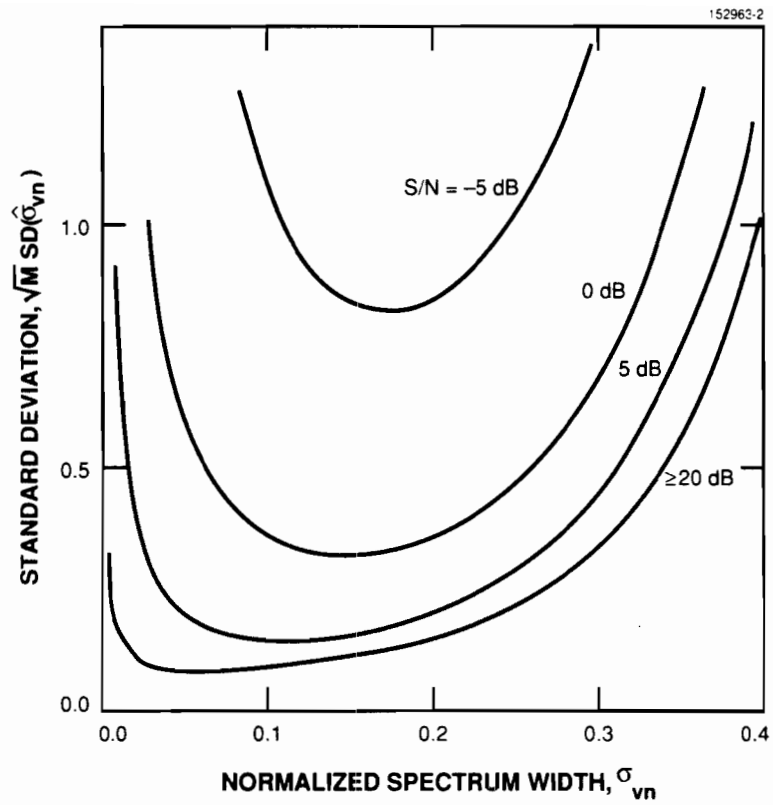


Figure 1.2b: Standard deviation of pulse-pair spectrum width estimate

width fields [Uyeda85a] .

The microburst and gustfront are the two most frequent types of low-altitude windshears at airports; their signatures must be discernible in TDWR Doppler measurements. Typical spectrum widths in microburst outflows may be on the order of 2 m/s [Rinehart87a] . The spectrum widths associated with gustfronts are larger than for the microburst – in Appendix A, we recommend a design value of 6 m/s in this context. In light of the discussion in section 1.2, accurate (*i.e.* standard deviations ≈ 2 m/s) Doppler measurements of gustfronts will require a v_u of at least 12 m/s. This corresponds to minimum PRF's of 480 Hz and 960 Hz at S and C-Bands ($\lambda=0.1$ m and $\lambda=0.05$ m), respectively. These minimum PRF's yield maximum r_u 's of 312 km and 156 km.

It has been proposed that the TDWR be sited within 15 km of its associated airport and utilize elevation angles as low as 0.5° to detect shear phenomena [Merritt87a] . Figure 1.3 depicts the altitude coverage of a 1° beam – at an elevation angle of 0.5° – as a function of ground range. Now, regions of significant reflectivity (*e.g.* ≥ 30 dBZ) in North America may extend vertically to as much as 14 km or 45,000 ft in altitude [Vasiloff84a, Wilk80a] . The import of the unambiguous range figure r_u is that the apparent range of any target at true range r_t will be $r_t \bmod r_u$. It is apparent from figure 1.3 that phenomena with significant reflectivity will be sensed beyond 450 km – with a 0.5° elevation angle – and that they may overlay or *obscure* targets within the unambiguous range interval r_u . The former targets are referred to as *out-of-trip* targets or *out-of-trip* weather. Obscuration by *out-of-trip* weather severely limits the radar's detection capability for *in-trip* hazards with low reflectivity such as gustfronts or microbursts in the American high-plains regions [Fujita85a] .

The minimum PRF's above, based on considerations of estimate accuracy, are not low enough to avoid obscuration by *out-of-trip* weather. Nor are they high enough to ensure unambiguous Doppler velocity estimates. Peak microburst windspeeds of 33 m/s, for example, have been observed [Fujita85a] ; and windspeeds associated with tornadic activity may be as high as 90 m/s [Doviak84a] . Pulsed Doppler Weather Radars operating at S and C-Bands must contend with degrees of both range obscuration and velocity aliasing.

1.4 RANGE DE-ALIASING

Range obscuration is difficult to predict in advance of actual measurements; and no satisfactory techniques exist for removing the effects of obscuration by post-processing of the measured data. Adaptive PRT selection and random phase coding of the pulse train are two methods for combatting obscuration.

In the former case, a rapid surveillance scan with a large PRT (large r_u) is employed to unambiguously acquire regions of reflectivity. This information is used

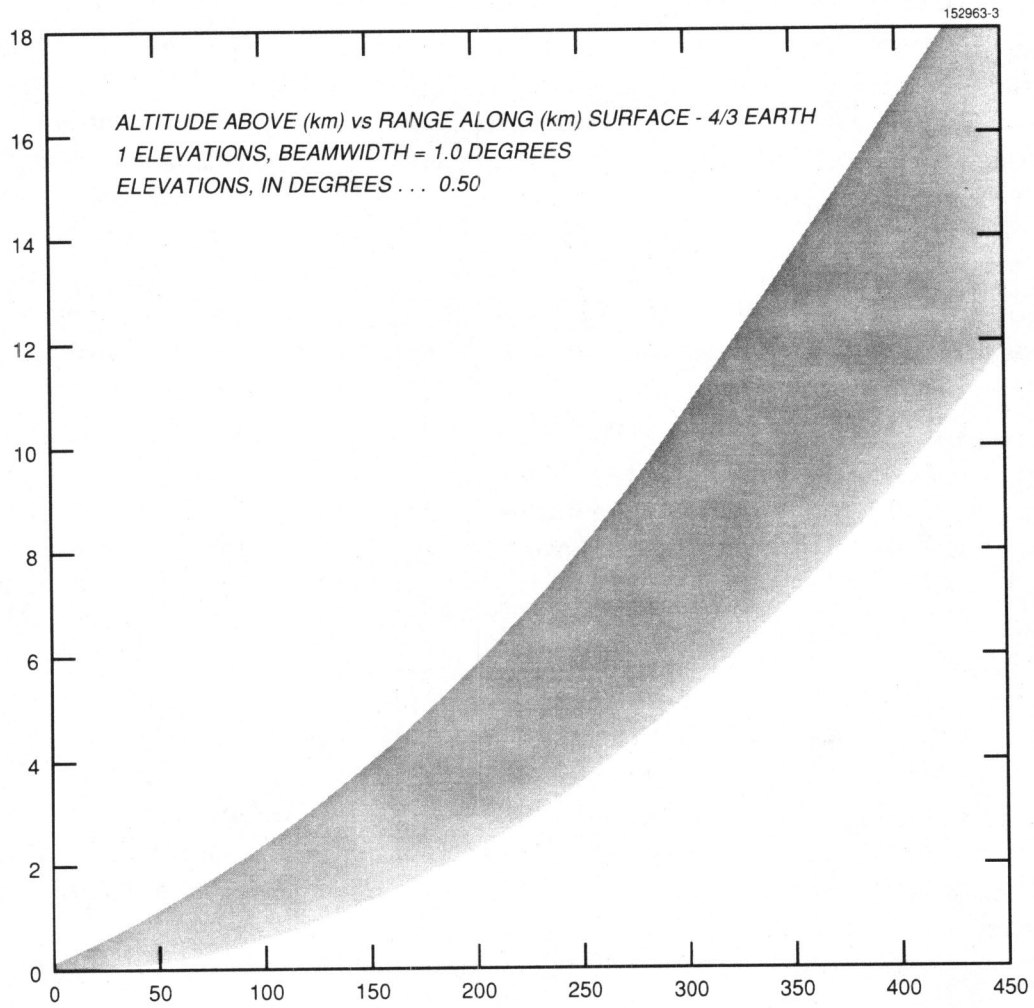


Figure 1.3: Vertical profile of 1° beam at 0.5° elevation versus ground range

to select the PRT for a subsequent weather collection scan. Random phase coding, on the other hand, whitens the received signal component due to the out-of-trip weather, at the expense of decreasing the effective SNR for the in-trip weather.

1.5 VELOCITY DE-ALIASING

The need to free radar velocity data from ambiguities is especially critical if the data are to be processed by automated algorithms. Unlike range obscuration, however, techniques do exist for "de-aliasing" aliased velocity estimates.

There are two general approaches to velocity de-aliasing. The first approach, *relative de-aliasing*, invokes assumptions of local radial and azimuthal continuity in processing the measured velocity field. As an example, imagine a radar with $v_u = 10$ m/s. Suppose that a radial of velocity measurements has just become available. Suppose further that the first hundred range gates have velocity values of 8 to 10 m/s, and that the 101st gate's velocity value is -9 m/s. The logic of radial continuity would declare that a velocity alias had occurred and reset the value of -9 m/s to 11 m/s. Azimuthal continuity operates in an analogous fashion.

Relative de-aliasing produces a velocity field containing extended regions which differ from the "true" Doppler velocity field by an additive constant equal to some multiple of the Nyquist interval length, $2v_u$. The second approach to velocity de-aliasing, *absolute de-aliasing*, attempts to generate an estimate of the "true" Doppler windfield. This can be achieved by the use of pulse trains with multiple PRT's. The mechanism of absolute de-aliasing will be discussed subsequently.

For the identification of phenomena whose discriminant is spatial variations in the velocity field, relative de-aliasing of that field is sufficient; relative de-aliasing produces a datafield whose spatial "gradient" locally matches that of the true Doppler velocity field. This class of phenomena includes the microburst and other shear events. Absolutely de-aliased velocity estimates are required when the velocity data is used directly – as in the *Sectorized Uniform Wind Algorithm* [Witt87a], which is used to estimate the windshift associated with the passage of a gustfront.

The discussions in the remainder of this report will concentrate on issues related to absolute de-aliasing.

1.6 ABSOLUTE VELOCITY DE-ALIASING

Section 1.2 described the estimation of a discrete mean Doppler velocity when the radar pulse train contains a single PRT. Now, suppose that the weather process is wide-sense stationary over an azimuth dwell-time – a reasonable assumption so long as the resolution volume contains a homogeneous windfield – and that we are able to independently interrogate the weather process with two different PRT's, $c_1\delta_T$ and $c_2\delta_T$, where c_1 and c_2 are relatively prime, positive, integers such that $c_1 < c_2$. The Nyquist velocities corresponding to these two sets of measurements are

$v_{u1} = \lambda(4c_1\delta_T)^{-1}$ and $v_{u2} = \lambda(4c_2\delta_T)^{-1}$, respectively. Generating separate mean velocity estimates (e.g. by using 1.4c twice) we obtain two, potentially aliased, estimates v_1 and v_2 .

v_1 and v_2 may be combined to generate a de-aliased estimate with the higher effective Nyquist velocity of v_u , the Nyquist velocity corresponding to a PRT of δ_T . This statement may seem counterintuitive, but it derives directly from number theory which tells us that the ordered pair $\{(v \bmod v_{u1}), (v \bmod v_{u2})\}$ is a unique function of v up to the Least Common Integral Multiple of v_{u1} and v_{u2} which is $c_1v_{u1} = c_2v_{u2} = v_u = \lambda(4\delta_T)^{-1}$. An example of this is provided in Figure 1.4 for the case $c_1 = 2$, $c_2 = 3$. The top pair of curves in the figure display the Doppler frequency aliasing for the two sampling frequencies $F_1 = (c_1\delta_T)^{-1}$ Hz and $F_2 = (c_2\delta_T)^{-1}$ Hz. The bottom curve displays the difference of the two aliased frequency estimates, f_1 and f_2 as a function of true Doppler frequency. Note that this difference is periodic with period δ_T^{-1} , the Nyquist interval corresponding to a PRT of δ_T .

Thus, if we can "simultaneously" interrogate the weather process with two PRT's $c_1\delta_T$ and $c_2\delta_T$, we can obtain an estimate with a Nyquist velocity of $\lambda(4\delta_T)^{-1}$ by comparing the estimates v_1 and v_2 , and determining the appropriate additive correction (e.g. via a table look-up). This final step in unfolding v_1 and v_2 is a statistical detection problem which is sensitive to errors in those two estimates. For the example of Figure 1.4, errors of magnitude greater than $\frac{1}{4}F_2$ in $f_1 - f_2$ would result in an erroneous unfolded estimate (assuming that the de-aliasing algorithm examines only the difference $f_1 - f_2$).

Pulse trains which incorporate two PRT's are of two basic types. The first is a *Batch PRT* sequence in which half the azimuth dwell time is spent taking samples at PRT $c_1\delta_T$ and the other half is spent taking samples at PRT $c_2\delta_T$. The second type of pulse train is a *Staggered PRT* sequence in which the PRT alternates from $c_1\delta_T$ to $c_2\delta_T$ on a pulse-by-pulse basis. Both types of sequences will be discussed in more detail. We note, though, that the Batch PRT scheme is prone to difficulties when shears exist within the resolution volume – a likelihood at longer ranges – for the following reason. The logic of velocity de-aliasing assumes that v_1 and v_2 are differently aliased estimates of the *same* mean velocity. If the windfield in the resolution volume is not uniform, the v_1 and v_2 generated with a Batch PRT scheme will be aliased estimates of the mean velocities for statistically *different* weather processes. In this case, the assumptions of velocity de-aliasing will be violated and the de-aliasing technique will generally fail. De-aliasing failures are not graceful since the errors are on the order of the Nyquist intervals corresponding to the two PRT's. The Staggered PRT scheme is a better choice in the respect that v_1 and v_2 will be spatially coherent. Some results on the performance of Staggered PRT velocity estimation are provided in [Sirmans76a].

VELOCITY DE-ALIASING WITH MULTIPLE SAMPLE RATES

TWO PRFs: $F_1 = \frac{1}{C_1 \delta_T}$, $F_2 = \frac{1}{C_2 \delta_T}$, δ_T IS "BASE INTERVAL"

WHEN C_1 AND C_2 ARE RELATIVELY PRIME INTEGERS, THE EFFECTIVE NYQUIST FREQUENCY IS $F_E = \frac{1}{2\delta_T}$

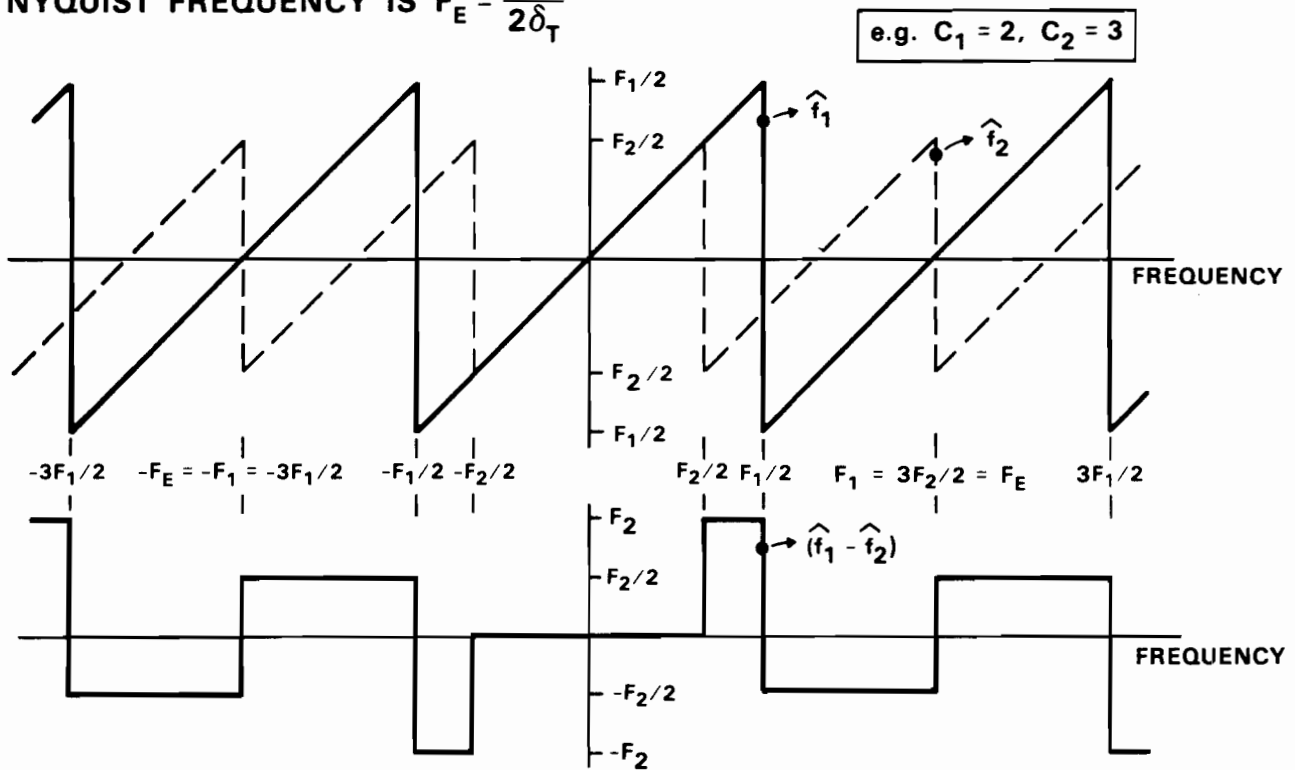


Figure 1.4: Velocity de-aliasing with multiple sample rates

1.7 THE CLUTTER CHALLENGE

The final topic to be discussed in this introduction is the need for effective clutter suppression in Doppler weather radars. For land based weather radars, clutter consists primarily of returns from ground targets such as trees, buildings and orographic features. Unfortunately, these targets possess radar cross-sections which are typically much larger than the aggregate radar cross-section of the particulates within a radar resolution volume.

Clutter of a given radar cross-section assumes different equivalent dBZ values as a function of range. Recent results [Mann86a] have shown that stressful clutter environments correspond to effective clutter returns of 55 dBZ at 10 km range to 45 dBZ at 100 km range, while average clutter returns are on the order of 45 dBZ at 10 km range to 35 dBZ at 100 km range. If we wish to maintain a 10 dB signal to clutter ratio for low-reflectivity phenomena such as gustfronts, clutter suppression in excess of 50 dB is required. With antenna rotation rates on the order of 4 rpm, this suppression must be achieved within azimuth dwell times on the order of 40 ms. We note that the azimuth dwell time is an important system parameter for clutter suppression. Its inverse is proportional to the attainable transition bandwidth of FIR clutter filters that operate on equispaced data, and to the frequency resolution available for frequency-domain clutter suppression techniques.

1.8 SUMMARY OF THE ISSUES AND OUTLINE OF THE REPORT

We have explained why Doppler weather radars usually operate in the S-band or C-Band frequency regimes (2-7 GHz), and that accurate Doppler estimates in the context of TDWR necessitate a minimum Nyquist velocity of 12 m/s – PRF's of 480 Hz and 960 Hz at $\lambda=10$ cm and $\lambda=5$ cm, respectively. We have shown that these PRF's are neither low enough to prevent range obscuration, nor high enough to prevent velocity aliasing. Schemes for de-aliasing velocity estimates were described; and we noted that it is possible to absolutely de-alias velocity estimates by use of two PRT's. Two types of radar pulse trains incorporating multiple PRT's were described, the Batch PRT and Staggered PRT waveforms. We have also shown that effective clutter suppression, in excess of 50 dB, is required if shear events with low reflectivities, such as gustfronts, are to be detected.

The organization of the remainder of this report is outlined below.

§2 Clutter Suppression for Batch PRT Sequences

The rationale for performing Batch PRT clutter suppression in the frequency domain is laid out and moment estimation with this scheme is described.

§2.1 Data Taper Selection for Frequency Domain Clutter Suppression

A normalized expression for assessing data taper performance in the context of clutter suppression is derived. This expression is employed to

evaluate seven candidate windows for Batch and equispaced PRT clutter suppression in a TDWR context.

§3 Clutter Suppression for Staggered PRT Sequences

§3.1 Staggered PRT Filter Structure

The staggered PRT sampling scheme is described and the architecture of the *Staggered PRT Filter* is introduced.

§3.2 Staggered PRT Filter Response

Z-transforms for multirate data sequences are presented and used to justify a time-varying filter architecture. The effects of having identical partial response sequences, which is equivalent to a conventional FIR tapped delay line, are discussed for odd and even filter lengths.

§3.2.1 Average Power Transfer Function

The staggered PRT filter's power transfer function for lags which are multiples of c_1+c_2 , $|G(\omega)|^2$, is derived. This is one of the three staggered PRT filter transfer functions that interact with the pulse-pair moment estimators. Multiple transfer functions are an important feature of the time-varying filter architecture.

§3.2.2 Convolutions of Staggered PRT Sequences

The convolution of staggered PRT sequences is contrasted with the convolution of equispaced sequences as preparation for section 3.2.3.

§3.2.3 Lag c_1 and Lag c_2 Power Transfer Functions

The staggered PRT filter's power transfer functions for lags of c_1 or c_2 plus multiples of c_1+c_2 are derived.

§3.3 Properties of the $C_i(z)$ and Effective Power Transfer Functions

§3.3.1 Z-Plane Zero Distribution of $|G(\omega)|^2$

Conjugate and reciprocal symmetry of the z-plane zero distribution of $|G(\omega)|^2$ is established. These symmetries guarantee a $|G(\omega)|^2$ which is a real, even, function of frequency.

§3.3.2 Phase Responses of $C_0^*(e^{j\omega\delta_T})C_1(e^{j\omega\delta_T})$ and $C_0(e^{j\omega\delta_T})C_1^*(e^{j\omega\delta_T})$

The phase response of the lags c_1 and c_2 power transfer functions are discussed. The non-zero phase response of the staggered PRT filter is a key factor in its interaction with the moment estimation process. Examples are provided of velocity estimation with a staggered PRT filter.

§3.3.3 Uncontrollable Zeroes in the $C_i(z)$

Not all of the z-plane zero locations of the staggered PRT filter may be directly specified by the filter designer. The number and z-plane distribution of these uncontrollable zeroes are discussed as functions of the filter length and stagger ratio.

§4 Staggered PRT Filter Design Techniques

§4.1 Design Technique: Coefficient Selection

A design technique based on selecting coefficients from a time-aligned equispaced filter with a PRT of δ_T is described and assessed. The DFT is shown to be an isometric mapping between the time and frequency domains.

§4.2 Design Technique: Maximally Flat Response

The assignment of all controllable zeroes to $z=1$ is assessed as a design technique.

§4.3 Design Technique: Output Signal to Clutter Ratio Maximization

Staggered PRT filter coefficients are selected to provide optimal suppression of scan-modulated clutter with a generalized weather spectrum.

§5 Conclusions

§5.1 Batch PRT

§5.2 Staggered PRT

§5.3 Further Research

Suggestions are provided for characterizing the z -plane zero locations of the staggered PRT filter; and techniques for phase control of the lags c_1 and c_2 transfer functions are described. A composite filter architecture, combining equispaced and staggered PRT filters, is described.

2.0 CLUTTER SUPPRESSION FOR BATCH PRT SEQUENCES

The Batch PRT pulse sequence is a pulse train with two alternating blocks of equispaced pulses as depicted in Figure 2.1. A block of N_1 samples is collected with PRT $c_1\delta_T$, followed by a block of N_2 samples with PRT $c_2\delta_T$. N_1 and N_2 are typically selected so that each block of equispaced samples has a duration of approximately half the azimuth dwell time. Clutter rejection is performed independently for each block of equispaced samples.

The Doppler spectrum of the weather process may be concentrated near zero velocity. As it is undesirable for a clutter filter to reject the weather signal, the clutter filter's stopband and transition regions should be limited to the narrowest velocity interval, centered about zero, which affords the necessary rejection. At S-Band, typical spectrum widths for scan-modulated, distributed clutter are ≈ 0.25 m/s with the assumption of a Gaussian shaped clutter spectrum [Evans83a]. For this model, 50 dB clutter rejection requires that the filter's stopband extend to at least four standard deviations, a 1 m/s stopband edge. The transition region bandwidth should be less than 2 m/s, so that passband performance is assured for velocities greater than 3 m/s.

For FIR clutter filters operating upon equispaced data (*e.g.* passband power ripple of 3 dB, stopband power ripple below -50 dB, and more than 10 taps), the width of the transition region, in Hz, is approximately 1.35 times the inverse of the filter's impulse response duration in seconds [Herrmann73a]. Typical antenna rotation rates for weather radars correspond to dwell times on the order of 50 ms. The dwell time per equispaced block of samples is then 25 ms; and, if we restrict the filter's impulse response duration to, say, 15 ms to insure a sufficient number of samples at the filter's output for reliable estimates of the autocorrelation at lags zero and one, the resulting transition region bandwidth is 90 Hz, or 4.5 m/s at S-Band. This example provides an optimistic estimate of the transition region bandwidth – the 10 ms integration time may not provide pulse-pair Doppler moment estimates of sufficiently small variance [Zrnić79a].

Rather than performing clutter suppression in the time domain, weather radars employing Batch PRT sequences could perform clutter rejection in the frequency domain [Passarelli81a]. Each block of equispaced samples is processed in the following manner. The data sequence, possibly weighted by a data taper, is transformed into the frequency domain via the Discrete Fourier Transform (DFT). The DFT of the transformed sequence is then replaced at each point by its magnitude squared, generating a periodogram estimate of the weather plus clutter spectrum. The central (zero-frequency) coefficient of the periodogram is set to zero, possibly along with its neighbors; and then transformed back via the Inverse DFT to generate an estimate of the weather autocorrelation function. Pulse-pair estimation is then performed with the autocorrelation estimates.

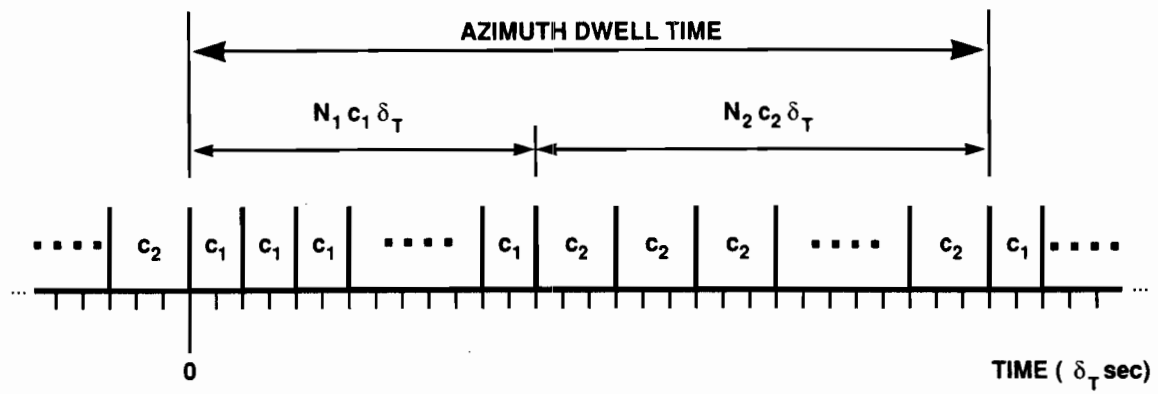


Figure 2.1: Batch PRT sampling scheme

2.1 DATA TAPER SELECTION FOR FREQUENCY DOMAIN CLUTTER SUPPRESSION

The particular data taper which is applied to time domain sequence prior to performing the DFT has a significant effect on the efficacy of frequency-domain clutter suppression. For periodogram-based spectral estimation, data tapers are employed to limit the blurring or apodization of the spectral estimate resulting from a finite record length [Harris78a]. In an analogous fashion, data tapers may be employed for frequency-domain clutter suppression to confine the clutter's spectral energy to Doppler frequencies near zero.

The intent of this current section is to present an analytical expression, independent of radar constants, which is useful in assessing the effectiveness of various data tapers for frequency-domain clutter suppression. Assume a finite energy, wide-sense stationary, clutter process $s(t)$ whose true power spectrum is given by

$$S_s(f) \triangleq \frac{K_0}{\sigma_c \sqrt{2\pi}} e^{-f^2/2\sigma_c^2}$$

where σ_c is the clutter spectrum width in Hz. We will denote the autocorrelation function of $s(t)$ by $R_s(\tau)$. Suppose that we make an observation of $s(t)$ of duration T and weight that observation by a data taper

$$w(t) \triangleq \begin{cases} d(t) & , \quad |t| \leq \frac{T}{2} \\ 0 & , \quad |t| > \frac{T}{2} \end{cases}$$

where $d(t)$ is a real, even, time function with finite energy.

Now, the continuous analogue of the windowed periodogram estimate is the following expectation with respect to $s(t)$.

$$\mathbf{E}_s \left\{ \frac{1}{T} \left| \int_{\frac{-T}{2}}^{\frac{T}{2}} w(t)s(t)e^{-j2\pi ft} dt \right|^2 \right\} \quad (2.1)$$

Since $w(t)$ and $s(t)$ both possess finite energy, the integrals may be combined to yield

$$= \frac{1}{T} \mathbf{E}_s \left\{ \int_{\frac{-T}{2}}^{\frac{T}{2}} \int_{\frac{-T}{2}}^{\frac{T}{2}-\tau} w(\xi+\tau)w^*(\tau)s(\xi+\tau)s^*(\tau)e^{-j2\pi f\xi} d\xi d\tau \right\}$$

where we have made the substitution $\xi = t - \tau$. Noting that $w^*(\tau) = w(-\tau)$, we may take the expectation inside the integral and change the order of integration with τ replaced by $-\tau$ to obtain

$$= \frac{1}{T} \int_{-T}^T R_s(\xi) \int_{\frac{-T}{2}}^{\frac{T}{2}} w(\xi-\tau)w(\tau) e^{-j2\pi f \xi} d\tau d\xi = \frac{1}{T} \left\{ S_s(f) * W^2(f) \right\}$$

where $W(f)$ is the Fourier Transform of the data taper $w(t)$.

Now suppose that we set this "periodogram" to zero for frequencies in the interval $[-\Omega, \Omega]$. As $W(f)$ and $S_s(f)$ are both even, the power remaining in the spectrum is given by

$$\begin{aligned} E_p &\triangleq 2 \int_{\Omega}^{\infty} \int_{-\infty}^{\infty} W^2(\xi) S_s(f-\xi) d\xi df \\ &= 2\sigma_c \int_{-\infty}^{\infty} W^2(\xi) \int_{\frac{\Omega-\xi}{\sigma_c}}^{\infty} S_s(\gamma\sigma_c) d\gamma d\xi \end{aligned} \quad (2.2)$$

where we have made the replacement $\gamma = \frac{f-\xi}{\sigma_c}$. Substituting for S_s , we have

$$= 2K_0 \int_{-\infty}^{\infty} W^2(\xi) \int_{\frac{\Omega-\xi}{\sigma_c}}^{\infty} \frac{1}{\sqrt{2\pi}} e^{-\frac{\gamma^2}{2}} d\gamma d\xi$$

yielding our result

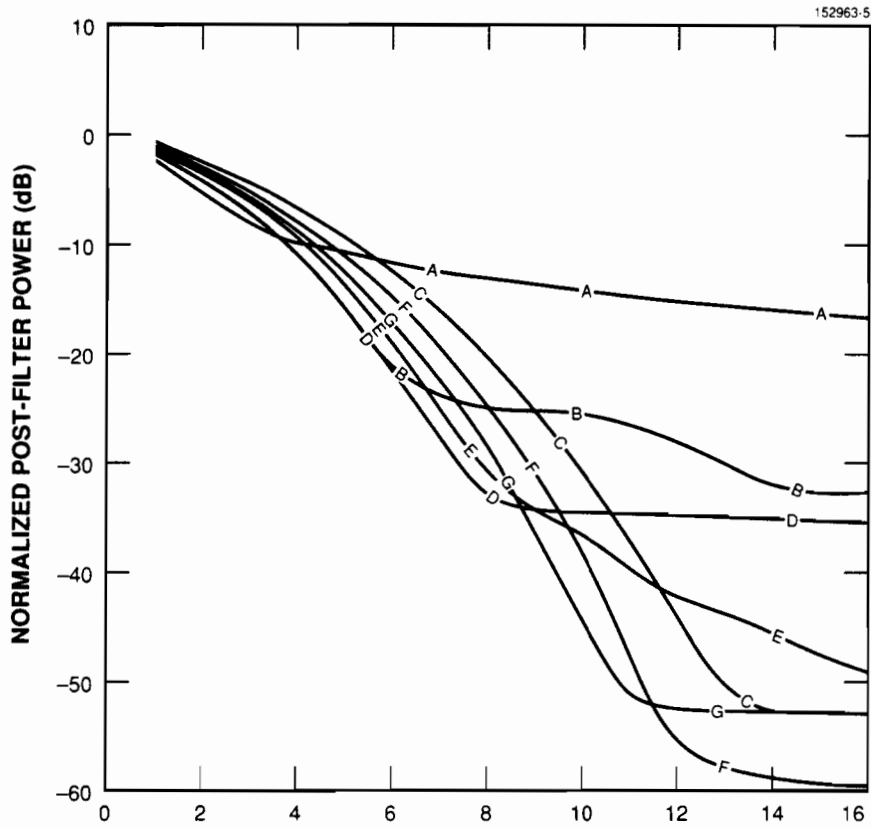
$$E_p = 2K_0 \int_{-\infty}^{\infty} W^2(\xi) \operatorname{erfc} \left(\frac{\Omega-\xi}{\sigma_c} \right) d\xi \quad (2.3)$$

where $\operatorname{erfc}(x)$ is the complimentary error function,

$$\operatorname{erfc}(x) \triangleq 1 - \frac{1}{\sqrt{2\pi}} \int_{-\infty}^x e^{-\frac{\zeta^2}{2}} d\zeta$$

Equation 2.3 is a useful result in that it completely characterizes the efficacy of a data taper for frequency-domain clutter rejection, parameterized by the ratio of the clutter spectrum width σ_c and the stopband cut-off frequency Ω . We can apply this result to assess frequency-domain clutter rejection for blocks of equispaced pulses by plotting E_p as a function of Ω/σ_c for a sampled data taper w_k of length N and azimuth dwell time $N\delta_T$.

Figure 2.2 displays normalized graphs of equation 2.3 for seven different data tapers, with representative S-Band Doppler parameters. This example is for the case of a uniform sampling frequency of 640 Hz over the azimuth dwell time and a 33 point data taper. The azimuth dwell time is 52 ms. The value selected for σ_c is 5 Hz, which corresponds to a 0.25 m/s clutter spectrum width for a 3 GHz radar.



PASSBAND EDGE / CLUTTER WIDTH

SMPL. FREQ. = 640.00 Hz
 CLUTTER WIDTH = 5.0000 Hz
 33 POINT WINDOW

A = DIRICHLET WINDOW	C = PARZEN WINDOW
B = BARTLETT WINDOW	D = HAMMING WINDOW
	E = HANN WINDOW
	F = BLACKMAN WINDOW
	G = DOLPH-CHEBYSHEV WINDOW

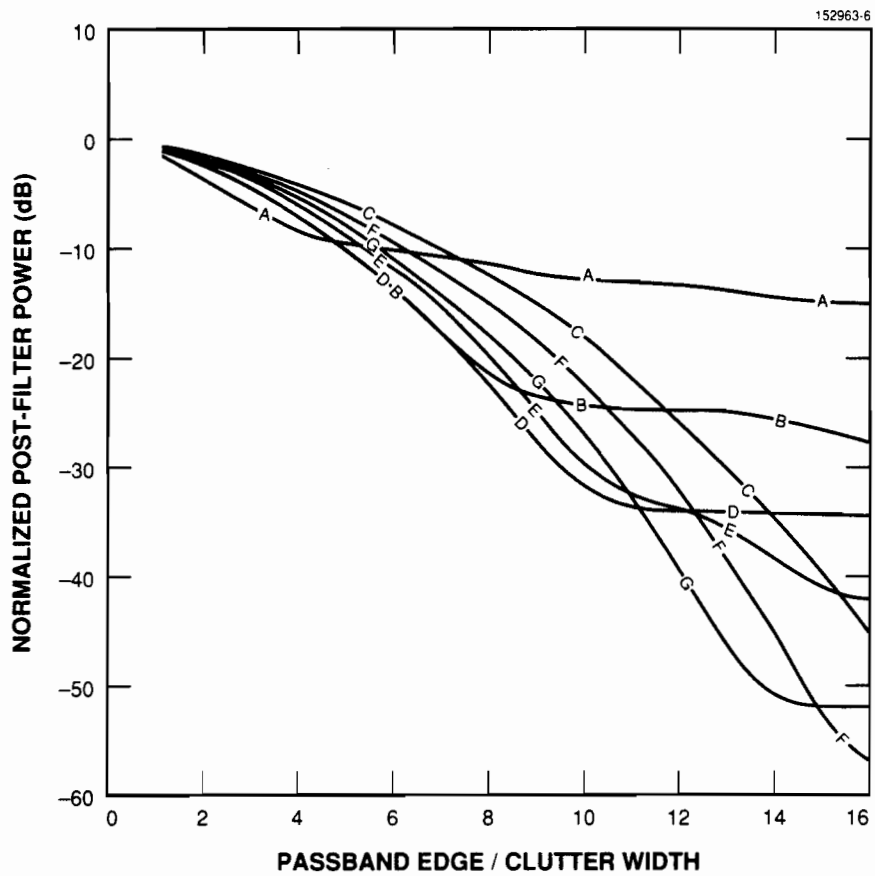
Figure 2.2: Clutter rejection via the windowed periodogram, 33 point window

Window "A" is the Dirichlet or "boxcar" window which applies uniform weights to the data sequence – the Dirichlet window corresponds to the case in which no data taper is employed. Window "B" is the Bartlett or triangular window, it is the time-scaled convolution of the Dirichlet window with itself. Window "C" is the the Parzen window, it is the time-scaled convolution of the Barlett window with itself and consists of segments of second and third order polynomials. Window "D", the Hamming window, consists of a cosine bell upon a pedestal; it is a weighted average of Window "E" the von Hann window, which is a simple cosine bell, and the Dirichlet window. The Blackman window, "F", is a second order trigonometric polynomial. The Dolph-Chebyshev window, "G", has uniform sidelobe levels, and possesses the narrowest main lobe width for a given sidelobe level (The examples in this report employ a squared transform sidelobe level of -70 dB, this value was selected to provide 50 dB of clutter rejection in the example of Figure 2.2.) [Harris78a, Jasik61a] .

These seven windows provide a representative sample of data tapers; ranging from the Dirichlet window which possesses a very narrow main lobe in the frequency domain and large sidelobes, to the Blackman window which possesses sidelobes which are orders of magnitude less than those of the Dirichlet window (at the expense of increased main lobe width), to the Chebyshev window which "optimally" balances main lobe width against sidelobe level. The dynamic ranges of the windows' coefficients are 0, 12, 33, 11, 20, 25 and 18 dB for windows A through G in Figure 2.2, respectively. Windows A, B and C are "constructed" windows; while windows D, E and F are trigonometric windows. Window G's DFT is a sampled Chebyshev polynomial.

In examining Figure 2.2, the frequency bin size of the DFT must be considered (*i.e.* the frequency locations at which coefficients may be set to zero). In this case the bin size is $(640/33)=19.4 \text{ Hz} \approx 1 \text{ m/s}$ at S-Band. It is apparent that some sort of data taper is required for frequency-domain clutter rejection, as curve A – the taperless case – fails to reach even 20 dB suppression with a passband edge of 3 m/s ($\Omega/\sigma_c = 12$) . The knees in the various curves correspond to transitions from mainlobe to sidelobe rejection for the windows. This transition happens at the first non-zero DFT bin edge for window A ($\Omega/\sigma_c = 4 \approx 20 \text{ Hz}$ or 1 m/s); at the second non-zero DFT bin edge for windows B, D and E; and at the third non-zero DFT bin edge for windows C, F and G. This figure demonstrates that acceptable (*i.e.* $\geq 50 \text{ dB}$) clutter rejection is achievable with this technique, for a 3 m/s passband edge at S-Band. We may also infer from the figure that the maximum achievable clutter suppression is driven by a data taper's sidelobe levels rather than its main lobe width.

The parameters for Figure 2.3 are identical to those of Figure 2.2 except that the azimuth dwell time has been reduced to 40 ms. Reducing the dwell time from 50 to 40 ms has the approximate effect of scaling the curves in Figure 2.3 horizontally by a factor of 50/40 relative to Figure 2.2. Since each DFT point nominally



SMPL. FREQ. = 640.00 Hz C = PARZEN WINDOW
 CLUTTER WIDTH = 5.0000 Hz D = HAMMING WINDOW
 25 POINT WINDOW E = HANN WINDOW
 A = DIRICHLET WINDOW F = BLACKMAN WINDOW
 B = BARTLETT WINDOW G = DOLPH-CHEBYSHEV WINDOW

Figure 2.3: Clutter rejection via the windowed periodogram, 25 point window

corresponds to a frequency band of one bin width, centered at that point, it appears that 50 dB of rejection with a 40 ms dwell time could be realized by zeroing the same number of DFT coefficients as for a 50 ms dwell time.

Figure 2.4 is an S-Band example of frequency-domain clutter suppression with a Block PRT scheme. All parameters are identical to those of Figure 2.2, except that the window length has been halved, corresponding to a block of equispaced samples which occupy half an azimuth dwell time as in Figure 2.1. The DFT bin size increases accordingly to $(640/17)=37.6 \text{ Hz} \approx 2 \text{ m/s}$. The available passband edges are then at 2,4,6, ... m/s. By halving the observation time, the spread of the clutter spectral energy due to a finite record length is increased, roughly by a factor of two, and clutter rejection for a given passband edge is correspondingly reduced. Figure 2.2 displays average rejection of 24 dB for a passband edge of 2 m/s ($\Omega/\sigma_c = 8$), while the corresponding rejection depicted in Figure 2.4 is closer to 10 dB.

Figure 2.5 displays the available clutter rejection for the case of Figure 2.4, but for passband edges up to 8 m/s ($\Omega/\sigma_c = 32$). Figure 2.5 closely resembles Figure 2.2 with the abscissa scaled by a factor of two. The requisite 50 dB of rejection is attained with the Blackman and Dolph-Chebyshev data tapers, but not until the passband edge is moved to the third DFT bin at 6 m/s. Relaxing the passband edge requirement from 3 m/s to 6 m/s will not necessarily make this an acceptable clutter rejection scheme for use with velocity de-aliasing. With a 6 m/s passband edge, the filter stopband occupies three-eighths of the entire Nyquist interval for this case. Not only will weather returns with Doppler velocities in the range $[-6 \text{ m/s}, 6 \text{ m/s}]$ be suppressed; velocities in the Doppler intervals which alias to that range, $[-6+2nv_u, 6+2nv_u]$ where $n \in \mathbf{I}$, will also be suppressed.

If frequency-domain clutter suppression is to be employed with Batch PRT schemes for velocity de-aliasing purposes, one of the following two compromises must be made. Either

- 1) the radar's azimuth dwell time must be increased beyond 50 ms – equivalently, the azimuth scanning rate must be reduced below 20 degrees per second (increasing the likelihood of velocity de-aliasing errors due to temporal/azimuthal non-stationarity of the weather process); or
- 2) the 50 dB clutter rejection requirement must be relaxed, at the cost of increased potential for obscuration of low reflectivity, low-altitude, phenomena.

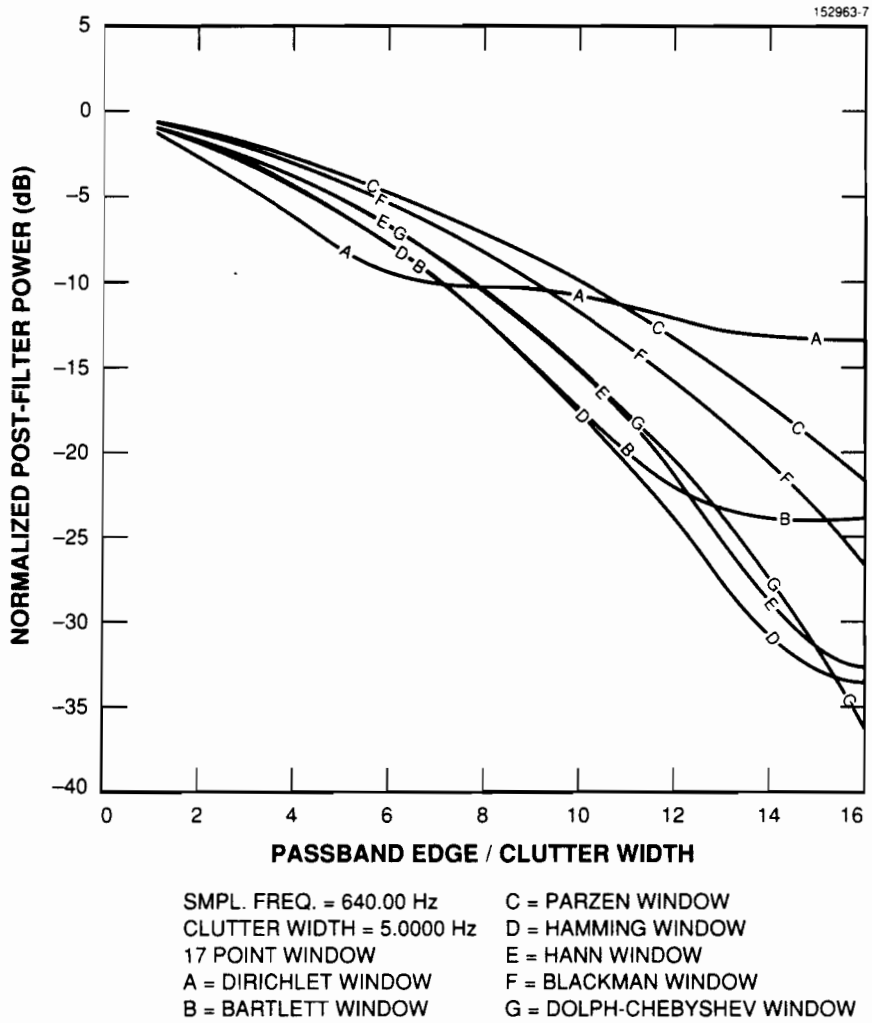


Figure 2.4: Clutter rejection via the windowed periodogram, 17 point window

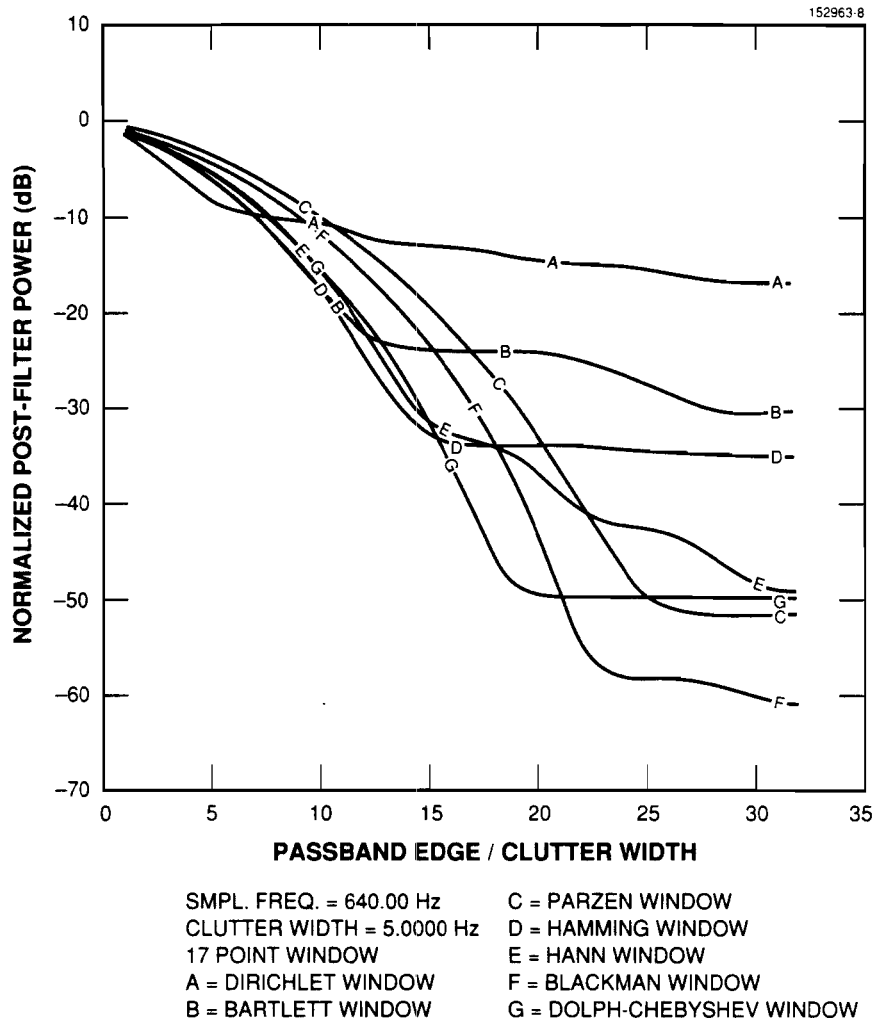


Figure 2.5: Clutter rejection via the windowed periodogram, 17 point window

3.0 CLUTTER SUPPRESSION FOR STAGGERED PRT SEQUENCES

Clutter suppression for staggered PRT sequences may be achieved by use of FIR (Finite Impulse Response or "all-zero") filters which operate on the unevenly spaced data. The goals of this section of the report are to develop a general theory of these filters; to identify those areas in which their behavior differs from FIR filters that operate on equispaced data; and to discuss the interaction of these filters with weather parameter estimation.

3.1 STAGGERED PRT FILTER STRUCTURE

We begin by noting that the filtering of unevenly spaced data has received little attention in the engineering literature. H.W. Thomas and N.P. Lutte treat this topic analytically in two papers which appeared in the early 1970's [Thomas72a, Thomas74a]. The method of analysis employed in those papers is that of the advanced Z-Transform. The approach taken here will be somewhat different.

The staggered PRT sampling scheme observes data values at times

$$\dots, -(c_1+2c_2)\delta_T, -(c_1+c_2)\delta_T, -c_2\delta_T, 0, c_1\delta_T, (c_1+c_2)\delta_T, (2c_1+c_2)\delta_T, \dots$$

where $c_1 < c_2$. The sampling method is depicted in Figure 3.1 for the case $c_1=2, c_2=3$ (δ_T has units of seconds throughout the following discussion). As stated earlier, with c_1 and c_2 constrained to be relatively prime integers, frequencies in the range $(-(2\delta_T)^{-1}, (2\delta_T)^{-1}]$ Hertz may be unambiguously observed.

The output of a causal FIR filter with N coefficients is a weighted sum of the current input value and the $N-1$ most recent input values. In the case of an equispaced sampling scheme with an intersample spacing of T seconds, the M th most recent sample is collected MT seconds previous to the current sample ($M = 0, 1, \dots$ and $M = 0$ corresponds to the current sample). In the case of a staggered sampling scheme, however, the time difference between the sampling instants for the current sample and the M th previous sample is a function of the current sampling instant. Defining

$$d_{0,0}=0, d_{0,1}=c_2, d_{0,2}=c_1+c_2, d_{0,3}=c_1+2c_2, d_{0,4}=2c_1+2c_2, d_{0,5}=2c_1+3c_2, \dots$$

$$d_{1,0}=0, d_{1,1}=c_1, d_{1,2}=c_1+c_2, d_{1,3}=2c_1+c_2, d_{1,4}=2c_1+2c_2, d_{1,5}=3c_1+2c_2, \dots$$

it may be observed that for a sample taken $c_2\delta_T$ seconds after the immediately preceding sample, the difference in sampling instants between this sample and the M th preceding sample is $d_{0,M}\delta_T$ seconds. Similarly, for a sample taken $c_1\delta_T$ seconds after the immediately preceding sample, the difference in sampling instants between this sample and the M th preceding sample is $d_{1,M}\delta_T$ seconds. This is illustrated for the case $c_1=2, c_2=3$ in Figure 3.2.

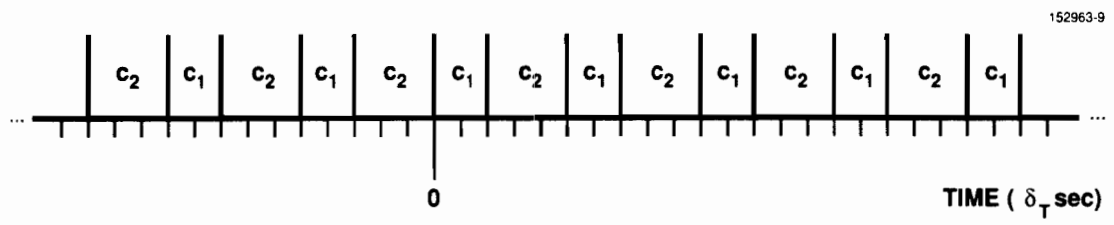


Figure 3.1: Staggered PRT sampling scheme

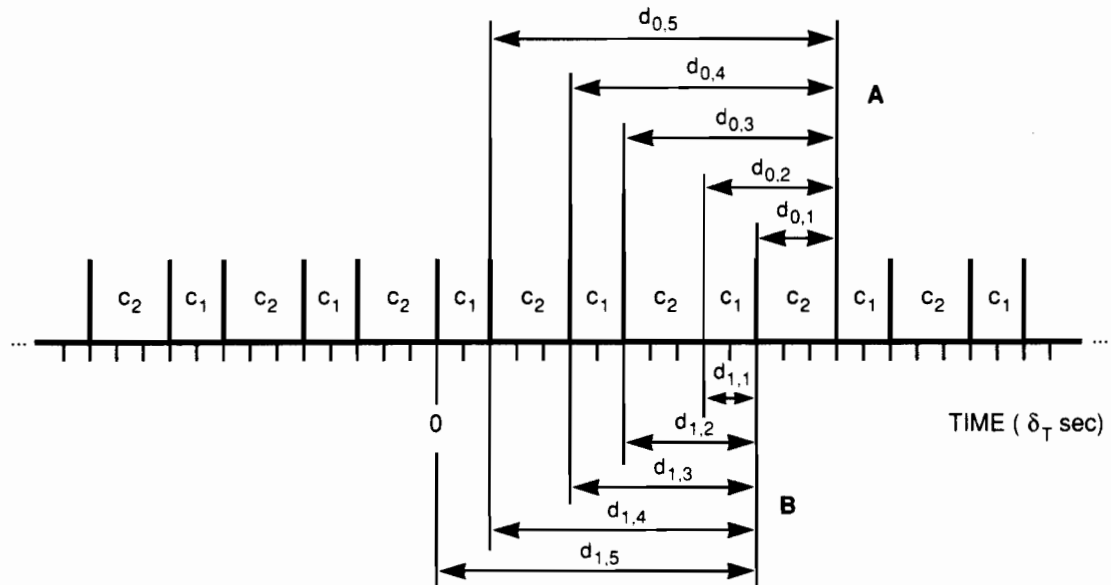


Figure 3.2: Staggered PRT intersample delays

The sample-to-sample alternation of the intersample spacings between a given sample and its predecessors suggests that the use of two sets of filter weights would provide the greatest degree of control in filtering time series data collected in this manner. One set of weights, $h_0 \triangleq \{h_{0,i}\}_{i=0}^{N-1}$, would be selected to achieve a desired response – the meaning of *response* will be defined subsequently – for samples observed at times $\{d_{0,i} \delta_T\}_{i=0}^{N-1}$ prior to the current sample. This set of weights would be utilized when the current sample is that at time **A** in Figure 3.2, and at all other times when the current sample is taken at $p(c_1+c_2)\delta_T$ seconds relative to time **A**, $p \in \mathbf{I}$. The second set of weights, $h_1 \triangleq \{h_{1,i}\}_{i=0}^{N-1}$, would be selected to achieve a desired response for samples observed at times $\{d_{1,i} \delta_T\}_{i=0}^{N-1}$ prior to the current sample. This set of weights would be employed when the current sample is that at time **B** in Figure 3.2, and at all other times when the current sample is taken at $p(c_1+c_2)\delta_T$ seconds relative to time **B**, $p \in \mathbf{I}$. If $x(t)$ is the continuous time function being sampled, the filter is depicted schematically in Figure 3.3, where we have defined $x_k \triangleq x(\Delta_k \delta_T)$ and

$$\Delta_k \triangleq \left\{ \begin{array}{ll} \cdot & \cdot \\ \cdot & \cdot \\ \cdot & \cdot \\ -(c_1+c_2) & k=-2 \\ -c_2 & k=-1 \\ 0 & k=0 \\ c_1 & k=1 \\ c_1+c_2 & k=2 \\ 2c_1+c_2 & k=3 \\ \cdot & \cdot \\ \cdot & \cdot \\ \cdot & \cdot \end{array} \right.$$

We will refer to the two sets of filter weights h_0 and h_1 , employed as in Figure 3.3 as a *Staggered PRT Filter of Length N*; and to each set of weights h_i , $i = 0,1$, as the i th *partial response sequence*.

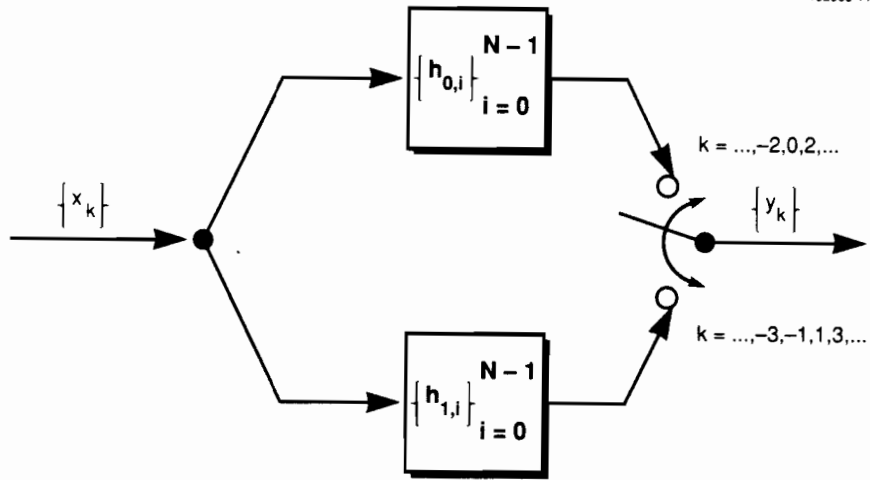


Figure 3.3: Staggered PRT filter architecture

3.2 STAGGERED PRT FILTER RESPONSE

The need for two different partial response sequences, corresponding to the two delay sequences $\{d_{i,k}\}_{k=0}^{N-1}$, $i = 0,1$, may be demonstrated by a simple example. As a preface, we introduce the Z-Transforms of the h_i . The one-sided Z-Transform of a continuous time function $x(t)$ relative to some sampling period T is defined as

$$X(z) \triangleq \mathbf{Z}\{x(t)\} = \sum_{n=0}^{\infty} x(nT)z^{-n}$$

If $x(nT)$ has finite energy, this series converges everywhere outside of some circle, centered at the origin in the z -plane. Due to the relative primality of c_1 and c_2 , the greatest common remainderless divisor of the two sampling periods $c_1\delta_T$ and $c_2\delta_T$ is δ_T . Thus, the Z-Transforms of the partial response sequences are given by

$$C_i(z) \triangleq \mathbf{Z}\{h_i\} = \sum_{k=0}^{N-1} h_{i,k} z^{-d_{i,k}}, \quad i = 0,1$$

In the following discussions, the region of convergence of the $C_i(z)$ is assumed to include $|z| = 1$.

By evaluating the $C_i(z)$ on the unit circle, relative to the base sampling rate of δ_T , we obtain

$$C_i(z) \Big|_{z=e^{j\omega\delta_T}} = \sum_{k=0}^{N-1} h_{i,k} e^{-jd_{i,k}\omega\delta_T}, \quad i = 0,1 \quad (3.1)$$

This is the complex frequency response of the partial response sequence h_i to a sinusoid at radian frequency ω , sampled at intervals of δ_T . We note that the period of $C_i(z)$, as a function of ω , is the length of the interval $(-\pi\delta_T^{-1}, \pi\delta_T^{-1}]$ – the same frequency interval which may be unambiguously observed for any relatively prime integer values of c_1 and c_2 .

When $h_0=h_1$ (which corresponds to passing the staggered PRT sequence through a conventional tapped delay line), the relationships between C_0 and C_1 for even values of N differ from those for odd values of N . Consider the following case: $N=2$, $c_1=1$, $c_2=2$ and $h_0=h_1=\{1,1\}$. This choice of parameters yields

$$C_0(e^{j\omega\delta_T}) = 1+(e^{j\omega\delta_T})^{-2}, \quad \text{zeroes at } \omega\delta_T = \pm\frac{\pi}{2}$$

$$C_1(e^{j\omega\delta_T}) = 1+(e^{j\omega\delta_T})^{-1}, \quad \text{zeroes at } \omega\delta_T = \pm\pi$$

Thus, h_0 effectively acts as a notch filter, with notches at $\pm(4\delta_T)^{-1}$ Hz, while h_1 functions as a lowpass filter with notches at $\pm(2\delta_T)^{-1}$ Hz. With an input sequence of, say $\{x_k\} = \{\sin(\omega\Delta_k \delta_T)\}$, $\omega = \pi\delta_T^{-1}$, it is apparent that a modulation effect, due to the mismatch of C_0 and C_1 , will be introduced into the output sequence $\{y_k\}$ of Figure 3.3.

Alternatively, for odd N , consider the case: $N=3, c_1=1, c_2=2$ and $h_0=h_1=\{1,1,1\}$. We have

$$C_0(e^{j\omega\delta_T}) = 1 + (e^{j\omega\delta_T})^{-2} + (e^{j\omega\delta_T})^{-3}$$

$$C_1(e^{j\omega\delta_T}) = 1 + (e^{j\omega\delta_T})^{-1} + (e^{j\omega\delta_T})^{-3} = (e^{j\omega\delta_T})^{-3} C_0^*(e^{j\omega\delta_T})$$

In fact, for odd N and a real $h_0=h_1$, it is always the case that $C_1(z) = z^{-\frac{1}{2}(N-1)(c_1+c_2)} C_0^*(z)$.

These two examples, the example for $N=2$ in particular, point out the advantage of individual specifications for h_0 and h_1 . They also show that the effect of alternation between h_0 and h_1 is a consideration in selecting those coefficients. As the autocorrelation properties of the output sequence $\{y_k\}$ are of primary interest, we will subsequently be concerned with the effective power transfer functions of the staggered PRT filter.

3.2.1 Average Power Transfer Function

The average power transfer function of a staggered PRT filter at frequency $\omega \in (-\pi\delta_T^{-1}, \pi\delta_T^{-1}]$, $|G(\omega)|^2$, will be defined as the filter's sample-averaged, magnitude-squared, output given an input of a sampled phasor at radian frequency ω . Thus we have as input $\{x_k\} = \{e^{j\omega\Delta_k\delta_T}\}$, and

$$|G(\omega)|^2 \triangleq \lim_{M \rightarrow \infty} \left[\frac{1}{2M+1} \sum_{k=-M}^M |y_k|^2 \right] \quad (3.2)$$

For k even, we note that $\Delta_{k-l} = \Delta_k - d_{0,l}$ and hence that

$$y_k = \sum_{l=0}^{N-1} h_{0,l} e^{j\Delta_{k-l}\omega\delta_T}$$

$$= e^{j\Delta_k\omega\delta_T} \sum_{l=0}^{N-1} h_{0,l} e^{-jd_{0,l}\omega\delta_T}$$

$$= e^{j\Delta_k\omega\delta_T} C_0(e^{j\omega\delta_T})$$

Similarly, for k odd, $y_k = e^{j\Delta_k\omega\delta_T} C_1(e^{j\omega\delta_T})$ so that equation 3.2 may be rewritten as

$$|G(\omega)|^2 = \lim_{M \rightarrow \infty} \left[\sum_{\substack{k=-M \\ k \text{ odd}}}^M \frac{1}{2M+1} |C_1(e^{j\omega\delta_T})|^2 + \sum_{\substack{k=-M \\ k \text{ even}}}^M \frac{1}{2M+1} |C_0(e^{j\omega\delta_T})|^2 \right] \quad (3.3)$$

or

$$|G(\omega)|^2 = \lim_{M \rightarrow \infty} \left[\begin{array}{l} \frac{1}{2M+1} \left\{ (M+1) |C_0(e^{j\omega\delta_T})|^2 + M |C_1(e^{j\omega\delta_T})|^2 \right\}, M \text{ even} \\ \frac{1}{2M+1} \left\{ M |C_0(e^{j\omega\delta_T})|^2 + (M+1) |C_1(e^{j\omega\delta_T})|^2 \right\}, M \text{ odd} \end{array} \right]$$

Recalling that $C_0(e^{j\omega\delta_T})$ and $C_1(e^{j\omega\delta_T})$ are finite for all values of ω and taking the limit, we arrive at the expected result

$$|G(\omega)|^2 = \frac{1}{2} |C_0(e^{j\omega\delta_T})|^2 + \frac{1}{2} |C_1(e^{j\omega\delta_T})|^2 \quad (3.4a)$$

If the $\{h_{i,k}\}_{k=1}^{N-1}$, $i = 0,1$, are real, we obtain

$$|G(\omega)|^2 = \left[\frac{1}{2} C_0(z) C_0\left(\frac{1}{z}\right) + \frac{1}{2} C_1(z) C_1\left(\frac{1}{z}\right) \right]_{z=e^{j\omega\delta_T}}, \quad \omega \in \left[\frac{-\pi}{\delta_T}, \frac{\pi}{\delta_T} \right] \quad (3.4b)$$

$|G(\omega)|^2$ represents the average power gain of the staggered PRT filter for a phasor input at discrete frequency $\omega \in (-\pi\delta_T^{-1}, \pi\delta_T^{-1}]$. Superposition may be employed to determine the filter's average power gain for more complicated input functions.

3.2.2 Convolutions of Staggered PRT Sequences

The purpose of this section of the report is to examine the convolution operator in the context of Staggered PRT sequences. Following sections will employ the convolution operator in deriving their results.

Consider two equispaced data sequences, $\{g_{i,k}\}_{k=0}^{N-1}$, $i = 0,1$, where the $g_{i,k}$ are identically zero for all $k \notin \{0, \dots, N-1\}$. Denoting the convolution operator by an inline $*$, we have by definition

$$f_l \triangleq g_0 * g_1 \Big|_l = \sum_{k=0}^{N-1} g_{0,k} g_{1,l-k}$$

f_l is then identically zero outside of $\{0, \dots, 2(N-1)\}$ and, subject to a particular choice of the $g_{i,k}$, may be non-zero for any value of l within that set.

When two Staggered PRT sequences are convolved, the time extent of the convolution is constrained by the time extent of the two sequences, as above. However, the special structure of these sequences imposes additional constraints on the instants at which the convolution may be non-zero. We will demonstrate this effect for a convolution required in the following section, $h_{1,k} * h_{0,-k}$. $h_{0,-k}$ is the partial response sequence $h_{0,k}$ reflected about $t=0$. Recalling that δ_T is the greatest common remainderless divisor of the two intersample delays, $c_1\delta_T$ and $c_2\delta_T$, define the following two equispaced sequences with intersample delays of δ_T .

$$\{\alpha_{i,m}\}_{m=-\infty}^{\infty} \triangleq \begin{cases} h_{0,k} & , m = -d_{0,k} & , i=0 \\ h_{1,k} & , m = d_{1,k} & , i=1 \\ 0 & , \text{otherwise} \end{cases}$$

Whence,

$$f_l = h_{1,k} * h_{0,-k} \Big|_l = \sum_{m=-\infty}^{\infty} \alpha_{1,l-m} \alpha_{0,-m} \quad , l \in \mathbf{I}$$

where l indexes sampling times in units of δ_T . This f_l will be identically zero for values of $l \notin [-d_{0,N-1}, \dots, d_{1,N-1}]$.

In particular, this f_l may take on non-zero values only at sampling times $l\delta_T$ for which $l \in [-d_{0,N-1}, \dots, d_{1,N-1}]$ and one of the following four equations is satisfied.

$$\begin{aligned} 1) \quad & l-p(c_1+c_2) = 0 \\ 2) \quad & l-p(c_1+c_2) = -c_2 \\ 3) \quad & l-p(c_1+c_2) = c_1 \\ 4) \quad & l-p(c_1+c_2) = c_1-c_2 \end{aligned} \quad ; p \in \mathbf{I} \quad (3.5)$$

Values of l satisfying these equations for $|p| \leq 3$ are displayed in Table 3.1.

Values of l Satisfying Eqn. 3.5				
p	1	2	3	4
3	$3(c_1+c_2)$	$3c_1+2c_2$	$4c_1+3c_2$	$4c_1+2c_2$
2	$2(c_1+c_2)$	$2c_1+c_2$	$3c_1+2c_2$	$3c_1+c_2$
1	c_1+c_2	c_1	$2c_1+c_2$	$2c_1$
0	0	$-c_2$	c_1	c_1-c_2
-1	$-(c_1+c_2)$	$-c_1-2c_2$	$-c_2$	$-2c_2$
-2	$-2(c_1+c_2)$	$-2c_1-3c_2$	$-c_1-2c_2$	$-c_1-3c_2$
-3	$-3(c_1+c_2)$	$-3c_1-4c_2$	$-2c_1-3c_2$	$-2c_1-4c_2$

TABLE 3.1

To use Table 3.1 to determine those values of l at which f_l may be non-zero, we must select a value for N and bear in mind that l must lie in the range $[-d_{0,N-1}, \dots, d_{1,N-1}]$.

Two specific examples are provided below for $c_1 = 2, c_2 = 3$ and $N \leq 4$. For this range of N, p takes on values of $-1, 0, 1$.

Case 1: $N = 3, f_l$ may be non-zero for (from Table 3.1)

$$l = \begin{bmatrix} -(c_1+c_2) & -c_2 & c_1-c_2 & 0 & c_1 & 2c_1 & c_1+c_2 \\ -5 & -3 & -1 & 0 & 2 & 4 & 5 \end{bmatrix}$$

Case 2: $N = 4$, f_l may be non-zero for (from Table 3.1)

$$l = \begin{bmatrix} -c_1-2c_2 & -2c_2 & -(c_1+c_2) & -c_2 & c_1-c_2 & 0 & c_1 & 2c_1 & c_1+c_2 & 2c_1+c_2 \\ -8 & -6 & -5 & -3 & -1 & 0 & 2 & 4 & 5 & 7 \end{bmatrix}$$

Note that in both Case 1 and Case 2, f_l may be non-zero for values of the index l at which $h_{0,-k}$ and $h_{1,k}$ are both identically zero, in particular for $l = -1,4$ in both cases and for $l = -6$ in Case 2. Also note that Case 2 employed all the entries of Table 3.1 for $p = -1,0,1$ while Case 1 did not.

As the Staggered PRT filter generates output values at times $\Delta_k \delta_T$, these unique convolution properties of Staggered PRT sequences may not be readily apparent in the filter's time domain output sequence. In the frequency domain, however, their effects are evident – the Z-Transforms of these convolutions will contain powers of $z = e^{j\omega\delta_T}$ other than $\{ \pm d_{0,0}, \dots, \pm d_{0,N-1}, \pm d_{1,1}, \dots, \pm d_{1,N-1} \}$.

In the following sections of this report, we will employ the notational convenience of denoting all convolutions by an inline $*$. The reader should bear in mind the results of this section for convolution operations involving one or more data sequences with staggered intersample delays.

3.2.3 Lag c_1 and Lag c_2 Power Transfer Functions

Given some wide-sense stationary input sequence $\{x_k\}$ to a linear time-invariant filter, the autocorrelation function of the output sequence $\{y_k\}$ is completely characterized by the filter's power transfer function and the autocorrelation function of the input sequence. Unfortunately, $|G(\omega)|^2$ does not play an exactly analogous role for the Staggered PRT filter. To understand why this is so, we must examine the definition of the autocorrelation function.

For some wide-sense stationary, equispaced, input sequence, $\{x_k\}$, the autocorrelation function of $\{x_k\}$ at lag p is defined to be $R_{xx}(p) \triangleq \mathbf{E}_X \{x_k x_{k+p}^*\}$, where \mathbf{E}_X denotes an expectation with respect to x and a superscript $*$ represents complex conjugation. If $\{x_k\}$ is passed through a linear time-invariant filter with impulse response $\{f_l\}_{l=0}^{N-1}$ and corresponding frequency response $F(\omega)$, the autocorrelation function of the output sequence is given by

$$\begin{aligned} R_{yy}(p) &\triangleq \mathbf{E}_X \left\{ \left[\sum_{l=0}^{N-1} x_{k-l} f_l \right] \left[\sum_{l=0}^{N-1} x_{p+k-l} f_l \right]^* \right\} \\ &= R_{xx} * f_l * f_{-l} \Big|_p \end{aligned}$$

Denoting the power spectra of $\{x_k\}$ and $\{y_k\}$ as $S_{xx}(\omega)$ and $S_{yy}(\omega)$, respectively, we obtain the equivalent result

$$S_{yy}(\omega) = |F(\omega)|^2 S_{xx}(\omega)$$

Since $|F(\omega)|^2$ is phaseless, the phase characteristic of $S_{yy}(\omega)$ is identical to that of $S_{xx}(\omega)$.

For the remainder of the current section of this report, we will use k to denote an offset in sample indices which define the lag at which an autocorrelation function or cross-correlation function is computed. Referring to Figure 3.3, we see that for even values of k (i.e. for values of Δ_k which are integer multiples of (c_1+c_2)), the autocorrelation function of the output sequence $\{y_k\}$ of a Staggered PRT filter is related to the autocorrelation function of the input sequence $\{x_k\}$ in the following manner (recall the preceding section of this report).

$$\begin{aligned} R_{yy}(\Delta_k) &= \mathbf{E}_X \left\{ \left[\left[\sum_{l=0}^{N-1} x_{n-l} h_{0,l} \right] \left[\sum_{l=0}^{N-1} x_{k+n-l} h_{0,l} \right]^* \right]_{n \text{ even}} + \left[\left[\sum_{l=0}^{N-1} x_{n-l} h_{1,l} \right] \left[\sum_{l=0}^{N-1} x_{k+n-l} h_{1,l} \right]^* \right]_{n \text{ odd}} \right\} \\ &= \frac{1}{2} \left(R_{xx} * h_{0,l} * h_{0,-l}^* + R_{xx} * h_{1,l} * h_{1,-l}^* \right) \Big|_k, \quad k \text{ even} \end{aligned}$$

or

$$S_{yy}(\omega) = |G(\omega)|^2 S_{xx}(\omega), \quad \text{for lags } p(c_1+c_2), p \in \mathbf{I}$$

For odd values of k , however, the power transfer functions which relate $S_{yy}(\omega)$ and $S_{xx}(\omega)$ depend upon the particular value of Δ_k as the autocorrelation of $\{y_k\}$ is, in these cases, actually a cross-correlation of the outputs of the two partial response sequences h_0 and h_1 . For the case $\Delta_k = p(c_1+c_2)+c_2, p \in \mathbf{I}$, the autocorrelation function of $\{y_k\}$ is given by

$$\begin{aligned} R_{yy}(\Delta_k) &= \mathbf{E}_X \left\{ \left[\sum_{l=0}^{N-1} x_{n-l} h_{1,l} \right] \left[\sum_{l=0}^{N-1} x_{p(c_1+c_2)+c_2+n-l} h_{0,l} \right]^* \right\} \\ &= R_{xx} * h_{1,l} * h_{0,-l}^* \Big|_k, \quad k \text{ odd}, \Delta_k = p(c_1+c_2)+c_2, p \in \mathbf{I} \end{aligned}$$

or

$$S_{yy}(\omega) = C_0^*(e^{j\omega\delta_T}) C_1(e^{j\omega\delta_T}) S_{xx}(\omega), \quad \text{for lags } p(c_1+c_2)+c_2, p \in \mathbf{I}$$

Similarly, for the case $\Delta_k = p(c_1+c_2)+c_1, p \in \mathbf{I}$, the autocorrelation function of $\{y_k\}$ is given by

$$R_{yy}(\Delta_k) = R_{xx} * h_{0,l} * h_{1,-l}^* \Big|_k, \quad k \text{ odd}, \Delta_k = p(c_1+c_2)+c_1, p \in \mathbf{I}$$

or

$$S_{yy}(\omega) = C_0(e^{j\omega\delta_T}) C_1^*(e^{j\omega\delta_T}) S_{xx}(\omega), \quad \text{for lags } p(c_1+c_2)+c_1, p \in \mathbf{I}$$

Collecting our results, we have the following for $p \in \mathbf{I}$

$$R_{yy}(\Delta_k) = \begin{cases} \frac{1}{2} \left[(R_{xx} * h_{0,l} * h_{0,-l}^*) + (R_{xx} * h_{1,l} * h_{1,-l}^*) \right] \Big|_k, & k \text{ even}, \Delta_k = p(c_1+c_2) \\ R_{xx} * h_{1,l} * h_{0,-l}^* \Big|_k, & k \text{ odd}, \Delta_k = p(c_1+c_2)+c_2 \\ R_{xx} * h_{0,l} * h_{1,-l}^* \Big|_k, & k \text{ odd}, \Delta_k = p(c_1+c_2)+c_1 \end{cases} \quad (3.6)$$

$$S_{yy}(\omega) = \begin{cases} |G(\omega)|^2 S_{xx}(\omega), & \text{for lags } p(c_1+c_2) \\ C_0^*(e^{j\omega\delta_T}) C_1(e^{j\omega\delta_T}) S_{xx}(\omega), & \text{for lags } p(c_1+c_2)+c_2 \\ C_0(e^{j\omega\delta_T}) C_1^*(e^{j\omega\delta_T}) S_{xx}(\omega), & \text{for lags } p(c_1+c_2)+c_1 \end{cases} \quad (3.7)$$

The fact that the Staggered PRT filter has the three effective power transfer functions displayed in equation 3.7 is a direct consequence of the fact that it is not a time-invariant system. The number of effective power transfer functions is equal to the number of positive lags embedded in $\{y_k\}$ which are less in magnitude than the lag corresponding to the basic period of the sampling scheme $-c_1+c_2$.

An analysis similar to that of this section and the preceding one could be performed for a sampling scheme which possessed intersample spacings of

$$\dots, c_{N-1}, c_N, c_1, c_2, \dots, c_{N-1}, c_N, c_1, c_2, \dots$$

relative to some time base, δ_T , where the c_i are relatively prime. In this case, the analogue of the filter depicted in Figure 3.3 would be comprised of N partial response sequences and would possess $N(N-1)+1$ effective power transfer functions. For the case $N>2$, however, certain intersample delays could possess multiple effective power transfer functions. As an example, if $N=3$ and $c_1=2, c_2=3, c_3=5$, lags of c_3 and c_1+c_2 would both correspond to a delay of $5\delta_T$; and the net power transfer function for estimates of the autocorrelation function of the filter's output at a delay of $5\delta_T$ would be the average of the lag c_1+c_2 and lag c_3 effective power transfer functions - if all available sample pairs in $\{y_k\}$ with an intersample spacing of $5\delta_T$ were to be used for the estimate.

For lags other than $p(c_1+c_2)$, equation 3.7 shows that the transfer functions of the Staggered PRT filter may have phase characteristics that are not identically zero. In designing Staggered PRT filters, then, it is highly desirable that the magnitude *and* phase characteristics of h_0 and h_1 be closely matched, so that filter's effective transfer function appears to be independent of the particular lag at which an autocorrelation value of the filter's output sequence is to be estimated. The interaction of the phase responses of $C_0^*(e^{j\omega\delta_T})C_1(e^{j\omega\delta_T})$ and $C_0(e^{j\omega\delta_T})C_1^*(e^{j\omega\delta_T})$ with pulse-pair velocity estimation will be discussed in section 3.3.2.

3.3 PROPERTIES OF THE $C_i(z)$ AND EFFECTIVE POWER TRANSFER FUNCTIONS

The purpose of this section of the report is to provide a qualitative discussion of some of the frequency-domain properties of the Staggered PRT filters.

3.3.1 Z-Plane Zero Distribution of $|G(\omega)|^2$

When the $h_{i,k}$ are real, the z-plane zeroes of $|G(\omega)|^2$ (more precisely, the zeroes of $C_0(z)C_0(z^{-1}) + C_1(z)C_1(z^{-1})$) display both conjugate symmetry and reciprocal symmetry about the unit circle. To see this, note that real $h_{i,k}$ yield $C_i(z)$ with zeroes occurring in conjugate pairs. The zeroes of $C_i(z^{-1})$ will be the inverses of those of $C_i(z)$, hence the zeroes of $C_i(z)C_i(z^{-1})$ – the totality of the zeroes of $C_i(z)$ and $C_i(z^{-1})$ – will possess conjugate and reciprocal symmetry. Zeroes of $|G(\omega)|^2$ will correspond to one of two cases. Either $C_0(z)C_0(z^{-1}) = C_1(z)C_1(z^{-1}) = 0$ or $C_0(z)C_0(z^{-1}) = -C_1(z)C_1(z^{-1})$. In both cases, conjugate and reciprocal symmetry follow from the properties of the $C_i(z)C_i(z^{-1})$, $i = 0,1$. These symmetries result in a $|G(\omega)|^2$ which is a real, even, function of ω . Examples of these z-plane zero distributions will be presented subsequently.

3.3.2 Phase Responses of $C_0^*(e^{j\omega\delta_T})C_1(e^{j\omega\delta_T})$ and $C_0(e^{j\omega\delta_T})C_1^*(e^{j\omega\delta_T})$

As mentioned earlier, the filter's effective power transfer functions for lags other than $p(c_1+c_2)$, $p \in \mathbf{I}$ may have non-zero phase characteristics. The goal of the next several paragraphs is to describe conditions on the selections of stagger ratio and filter length which are sufficient to guarantee linear phase characteristics for $C_0^*(e^{j\omega\delta_T})C_1(e^{j\omega\delta_T})$ and $C_0(e^{j\omega\delta_T})C_1^*(e^{j\omega\delta_T})$. In the present context, we need only discuss one of these transfer functions, $C_0^*(e^{j\omega\delta_T})C_1(e^{j\omega\delta_T})$, as phase linearity of one guarantees phase linearity of the other. A linear phase characteristic is desirable, as its only effect is to induce a known time shift into the autocorrelation sequence at the filter's output.

Referring to equations 3.6 and 3.7, we see that

$$C_0^*(e^{j\omega\delta_T})C_1(e^{j\omega\delta_T}) = \mathbf{Z}\{h_{1,l} * h_{0,-l}^*\} \Big|_{z=e^{j\omega\delta_T}}$$

This is the lag c_2 effective power transfer function, and it will possess a linear phase characteristic if $f_m \triangleq h_{1,l} * h_{0,-l}^*$ is a time function which is real and even with respect to some time instant.

If we examine the sampling instants, $m\delta_T$, $m \in \mathbf{I}$, at which f_m may be non-zero (e.g. via Table 3.1); and then successively difference those sampling times to obtain the intersample delays in f_m , we see the following pattern (differences are displayed left to right from the most negative pair of sampling instants at which f_m

may be non-zero to the most positive pair).

N=2:

$$c_1, c_2 - c_1, c_1$$

N=3:

$$c_1, c_1, c_2 - c_1, c_1, c_1, c_2 - c_1$$

N=4:

$$c_1, c_2 - c_1, c_1, c_1, c_2 - c_1, c_1, c_1, c_2 - c_1, c_1$$

N=5:

$$c_1, c_1, c_2 - c_1, c_1, c_1, c_2 - c_1, c_1, c_1, c_2 - c_1, c_1, c_1, c_2 - c_1$$

N=6:

$$c_1, c_2 - c_1, c_1, c_1, c_2 - c_1, c_1, c_1, c_2 - c_1, c_1, c_1, c_2 - c_1, c_1, c_1, c_2 - c_1, c_1$$

For values of $N \leq 6$, f_m only possesses even intersample delays for even values of N . We conjecture that f_m possesses even intersample delays for all even values of N and non-even intersample delays for all odd values of N . For $N = 2, 4, 6$ the central intersample delay of $c_2 - c_1$ is centered at time $-(c_2 - c_1)\delta_T / 2$, which implies the possibility of a linear phase characteristic of $\exp(+j\omega(c_2 - c_1)\delta_T / 2)$ for $C_0^*(e^{j\omega\delta_T})C_1(e^{j\omega\delta_T})$. A linear phase characteristic will be obtained if the values of f_m possess even symmetry about the central intersample delay.

We note that the convolution of two sequences with odd symmetry always results in a sequence with even symmetry. This may be easily demonstrated. Consider two, finite energy, equispaced data sequences $\{g_{i,k}\}_{k=-\infty}^{\infty}$, $i = 0, 1$ which possess odd symmetry - $g_{i,k} = -g_{i,-k}$, $i = 0, 1$. Their convolution, evaluated at some index l is given by

$$\begin{aligned} g_{0,k} * g_{1,k} \Big|_l &= \sum_{k=-\infty}^{\infty} g_{1,k} g_{0,l-k} = \sum_{k=-\infty}^{\infty} g_{1,-k} g_{0,k-l} \\ &= \sum_{k=+\infty}^{-\infty} g_{1,k} g_{0,-l-k} = g_{0,k} * g_{1,k} \Big|_{-l} \end{aligned}$$

As will be seen, it is often the case that the design of high-pass Staggered PRT filters with narrow stopbands (*e.g.* clutter filters) results in partial response sequences which possess odd symmetry for even values of N , in the sense that

$$h_{i,0} = -h_{i,N-1}, h_{i,1} = -h_{i,N-2}, \dots, i = 0, 1$$

Combining the results of the preceding several paragraphs, it is apparent for even values of N and partial response sequences with odd symmetry that the lag c_1 and

lag c_2 effective transfer functions – $C_0(e^{j\omega\delta_T})C_1^*(e^{j\omega\delta_T})$ and $C_0^*(e^{j\omega\delta_T})C_1(e^{j\omega\delta_T})$ – will possess linear phase characteristics of $\exp(-j\omega(c_2-c_1)\delta_T/2)$ and $\exp(+j\omega(c_2-c_1)\delta_T/2)$, respectively.

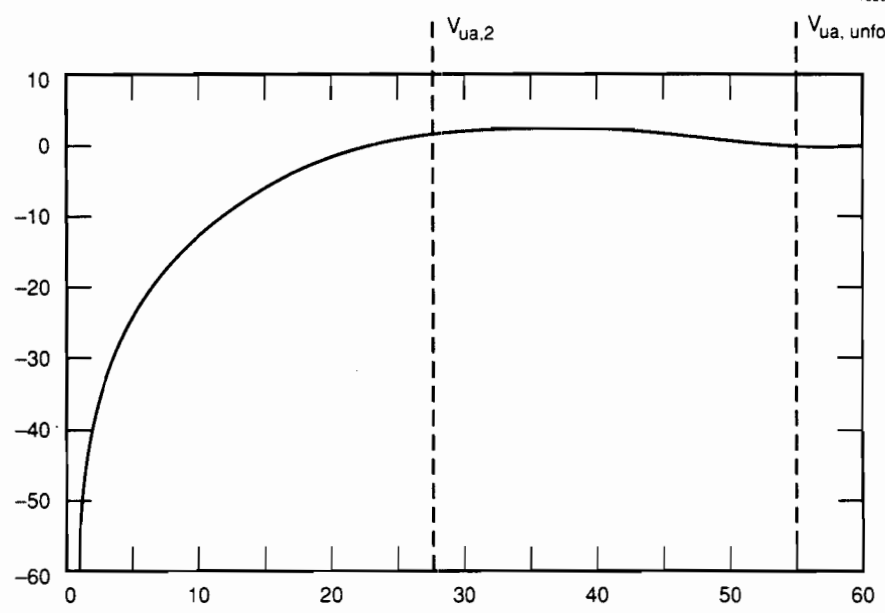
Figures 3.4 through 3.7 display these phase properties for $N=3$ and $N=4$ with $c_1=1$ and $c_2=2$. The particular values for c_1 and c_2 were selected for the purpose of demonstration, only. Figures 3.4 and 3.5 display $|G(\omega)|^2$ and $C_0(e^{j\omega\delta_T})C_1^*(e^{j\omega\delta_T})$, respectively, for the case $N=3$; Figures 3.6 and 3.7 provide the corresponding plots for the case $N=4$ (and partial response sequences with odd symmetry). The format for these plots is as follows. The abscissa is the positive portion of the Nyquist interval in Doppler velocity space, for a 3 GHz (S-Band) radar with $\delta_T = 0.45455$ ms. The corresponding Nyquist velocity is 55 m/s. The left-hand ordinate axis is power gain in dB, while the right-hand ordinate axis in Figures 3.5 and 3.7 is phase shift in degrees. The block of text below the plot on the left displays the stagger ratio, radar constants, δ_T and N . The block of text below the plot on the right displays the parameters used in designing the partial response sequences – design techniques are the topic of subsequent sections of this report. Figures 3.4 and 3.6 also are marked to indicate the Nyquist velocities corresponding to PRT's of $c_1\delta_T$, $c_2\delta_T$ and δ_T . Those markings are $V_{ua,1}$, $V_{ua,2}$ and $V_{ua,unfolded}$, respectively. As $c_1=1$ for these examples, the labels $V_{ua,1}$ and $V_{ua,unfolded}$ are overlaid.

Comparing Figures 3.4 and 3.5, we see that the gain characteristics of $|G(\omega)|^2$ and $C_0(e^{j\omega\delta_T})C_1^*(e^{j\omega\delta_T})$ are well matched. This is desirable as it implies that the Staggered PRT filter's gain effects on the power spectrum of its output will be essentially independent of the particular output value, or collection of values, examined. As expected, however, the phase response of $C_0(e^{j\omega\delta_T})C_1^*(e^{j\omega\delta_T})$ is non-linear. The non-linearity is especially benign for this example – more realistic values of $c_1:c_2$ (e.g. 2:3, 3:4, 3:5, 5:7, etc.) tend to exacerbate the non-linearity.

In comparing Figures 3.6 and 3.7, the gain characteristics of $|G(\omega)|^2$ and $C_0(e^{j\omega\delta_T})C_1^*(e^{j\omega\delta_T})$ may be observed to differ. For even values of N , this disparity can become acute for more realistic values of $c_1:c_2$. The phase response of $C_0(e^{j\omega\delta_T})C_1^*(e^{j\omega\delta_T})$ is linear, with the expected slope of $-90(c_2-c_1)$ degrees per π radians of digital frequency.

Figures 3.8 through 3.10 provide an example of velocity estimation from the autocorrelation sequence of the staggered PRT filter's output. De-aliasing is accomplished as follows:

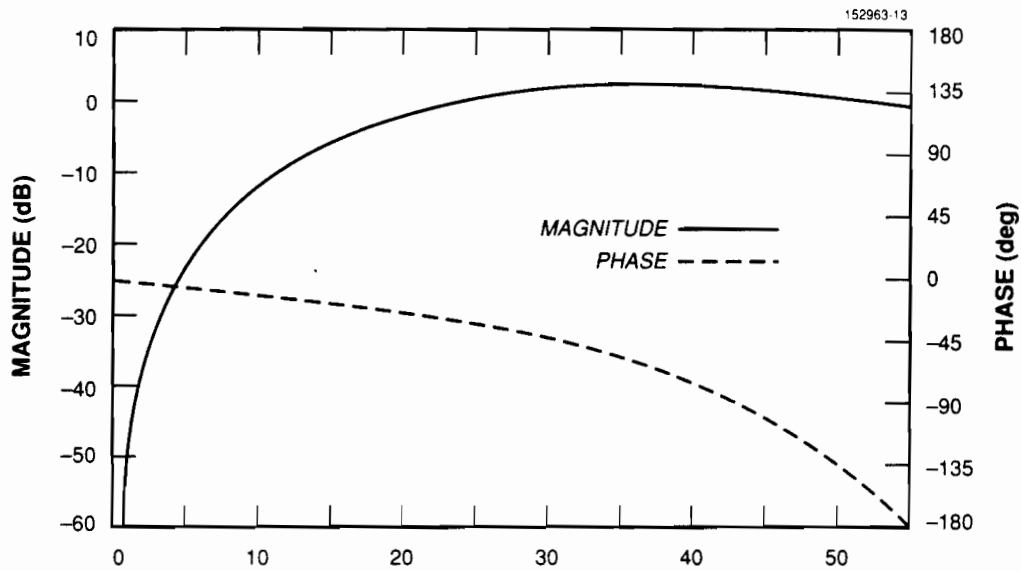
- 1) a lookup table containing all combinations of rate $c_1\delta_T$ and $c_2\delta_T$ velocity folds for velocities in the range $\pm v_u = \pm\lambda(4\delta_T)^{-1}$ is precomputed "offline" – Table 3.2 is an example of the lookup table for $c_1=2$, $c_2=3$ and $v_u=1$ m/s (see Figure 1.4, also);



(MAGNITUDE)² (dB) vs DOPPLER VELOCITY (m/s)
FILTER ID: 123

STAGGER RATIO 1:2	AUTOCORRELATION-BASED DESIGN:
δ_T IS 0.45455 ms	INPUT S/C POWER RATIO: -10.0 dB
PRF 1 = 2200.0 Hz, PRF 2 = 1100.0 Hz	OUTPUT S/C POWER RATIOS: 71.6 dB,
3 FILTER COEFFICIENTS	71.6 dB
RADAR FREQUENCY IS 3.00000 GHz	NORMALIZED CLUTTER WIDTH: 0.00273
	NORMALIZED W-SPECTRUM BREAKPOINTS:
	0.00000 0.00200 0.85000 1.00000

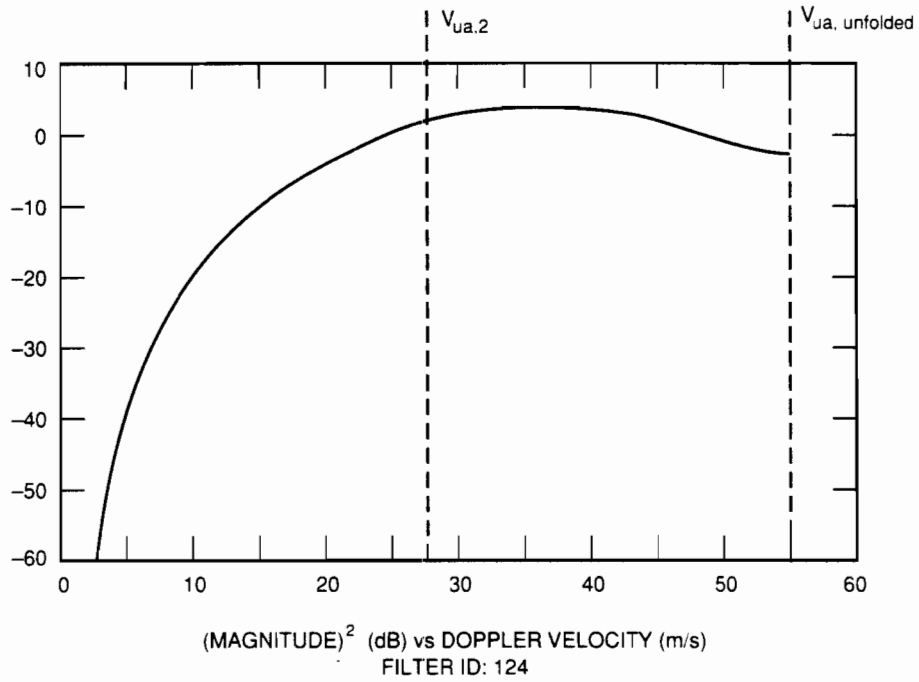
Figure 3.4: $|G(\omega)|^2$ for a staggered PRT filter, $N=3$



MAGNITUDE AND PHASE FUNCTIONS FOR $C_0C_1^*$ vs DOPPLER VELOCITY (m/s)
 FILTER ID: 123

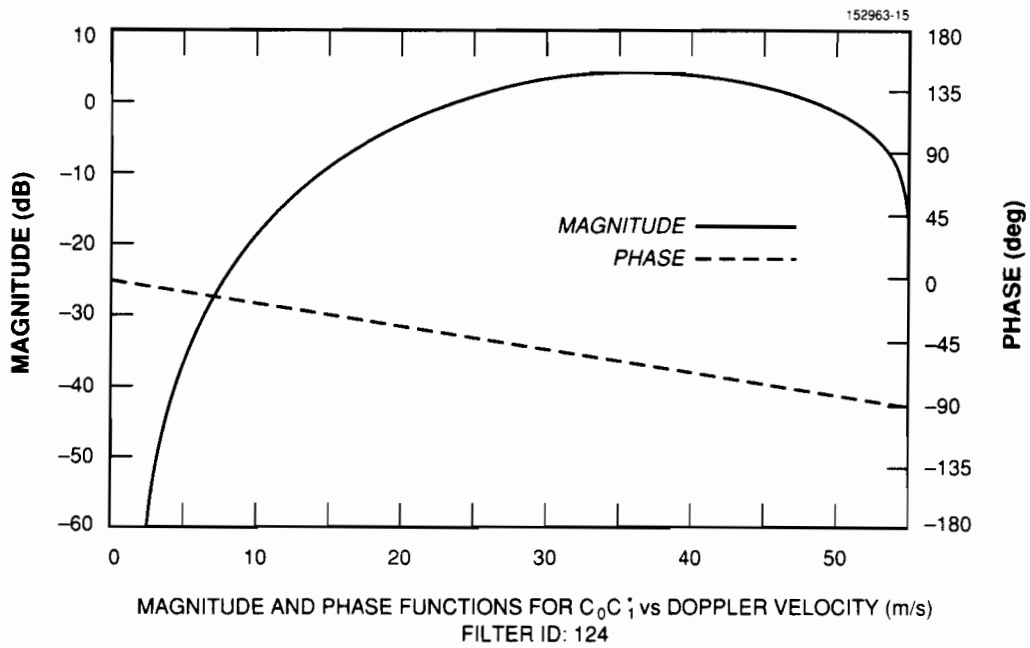
STAGGER RATIO 1:2	AUTOCORRELATION-BASED DESIGN:
δ_T IS 0.45455 ms	INPUT S/C POWER RATIO: -10.0 dB
PRF 1 = 2200.0 Hz, PRF 2 = 1100.0 Hz	OUTPUT S/C POWER RATIOS: 71.6 dB,
3 FILTER COEFFICIENTS	71.6 dB
RADAR FREQUENCY IS 3.00000 GHz	NORMALIZED CLUTTER WIDTH: 0.00273
	NORMALIZED W-SPECTRUM BREAKPOINTS:
	0.00000 0.00200 0.85000 1.00000

Figure 3.5: Magnitude and phase functions for $C_0C_1^*$, $N=3$



STAGGER RATIO 1:2	AUTOCORRELATION-BASED DESIGN:
δ_T IS 0.45455 ms	INPUT S/C POWER RATIO: -10.0 dB
PRF 1 = 2200.0 Hz, PRF 2 = 1100.0 Hz	OUTPUT S/C POWER RATIOS: 109.3 dB,
4 FILTER COEFFICIENTS	110.5 dB
RADAR FREQUENCY IS 3.00000 GHz	NORMALIZED CLUTTER WIDTH: 0.00273
	NORMALIZED W-SPECTRUM BREAKPOINTS:
	0.00000 0.00200 0.85000 1.00000

Figure 3.6: $|G(\omega)|^2$ for a staggered PRT filter, $N=4$



STAGGER RATIO 1:2	AUTOCORRELATION-BASED DESIGN:
δ_T IS 0.45455 ms	INPUT S/C POWER RATIO: -10.0 dB
PRF 1 = 2200.0 Hz, PRF 2 = 1100.0 Hz	OUTPUT S/C POWER RATIOS: 109.3 dB,
4 FILTER COEFFICIENTS	110.5 dB
RADAR FREQUENCY IS 3.00000 GHz	NORMALIZED CLUTTER WIDTH: 0.00273
	NORMALIZED W-SPECTRUM BREAKPOINTS:
	0.00000 0.00200 0.85000 1.00000

Figure 3.7: Magnitude and phase functions for $C_0C_1^*$, $N=4$

Folding Table: $c_1=2$, $c_2=3$ and $v_u=1$ m/s						
Rate $c_1\delta_T$	Number of Folds	1	0	0	0	1
	Correction (m/s)	-1	0	0	0	+1
Rate $c_2\delta_T$	Number of Folds	1	1	0	1	1
	Correction (m/s)	-2/3	-2/3	0	2/3	2/3
TABLE 3.2						

- 2) potentially aliased lag c_1 and lag c_2 velocity estimates, \hat{v}_1 and \hat{v}_2 respectively, are generated from the filter's output sequence;
- 3) using the table computed in (1), the magnitude of the difference in each combination of corrected estimates, $|\hat{v}_{1c} - \hat{v}_{2c}|$, is computed; and
- 4) the final velocity estimate is the average of the \hat{v}_{1c} and \hat{v}_{2c} which minimized $|\hat{v}_{1c} - \hat{v}_{2c}|$ in (3).

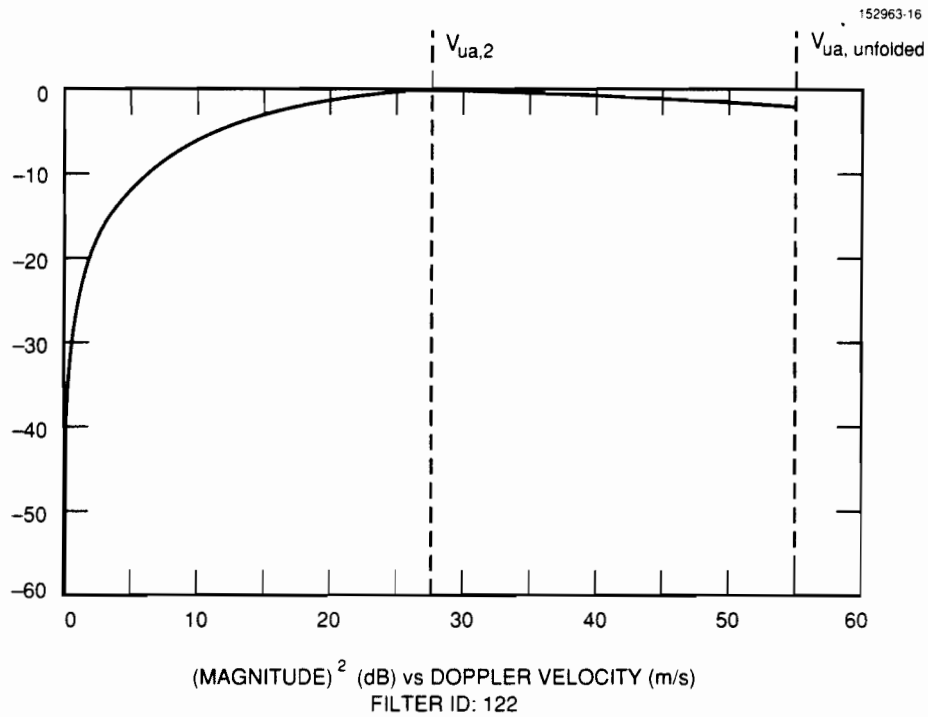
Figure 3.8a displays $|G(\omega)|^2$ for a Staggered PRT filter with $c_1=1$, $c_2=2$ and $N=2$. v_u is 55 m/s. The filter was designed using the OSCRM design technique which will be described in section 4.3. Figure 3.8b displays the lag c_1 transfer function $C_0(e^{j\omega\delta_T})C_1^*(e^{j\omega\delta_T})$. N is even and the h_i are odd, in the sense that $h_{i,0}=-h_{i,1}$, hence $C_0(e^{j\omega\delta_T})C_1^*(e^{j\omega\delta_T})$ possesses a linear phase response. Figure 3.9a displays the uncorrected lag c_1 (solid line) and lag c_2 (dashed line) velocity estimates versus true velocity – the weather spectrum width is 1 m/s for this example. These were computed via equation 1.4c as $-\lambda(4\pi c_1\delta_T)^{-1}\arg[\hat{R}_{yy}(c_1\delta_T)]$ and $-\lambda(4\pi c_2\delta_T)^{-1}\arg[\hat{R}_{yy}(c_2\delta_T)]$, respectively. Properly aliased velocities would have resulted in line segments with slopes of unity in this figure. Instead, the slopes are $1/2$ and $5/2$.

Noting that the phase responses of $C_0(e^{j\omega\delta_T})C_1^*(e^{j\omega\delta_T})$ and $C_0^*(e^{j\omega\delta_T})C_1(e^{j\omega\delta_T})$ correspond to an advance and delay of $1/2\delta_T$, respectively, we may instead compute the lag c_1 and lag c_2 velocity estimates as

$$\hat{v}_1 = \frac{-\lambda}{4\pi(c_1 - 1/2)\delta_T} \arg[\hat{R}_{yy}(c_1\delta_T)] \quad (3.8a)$$

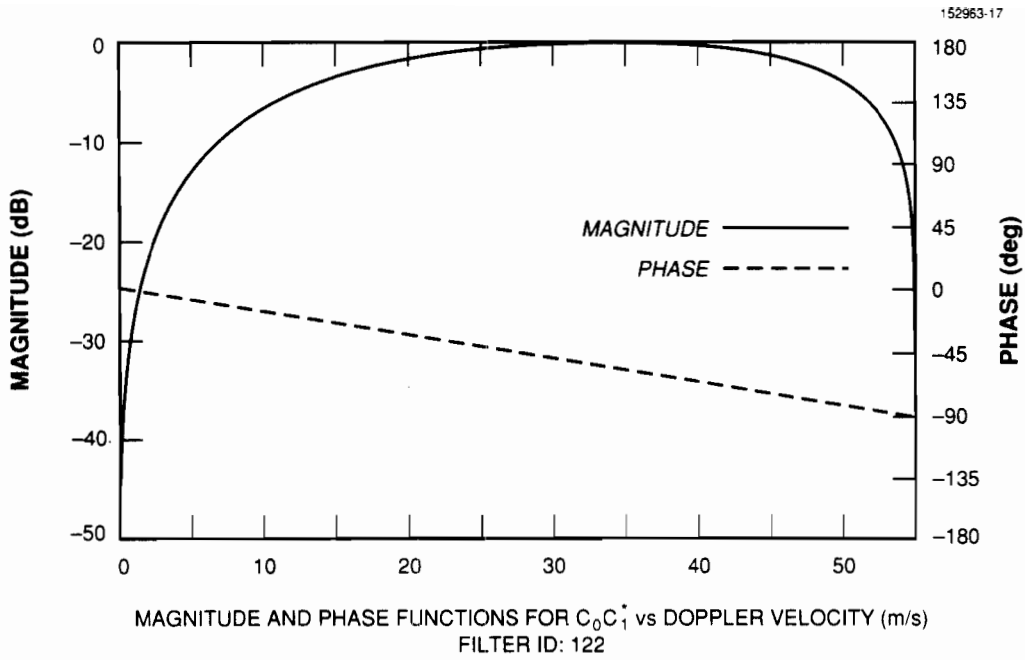
$$\hat{v}_2 = \frac{-\lambda}{4\pi(c_2 + 1/2)\delta_T} \arg[\hat{R}_{yy}(c_2\delta_T)] \quad (3.8a)$$

to account for the offset in R_{yy} relative to R_{xx} . The resulting estimates are plotted in Figure 3.9b. These estimates are properly aliased, with the exception that the lag c_2 estimate folds at approximately 22 m/s, rather than at $1/2v_u=27.5$ m/s. The cause of the premature fold is currently a mystery; as it occurs in a velocity region where $|C_0(e^{j\omega\delta_T})C_1^*(e^{j\omega\delta_T})|$ is not constant, a partial explanation may lie in



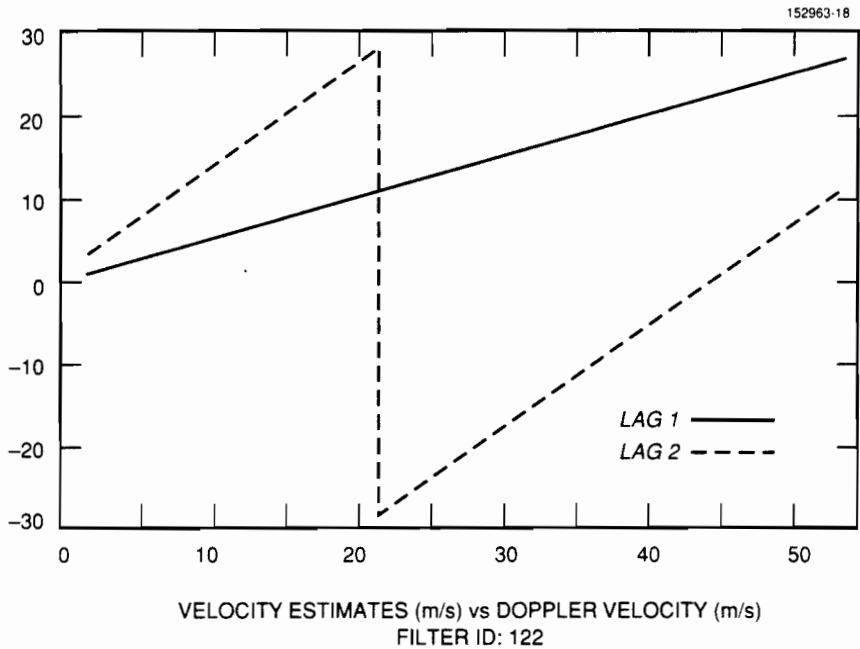
STAGGER RATIO 1:2	AUTOCORRELATION-BASED DESIGN:
δ_T IS 0.45455 ms	INPUT S/C POWER RATIO: -10.0 dB
PRF 1 = 2200.0 Hz, PRF 2 = 1100.0 Hz	OUTPUT S/C POWER RATIOS: 28.6 dB,
2 FILTER COEFFICIENTS	34.0 dB
RADAR FREQUENCY IS 3.00000 GHz	NORMALIZED CLUTTER WIDTH: 0.00273
	NORMALIZED W-SPECTRUM BREAKPOINTS:
	0.00000 0.00200 0.85000 1.00000

Figure 3.8a: $|G(\omega)|^2$ for an OSCRM design, $c_1=1$, $c_2=2$ and $N=2$



STAGGER RATIO 1:2	AUTOCORRELATION-BASED DESIGN:
δ_T IS 0.45455 ms	INPUT S/C POWER RATIO: -10.0 dB
PRF 1 = 2200.0 Hz, PRF 2 = 1100.0 Hz	OUTPUT S/C POWER RATIOS: 28.6 dB,
2 FILTER COEFFICIENTS	34.0 dB
RADAR FREQUENCY IS 3.00000 GHz	NORMALIZED CLUTTER WIDTH: 0.00273
	NORMALIZED W-SPECTRUM BREAKPOINTS:
	0.00000 0.00200 0.85000 1.00000

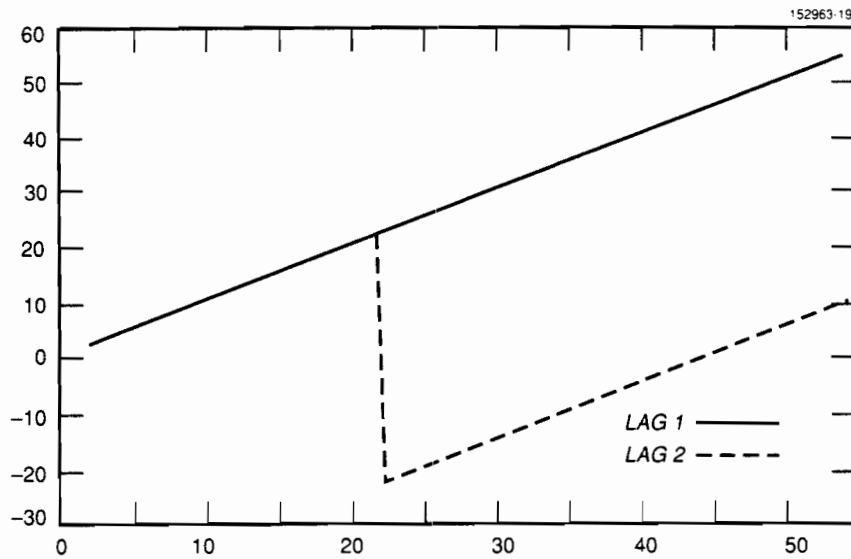
Figure 3.8b: Lag c_1 transfer function for OSCR design of figure 3.8a



WEATHER SPECTRUM WIDTH IS 1.0 m/s
 LAG 1 RESET TO 1.0
 LAG 2 RESET TO 2.0
 STAGGER RATIO 1:2
 δ_T IS 0.45455 ms
 PRF 1 = 2200.0 Hz, PRF 2 = 1100.0 Hz
 2 FILTER COEFFICIENTS
 RADAR FREQUENCY IS 3.00000 GHz

NYQUIST SPECTRAL FOLDING ENFORCED
 AUTOCORRELATION-BASED DESIGN:
 INPUT S/C POWER RATIO: -10.0 dB
 OUTPUT S/C POWER RATIOS: 28.6 dB,
 34.0 dB
 NORMALIZED CLUTTER WIDTH: 0.00273
 NORMALIZED W-SPECTRUM BREAKPOINTS:
 0.00000 0.00200 0.85000 1.00000

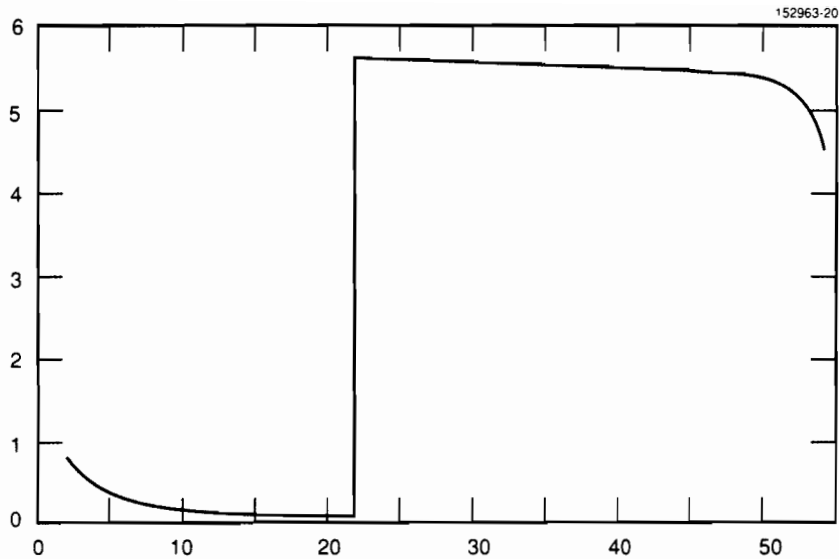
Figure 3.9a: Uncorrected lag c_1 and c_2 velocity estimates from filter of figure 3.8,
 $\sigma_v = 1$ m/s



VELOCITY ESTIMATES (m/s) vs DOPPLER VELOCITY (m/s)
 FILTER ID: 122

WEATHER SPECTRUM WIDTH IS 1.0 m/s	NYQUIST SPECTRAL FOLDING ENFORCED
LAG 1 RESET TO 0.5	AUTOCORRELATION-BASED DESIGN:
LAG 2 RESET TO 2.5	INPUT S/C POWER RATIO: -10.0 dB
STAGGER RATIO 1:2	OUTPUT S/C POWER RATIOS: 28.6 dB,
δ_T IS 0.45455 ms	34.0 dB
PRF 1 = 2200.0 Hz, PRF 2 = 1100.0 Hz	NORMALIZED CLUTTER WIDTH: 0.00273
2 FILTER COEFFICIENTS	NORMALIZED W-SPECTRUM BREAKPOINTS:
RADAR FREQUENCY IS 3.00000 GHz	0.00000 0.00200 0.85000 1.00000

Figure 3.9b: Corrected lag c_1 and c_2 velocity estimates from filter of figure 3.8,
 $\sigma_v = 1$ m/s



MEAN VELOCITY ESTIMATE ERROR (m/s) vs MEAN WEATHER VELOCITY (m/s)
 FILTER ID: 122

WEATHER SPECTRUM WIDTH IS 1.0 m/s.	2 FILTER COEFFICIENTS
LAG 1 RESET TO 0.5	RADAR FREQUENCY IS 3.00000 GHz
LAG 2 RESET TO 2.5	NYQUIST SPECTRAL FOLDING ENFORCED
STAGGER RATIO 1:2	AUTOCORRELATION-BASED DESIGN:
δ_T IS 0.45455 ms	INPUT S/C POWER RATIO: -10.0 dB
PRF 1 = 2200.0 Hz, PRF 2 = 1100.0 Hz	OUTPUT S/C POWER RATIOS: 28.6 dB,
MINIMUM DISPLAYED	34.0 dB
VELOCITY: 2.0 m/s	NORMALIZED CLUTTER WIDTH: 0.00273
	NORMALIZED W-SPECTRUM BREAKPOINTS:
	0.00000 0.00200 0.85000 1.00000

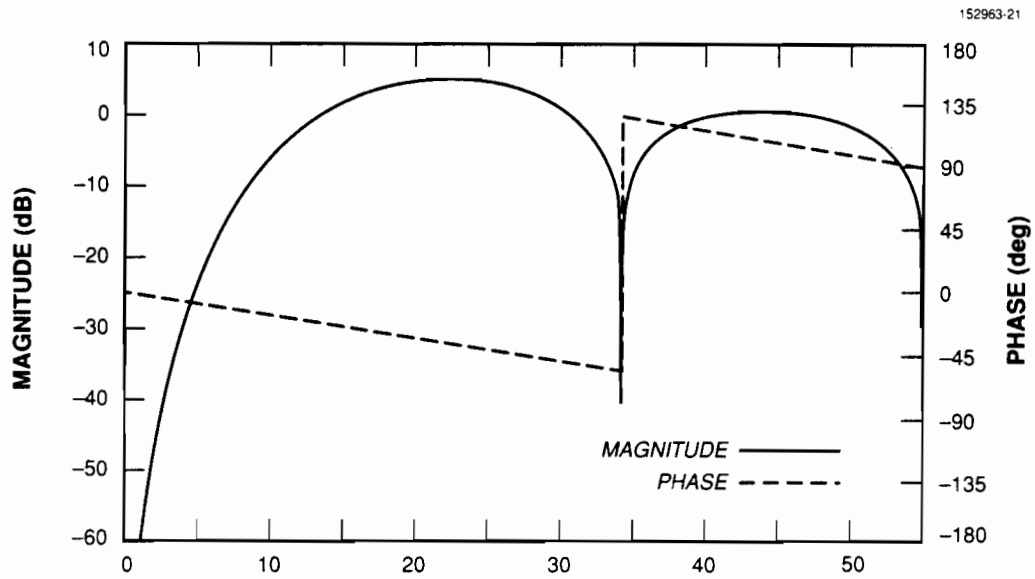
VELOCITY DE-ALIASING OPERATING UPON LAG 1 VELOCITY ESTIMATES AT EACH PULSE RATE.

Figure 3.10: Errors in final de-aliased estimates generated from lag c_1 and c_2 estimates of figure 3.9b, $\sigma_v = 1$ m/s

distortion of the weather spectrum. The effect of the premature fold is a positive bias of approximately 11 m/s (2(27.5-22)) for the aliased lag c_2 estimate. Velocity de-aliasing performs properly, however – the errors in the final de-aliased estimates are displayed in Figure 3.10. Note that the averaging performed in step (4) reduces the bias in the unfolded estimate to 5.5 m/s for velocities greater than 22 m/s. A more intelligent de-aliasing algorithm, with knowledge of the lag c_1 and lag c_2 transfer functions, could further reduce that bias.

For those $C_0(e^{j\omega\delta_T})C_1^*(e^{j\omega\delta_T})$ which meet all of the aforementioned criteria for linear phase, but possesses zeroes with odd multiplicity on the unit circle, 180° discontinuities will be introduced into the otherwise linear phase characteristic. In such cases, equations 3.8 will not yield properly aliased estimates. Figure 3.11 provides an example of a $C_0(e^{j\omega\delta_T})C_1^*(e^{j\omega\delta_T})$ with a discontinuous, "linear", phase characteristic. This is an OSCRM design with $c_1=2$, $c_2=3$ and $N=4$. The unambiguous velocity is 55 m/s and the weather spectrum width is 1 m/s. Figure 3.12 displays the lag c_1 and lag c_2 velocity estimates of equations 3.8. The effects of the phase discontinuity in $C_0(e^{j\omega\delta_T})C_1^*(e^{j\omega\delta_T})$ at ≈ 34 m/s is clearly evident – note that correctly aliased estimates are obtained for velocities below the phase discontinuity, although the lag c_2 estimate folds prematurely at ≈ 15 m/s rather than at $18\frac{1}{3}$ m/s. The appropriate folding table for this stagger ratio and unambiguous velocity is Table 3.2 with the entries labeled *Correction (m/s)* all scaled by 55. Applying the de-aliasing algorithm to these estimates, we obtain the final estimate errors shown in Figure 3.13. The errors in the lag c_1 and lag c_2 estimates of Figure 3.12 result in the selection of an improper additive correction (-55 m/s in this case) for velocities in the range of 34 to 55 m/s. Empirically, discontinuous "linear" phase characteristics like that of Figure 3.11 are more common than truly linear phase characteristics like that of Figure 3.8b.

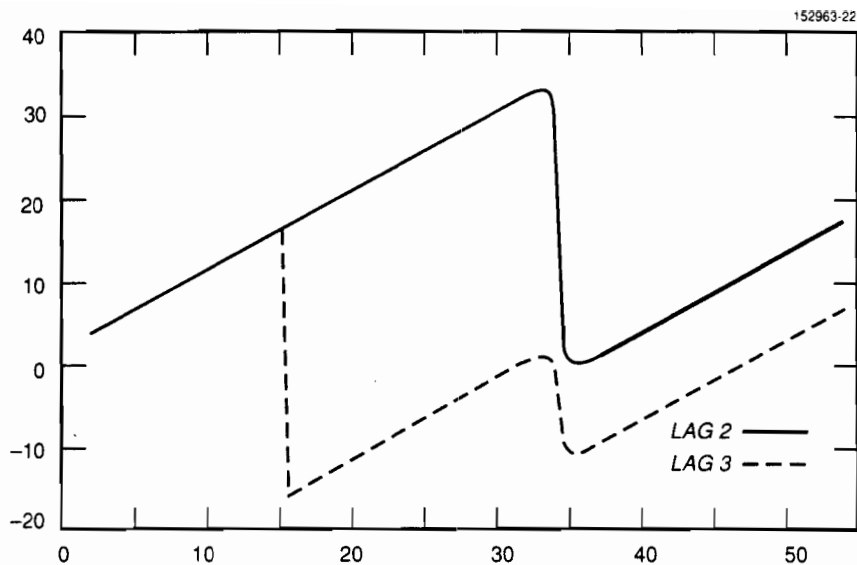
This section of the report may be summarized as follows. For Staggered PRT clutter filters, even values of N generally result in linear phase characteristics for the lag c_1 and lag c_2 effective power transfer functions and disparities in the gain characteristics of $|G(\omega)|^2$ and $C_0(e^{j\omega\delta_T})C_1^*(e^{j\omega\delta_T})$. When the phase characteristics are truly linear, equations 3.8 will yield properly aliased lag c_1 and lag c_2 velocity estimates. Odd values of N generally result in non-linear phase characteristics for the lag c_1 and lag c_2 effective power transfer functions and good agreement among the gain characteristics of $|G(\omega)|^2$ and $C_0(e^{j\omega\delta_T})C_1^*(e^{j\omega\delta_T})$ – as mentioned in section 3.2, odd N and a real $h_0=h_1$ guarantee that $|C_0(e^{j\omega\delta_T})|=|C_1^*(e^{j\omega\delta_T})|$ and hence that $|G(\omega)|^2=|C_0(e^{j\omega\delta_T})C_1^*(e^{j\omega\delta_T})|$. All other things held constant, increasing the values of N , c_1 or c_2 tend to exacerbate phase non-linearities and magnitude response mismatches in a filter design.



MAGNITUDE AND PHASE FUNCTIONS FOR C_0C_1 vs DOPPLER VELOCITY (m/s)
 FILTER ID: 234

STAGGER RATIO 2:3	AUTOCORRELATION-BASED DESIGN:
δ_T IS 0.45455 ms	INPUT S/C POWER RATIO: -10.0 dB
PRF 1 = 1100.0 Hz, PRF 2 = 733.3 Hz	OUTPUT S/C POWER RATIOS: 95.8 dB,
4 FILTER COEFFICIENTS	96.1 dB
RADAR FREQUENCY IS 3.00000 GHz	NORMALIZED CLUTTER WIDTH: 0.00273
	NORMALIZED W-SPECTRUM BREAKPOINTS:
	0.00000 0.00200 0.85000 1.00000

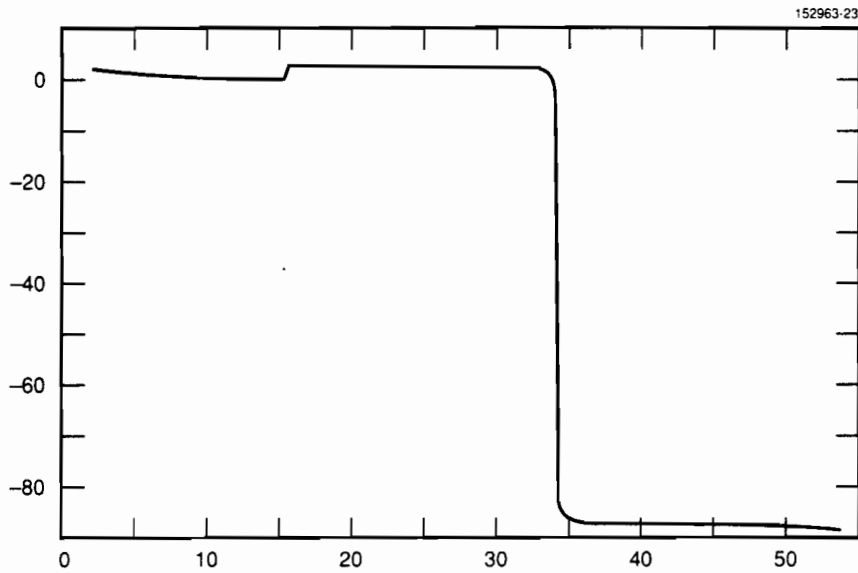
Figure 3.11: Lag c_1 transfer function for OSCR design, $c_1=2$, $c_2=3$ and $N=4$



VELOCITY ESTIMATES (m/s) vs DOPPLER VELOCITY (m/s)
 FILTER ID: 234

WEATHER SPECTRUM WIDTH IS 1.0 m/s	NYQUIST SPECTRAL FOLDING ENFORCED
LAG 2 RESET TO 1.5	AUTOCORRELATION-BASED DESIGN:
LAG 3 RESET TO 3.5	INPUT S/C POWER RATIO: -10.0 dB
STAGGER RATIO 2:3	OUTPUT S/C POWER RATIOS: 95.8 dB,
δ_T IS 0.45455 ms	96.1 dB
PRF 1 = 1100.0 Hz, PRF 2 = 733.3 Hz	NORMALIZED CLUTTER WIDTH: 0.00273
4 FILTER COEFFICIENTS	NORMALIZED W-SPECTRUM BREAKPOINTS:
RADAR FREQUENCY IS 3.00000 GHz	0.00000 0.00200 0.85000 1.00000

Figure 3.12: "Corrected" lag c_1 and c_2 velocity estimates from filter of figure 3.11,
 $\sigma_v = 1$ m/s



MEAN VELOCITY ESTIMATE ERROR (m/s) vs MEAN WEATHER VELOCITY (m/s)
 FILTER ID: 234

WEATHER SPECTRUM WIDTH IS 1.0 m/s	4 FILTER COEFFICIENTS
VELOCITY DE-ALIASING OPERATING	RADAR FREQUENCY IS 3.00000 GHz
UPON LAG 1 VELOCITY ESTIMATES	NYQUIST SPECTRAL FOLDING ENFORCED
AT EACH PULSE RATE	AUTOCORRELATION-BASED DESIGN:
LAG 2 RESET TO 1.5	INPUT S/C POWER RATIO: -10.0 dB
LAG 3 RESET TO 3.5	OUTPUT S/C POWER RATIOS: 95.8 dB,
MINIMUM DISPLAYED VELOCITY: 2.0 m/s	96.1 dB
STAGGER RATIO 2:3	NORMALIZED CLUTTER WIDTH: 0.00273
δ_T IS 0.45455 ms	NORMALIZED W-SPECTRUM BREAKPOINTS:
PRF 1 = 1100.0 Hz, PRF 2 = 733.3 Hz	0.00000 0.00200 0.85000 1.00000

Figure 3.13: Errors in final de-aliased estimates generated from lag c_1 and c_2 estimates of figure 3.12, $\sigma_v = 1$ m/s

3.3.3 Uncontrollable Zeroes in the $C_i(z)$

In contrast to the design of FIR filters operating on equispaced data, not all of the Staggered PRT filter's z-plane zeroes may be directly specified. The number of z-plane zeroes for an equispaced FIR filter is equal to the number of coefficients it possesses, excluding the coefficient at lag zero which is a scalar multiplicative factor, as shown below.

$$A(z) = a_0(1 + a_1z^{-1} + a_2z^{-2} + \dots + a_{N-1}z^{N-1})$$

In selecting the coefficients for such a filter, then, the designer may directly specify the location of each z-plane zero. A staggered PRT filter, however, generally possesses many more zeroes than filter coefficients. With a stagger of 3:5 (*i.e.* $c_1=3, c_2=5$), for example, the $C_i(z)$ have the form displayed below.

$$C_0(z) = h_{0,0} + h_{0,1}z^{-5} + h_{0,2}z^{-8} + h_{0,3}z^{-13} + \dots + h_{0,N-1}z^{-d_{0,N-1}}$$

$$C_1(z) = h_{1,0} + h_{1,1}z^{-3} + h_{1,2}z^{-8} + h_{1,3}z^{-11} + \dots + h_{1,N-1}z^{-d_{1,N-1}}$$

For every two coefficients added to the partial response sequences beyond $h_{0,0}$ or $h_{1,0}$, an additional c_1+c_2 z-plane zeroes are added to $C_0(z)$ or $C_1(z)$, respectively, only two of which are controllable. We note that N must be odd if $C_0(z)$ and $C_1(z)$ are to have the same number of zeroes. If N is odd, the $C_i(z)$ are both of order $\frac{1}{2}(N-1)(c_1+c_2)$. If N is even, however, $C_0(z)$ is of order $c_2+((N/2)-1)(c_1+c_2)$ while $C_1(z)$ is of order $c_1+((N/2)-1)(c_1+c_2)$.

The stagger ratio, itself, is an important parameter of a Staggered PRT filter design for two reasons.

- 1) The stagger ratio determines the number of uncontrollable zeroes incurred by partial response sequences for a given value of N .
- 2) For filter designs in which the controllable zeroes are located in the z-plane near $z=1$ (*e.g.* for clutter filters or other high-pass filters with narrow stopbands), the stagger ratio appears to determine the z-plane distribution of the uncontrollable zeroes. These are the zeroes which determine the filter's passband characteristics, such as ripple.

Figures 3.14 through 3.16 provide examples of the effect of stagger ratio choice on the z-plane zero distribution of $|G(\omega)|^2$. The partial response sequences were all designed to place the controllable zeroes of the $C_i(z)$ at $z=1$. Each figure consists of two plots, "a" and "b". The "a" plots are z-plane zero plots of $|G(\omega)|^2$ – the unit circle is displayed on these plots, along with a block of text on the lower left describing the basic filter parameters. The "b" plots are corresponding plots of the magnitude response of $|G(\omega)|^2$, with the same plot format as Figure 3.4. Each "b" plot displays $|G(\omega)|^2$ for an entire Nyquist interval – digital frequencies from 0 to 2π –

although different values of δ_T were employed in generating the plots. $N=3$ for all three figures, implying two controllable zeros and $(c_1+c_2)-2$ uncontrollable zeros for each partial response sequence. For these examples, the $h_{i,k}$ are real.

Figure 3.14 displays $|G(\omega)|^2$ for the case $c_1=2, c_2=3$. With N odd, $C_0(z)$ and $C_1(z)$ possess the same numbers of intersample delays of c_1 and c_2 and hence the same distributions of powers of z in the products $C_0(z)C_0(z^{-1})$ and $C_1(z)C_1(z^{-1})$. Thus, $|G(\omega)|^2$ also possesses this distribution of powers of z , which extends from $z^{-(c_1+c_2)}$ to $z^{c_1+c_2}$. For the particular values of c_1 and c_2 , the distribution extends from z^{-5} to z^5 , therefore $|G(\omega)|^2$ possesses 10 zeroes.

Referring to Figure 3.14a, we see that 4 of these zeroes are located at $z=1$. The controllable zeroes of $C_0(z)$ and $C_1(z)$, which were all placed at $z=1$, carry over to $|G(\omega)|^2$ for the following reason. The $C_i(z)$ are of the form

$$C_i(z) = (z-1)^2 \prod_{m=1}^{d_{i,N-1}-2} (z-z_{i,m}), \quad i = 0,1$$

Thus

$$C_i(z)C_i\left(\frac{1}{z}\right) = (z-1)^2(z^{-1}-1)^2 \prod_{m=1}^{d_{i,N-1}-2} (z-z_{i,m})(z^{-1}-z_{i,m}), \quad i = 0,1$$

and

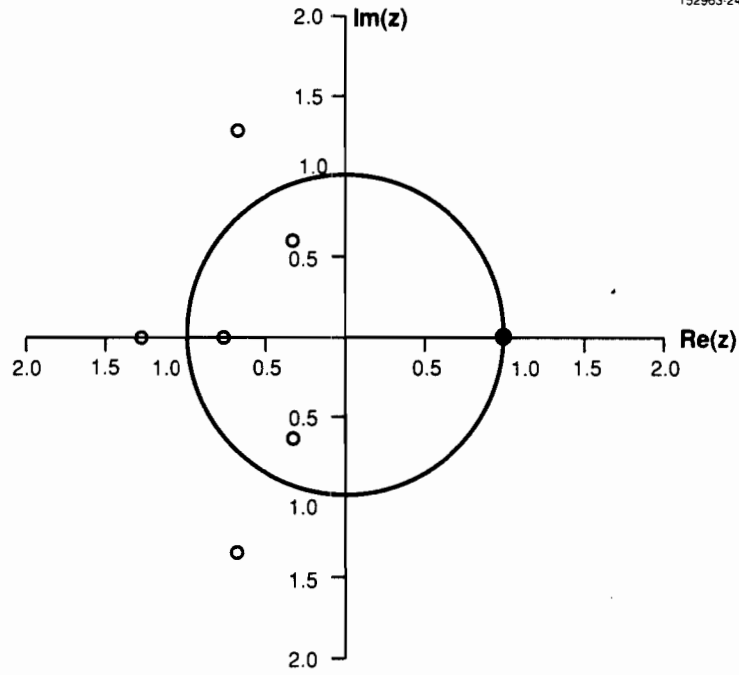
$$\begin{aligned} |G(\omega)|^2 &= \frac{1}{2}C_0(z)C_0\left(\frac{1}{z}\right) + \frac{1}{2}C_1(z)C_1\left(\frac{1}{z}\right) \\ &= \frac{1}{2} \left[(z-1)^2(z^{-1}-1)^2 \sum_{i=1}^2 \left(\prod_{m=1}^{d_{i,N-1}-2} (z-z_{i,m})(z^{-1}-z_{i,m}) \right) \right] \end{aligned}$$

The remaining six zeroes in Figure 3.14a are the uncontrollable zeroes resulting from the $z_{i,m}$ in the preceding equation and give rise to the dips in the curve of Figure 3.14b at 35, 52 and 70 m/s Doppler velocity.

Figure 3.15 displays $|G(\omega)|^2$ for the case $c_1=3, c_2=4$. As in Figure 3.14, $N=3$ and all controllable zeroes of the partial response sequences are placed at $z=1$. In this case, however, $|G(\omega)|^2$ possesses 10 uncontrollable zeroes. This fact is reflected in the increased number of passband ripples in Figure 3.15b relative to Figure 3.14b.

Figure 3.16 displays $|G(\omega)|^2$ for the case $c_1=5, c_2=6$. All other parameters of the filter design are identical to those of the preceding two figures. $|G(\omega)|^2$ possesses 18 uncontrollable zeroes in this case.

Increasing the values of c_1 and c_2 does not necessarily worsen the passband characteristics of a Staggered PRT filter. The effect of the uncontrollable zeroes is a function of both their number *and* their z -plane locations. Certain stagger ratios (δ_T)

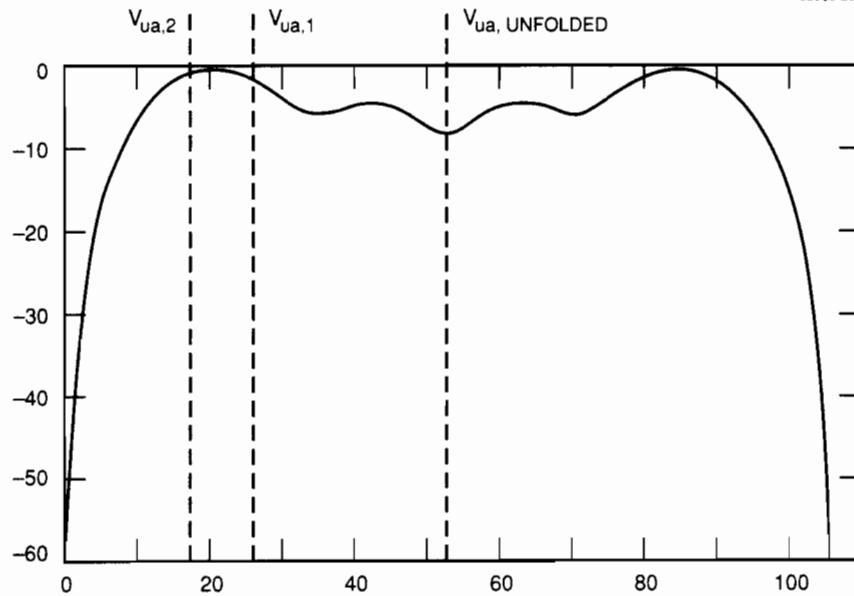


Z-PLANE ZERO PLOT OF $C_0(z)C_0(1/z)+C_1(z)C_1(1/z)$ FOR FILTER 233
 NYQUIST FREQUENCY IS $(2\delta_T)^{-1}$ Hz

STAGGER RATIO 2:3
 3 FILTER COEFFICIENTS

4 ZEROES AT $z = 1$
 MAXIMALLY FLAT DESIGN

Figure 3.14a: Z-Plane zeroes of $|G(\omega)|^2 - c_1=2, c_2=3, N=3$ and all controllable zeroes at $z=1$



(MAGNITUDE)² (dB) vs DOPPLER VELOCITY (m/s)
 FILTER ID: 35

STAGGER RATIO 2:3

δ_T IS 0.47619 ms

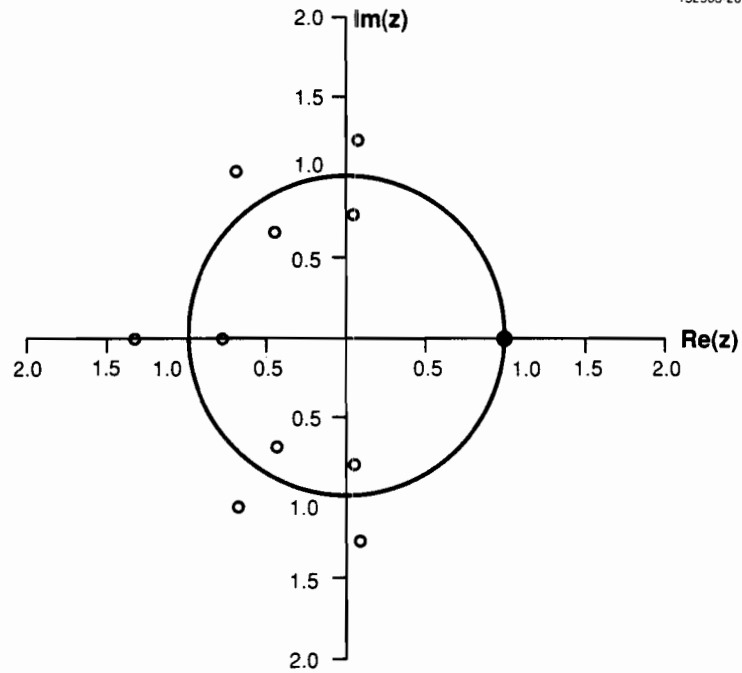
PRF 1 = 1050.0 Hz, PRF 2 = 700.0 Hz

3 FILTER COEFFICIENTS

RADAR FREQUENCY IS 3.00000 GHz

MAXIMALLY FLAT DESIGN

Figure 3.14b: $|G(\omega)|^2 - c_1=2, c_2=3, N=3$ and all controllable zeroes at $z=1$

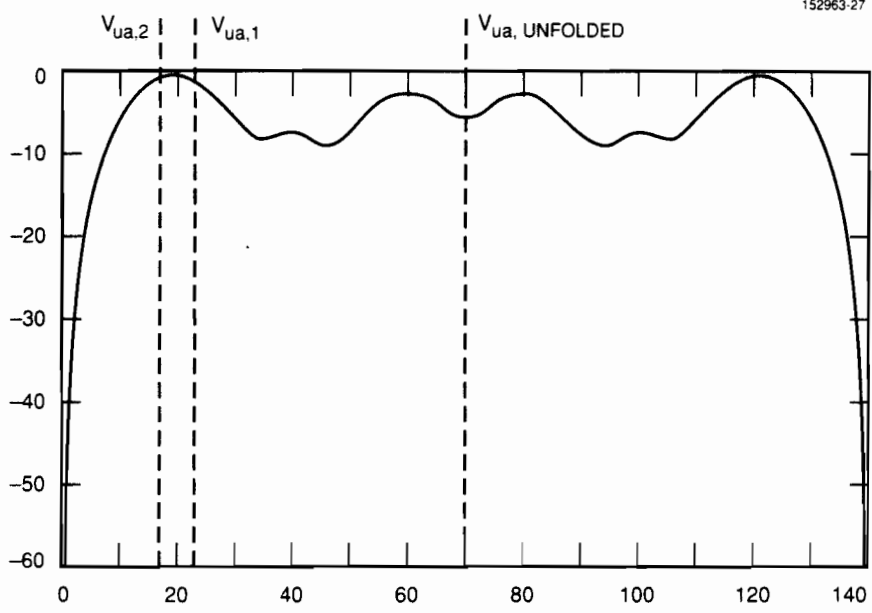


Z-PLANE ZERO PLOT OF $C_0(z)C_0(1/z)+C_1(z)C_1(1/z)$ FOR FILTER 63
 NYQUIST FREQUENCY IS $(2\delta_T)^{-1}\text{Hz}$

STAGGER RATIO 3:4
 3 FILTER COEFFICIENTS

4 ZEROS AT $z=1$
 MAXIMALLY FLAT DESIGN

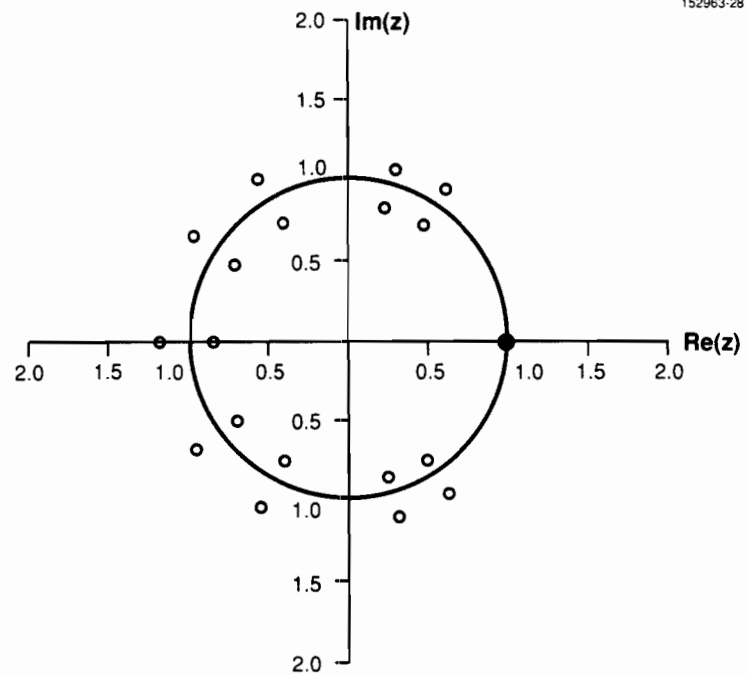
Figure 3.15a: Z-Plane zeroes of $|G(\omega)|^2 - c_1=3, c_2=4, N=3$ and all controllable zeroes at $z=1$



(MAGNITUDE)² (dB) vs DOPPLER VELOCITY (m/s)
 FILTER ID: 37

STAGGER RATIO 3:4	3 FILTER COEFFICIENTS
δ_T IS 0.35714 ms	RADAR FREQUENCY IS 3.00000 GHz
PRF 1 = 933.3 Hz, PRF 2 = 700.0 Hz	MAXIMALLY FLAT DESIGN

Figure 3.15b: $|G(\omega)|^2 - c_1=3, c_2=4, N=3$ and all controllable zeroes at $z=1$



Z-PLANE ZERO PLOT OF $C_0(z)C_0(1/z)+C_1(z)C_1(1/z)$ FOR FILTER 68
 NYQUIST FREQUENCY IS $(2\delta_T)^{-1}$ Hz

STAGGER RATIO 5:6
 3 FILTER COEFFICIENTS

4 ZEROS AT $z=1$
 MAXIMALLY FLAT DESIGN

Figure 3.16a: Z-Plane zeroes of $|G(\omega)|^2 - c_1=5, c_2=6, N=3$ and all controllable zeroes at $z=1$

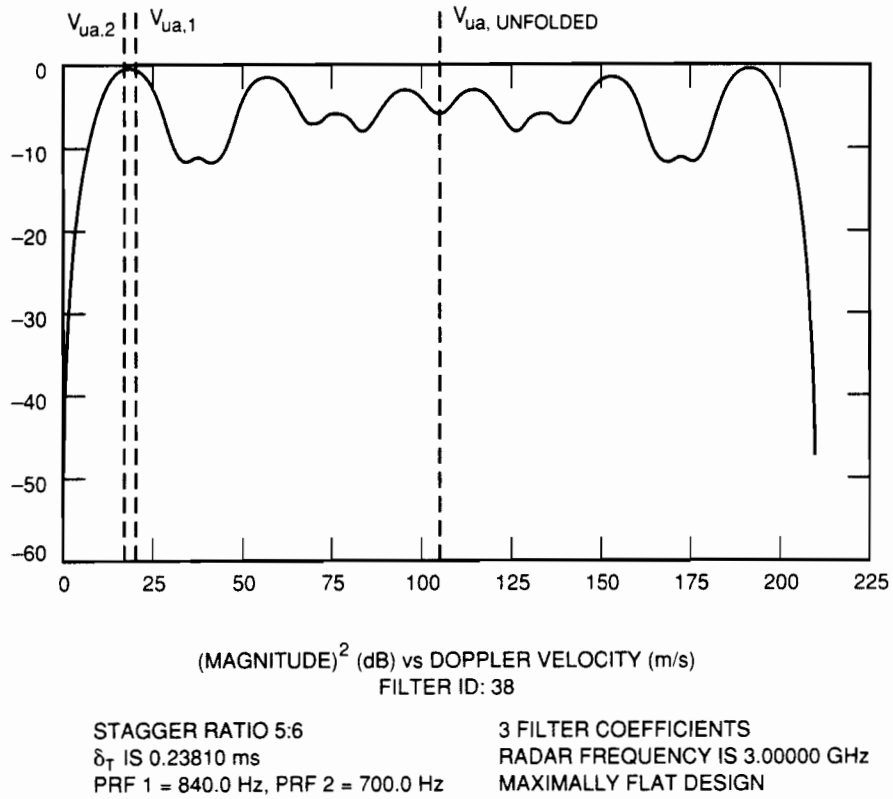
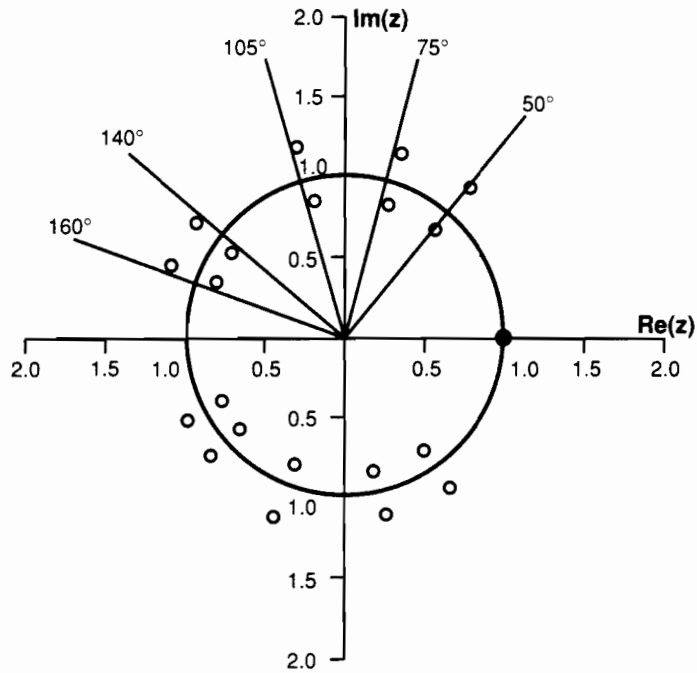


Figure 3.16b: $|G(\omega)|^2 - c_1=5, c_2=6, N=3$ and all controllable zeroes at $z=1$

e.g. 5:7) result in passband characteristic with small ripples and a steep slope in the transition region between the stopband and passband. Placing all controllable zeroes at $z=1$ makes the transition region slope a function of the uncontrollable zeroes, as well.

Empirically, the selection of a stagger ratio appears to determine the z -plane loci for $|G(\omega)|^2$'s uncontrollable zeroes. Within the unit circle in the upper half-plane, the loci appear to be second order functions such as hyperbolas and parabolas. Outside of the unit circle and in the lower half-plane, the loci are determined by the conjugate and reciprocal symmetries discussed earlier. To date, an analytical description of these loci as a function of the stagger ratio has not been obtained. Factoring polynomials is generally difficult.

As an example of such loci, Figures 3.17a through 3.17f display the z -plane positions assumed by uncontrollable zeroes which are successively added to $|G(\omega)|^2$. Figures 3.18a-f are corresponding plots of $|G(\omega)|^2$ versus Doppler velocity. Each design displayed in these figures possesses a 5:7 stagger ratio with all controllable zeroes clustered at $z=1$ - this type of design will be discussed in section 4.2 as the *Maximally Flat Response* design technique. The values of N for Figures 3.17a-f are 3, 4, 5, 6, 7 and 8, respectively; resulting in 4, 6, 8, 10, 12 and 14 controllable zeroes, and 20, 32, 40, 52, 60 and 72 uncontrollable zeroes, respectively. The radials in the upper half-plane of the zero plots are included for the purpose of illustration, only. As N increases, additional uncontrollable zeroes appear on the loci, increasing the depth of the passband ripples of $|G(\omega)|^2$. The ripple locations are essentially fixed. The additional zeroes placed near $z=1$ increase the stopband width with N , and the transition region width (e.g. the velocity interval over which $|G(\omega)|^2$ goes from -60 dB to -3 dB) decreases, at a lesser rate, with N . As the stopband width increases more rapidly than the transition band width decreases, the passband edge also increases with increasing N .

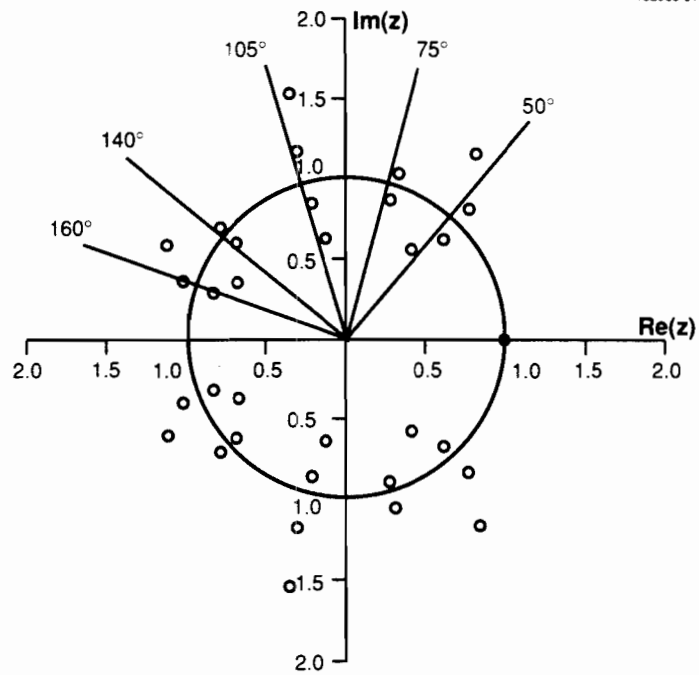


Z-PLANE ZERO PLOT OF $C_0(z)C_0(1/z) + C_1(z)C_1(1/z)$ FOR FILTER 573
 NYQUIST FREQUENCY IS $(2\delta_T)^{-1}$ Hz

STAGGER RATIO 5:7
 3 FILTER COEFFICIENTS

4 ZEROS AT $z = 1$
 MAXIMALLY FLAT DESIGN

Figure 3.17a: Z-Plane zeroes of $|G(\omega)|^2 - c_1=5, c_2=7, N=3$ and all controllable zeroes at $z=1$

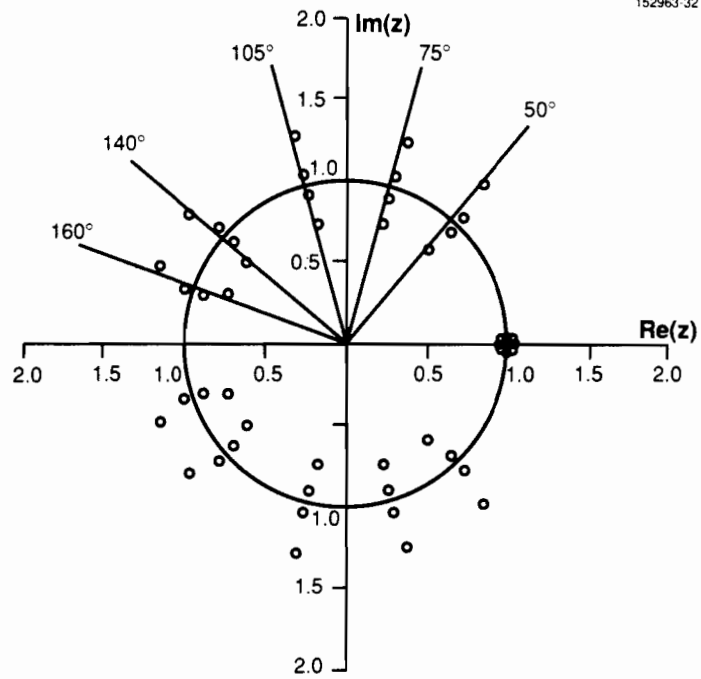


Z-PLANE ZERO PLOT OF $C_0(z)C_0(1/z) + C_1(z)C_1(1/z)$ FOR FILTER 574
 NYQUIST FREQUENCY IS $(2\delta_T)^{-1}$ Hz

STAGGER RATIO 5:7
 4 FILTER COEFFICIENTS

6 ZEROES AT $z = 1$
 MAXIMALLY FLAT DESIGN

Figure 3.17b: Z-Plane zeroes of $|G(\omega)|^2 - c_1=5, c_2=7, N=4$ and all controllable zeroes at $z=1$

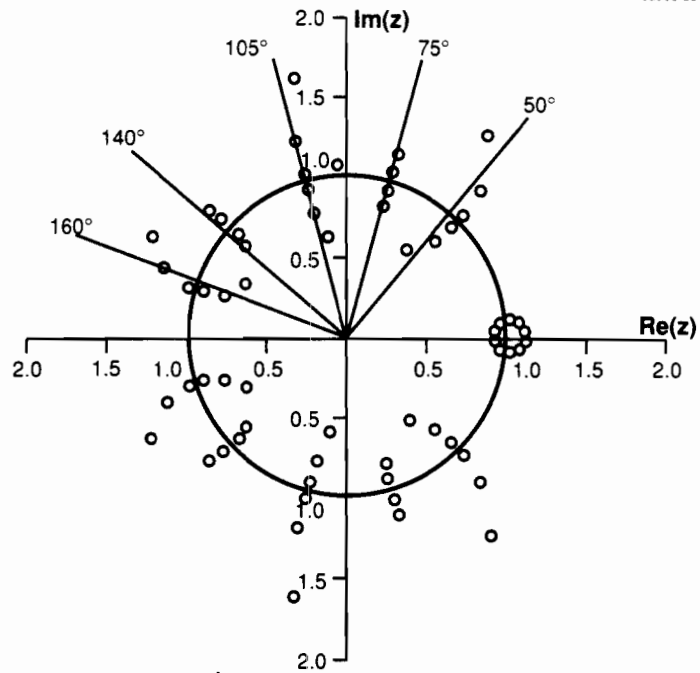


Z-PLANE ZERO PLOT OF $C_0(z)C_0(1/z)+C_1(z)C_1(1/z)$ FOR FILTER 575
 NYQUIST FREQUENCY IS $(2\delta_T)^{-1}$ Hz

STAGGER RATIO 5:7
 5 FILTER COEFFICIENTS

2 ZEROES AT $z = 1$
 MAXIMALLY FLAT DESIGN

Figure 3.17c: Z-Plane zeroes of $|G(\omega)|^2 - c_1=5, c_2=7, N=5$ and all controllable zeroes at $z=1$

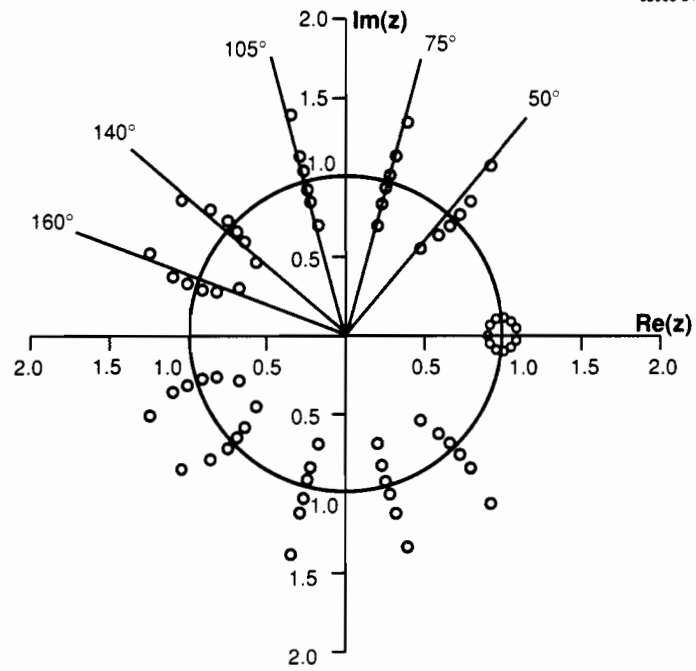


Z-PLANE ZERO PLOT OF $C_0(z)C_0(1/z) + C_1(z)C_1(1/z)$ FOR FILTER 576
 NYQUIST FREQUENCY IS $(2\delta_T)^{-1}$ Hz

STAGGER RATIO 5:7
 6 FILTER COEFFICIENTS

0 ZEROS AT $z = 1$
 MAXIMALLY FLAT DESIGN

Figure 3.17d: Z-Plane zeroes of $|G(\omega)|^2 - c_1=5, c_2=7, N=6$ and all controllable zeroes at $z=1$

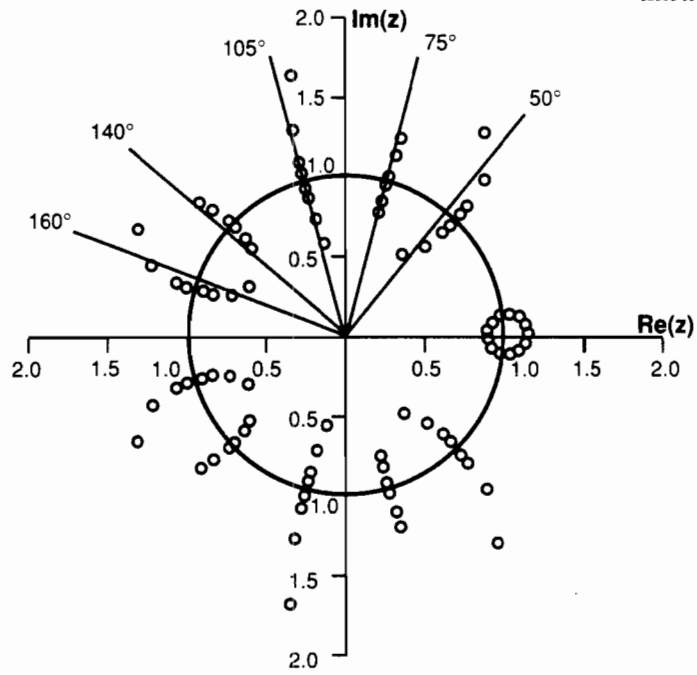


Z-PLANE ZERO PLOT OF $C_0(z)C_0(1/z) + C_1(z)C_1(1/z)$ FOR FILTER 577
 NYQUIST FREQUENCY IS $(2\delta_T)^{-1}\text{Hz}$

STAGGER RATIO 5:7
 7 FILTER COEFFICIENTS

0 ZEROES AT $z = 1$
 MAXIMALLY FLAT DESIGN

Figure 3.17e: Z-Plane zeroes of $|G(\omega)|^2 - c_1=5, c_2=7, N=7$ and all controllable zeroes at $z=1$

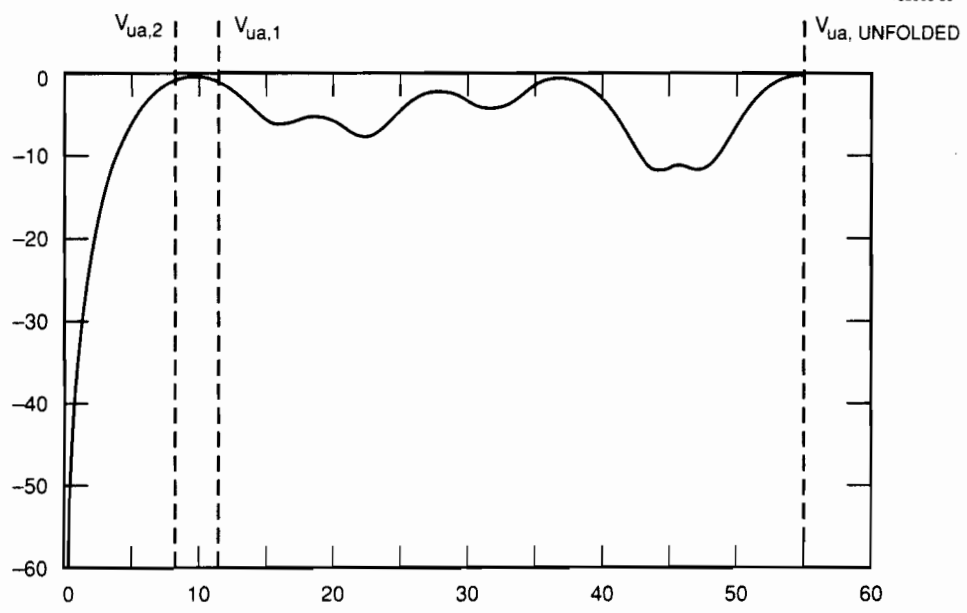


Z-PLANE ZERO PLOT OF $C_0(z)C_0(1/z)+C_1(z)C_1(1/z)$ FOR FILTER 578
 NYQUIST FREQUENCY IS $(2\delta_T)^{-1}$ Hz

STAGGER RATIO 5:7
 8 FILTER COEFFICIENTS

0 ZEROS AT $z = 1$
 MAXIMALLY FLAT DESIGN

Figure 3.17f: Z-Plane zeroes of $|G(\omega)|^2 - c_1=5, c_2=7, N=8$ and all controllable zeroes at $z=1$



(MAGNITUDE)² (dB) vs DOPPLER VELOCITY (m/s)
FILTER ID: 573

STAGGER RATIO 5:7	3 FILTER COEFFICIENTS
δ_T IS 0.45455 ms	RADAR FREQUENCY IS 3.00000 GHz
PRF 1 = 440.0 Hz, PRF 2 = 314.3 Hz	MAXIMALLY FLAT DESIGN

Figure 3.18a: $|G(\omega)|^2$ versus Doppler velocity - $c_1=5$, $c_2=7$, $N=3$ and all controllable zeroes at $z=1$

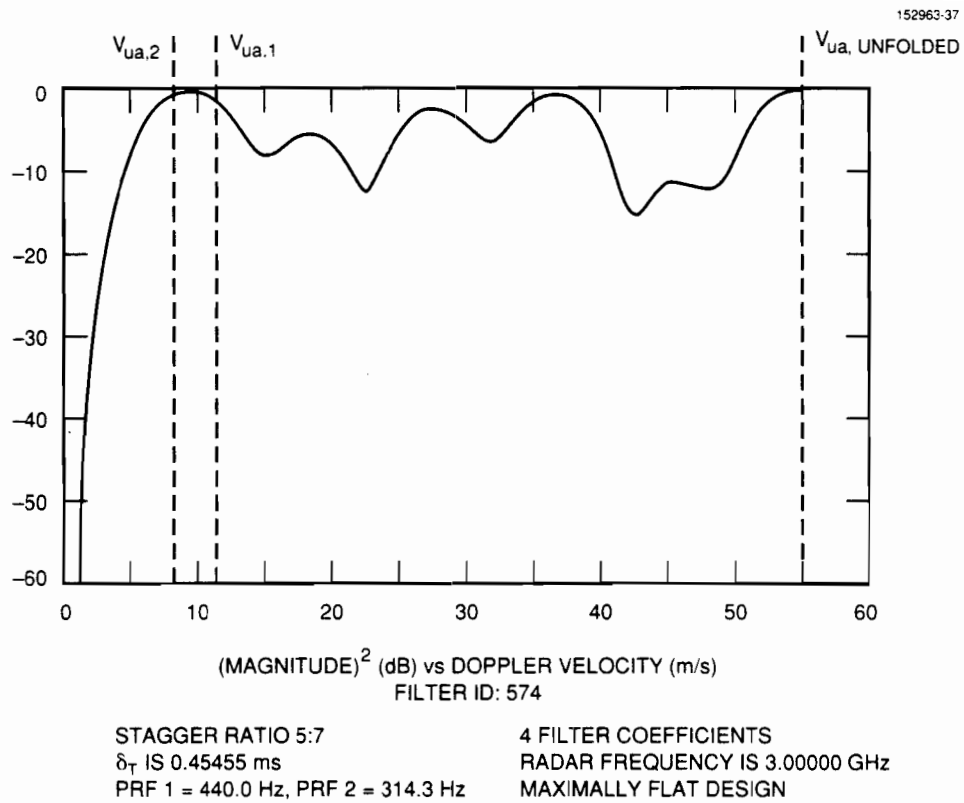
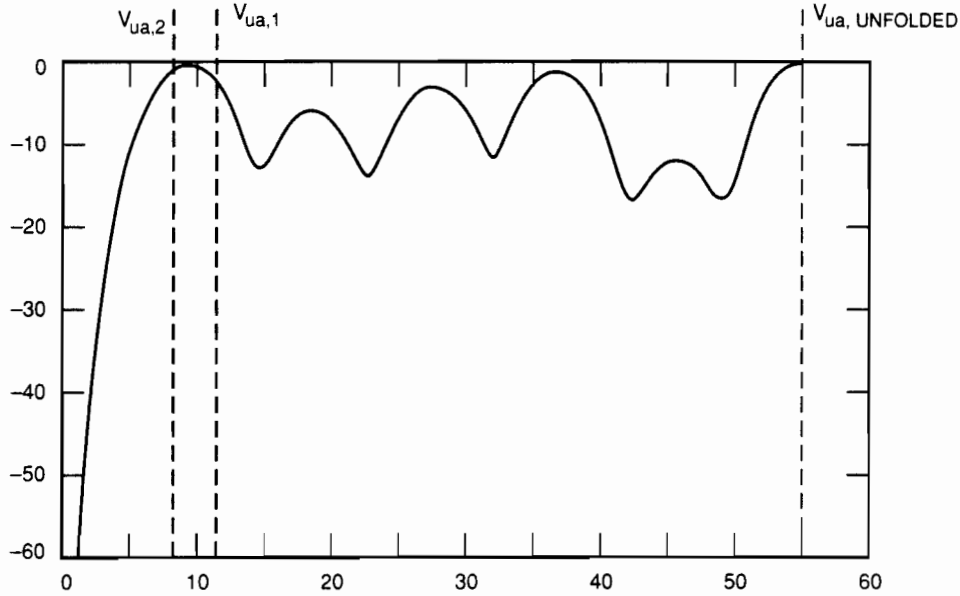


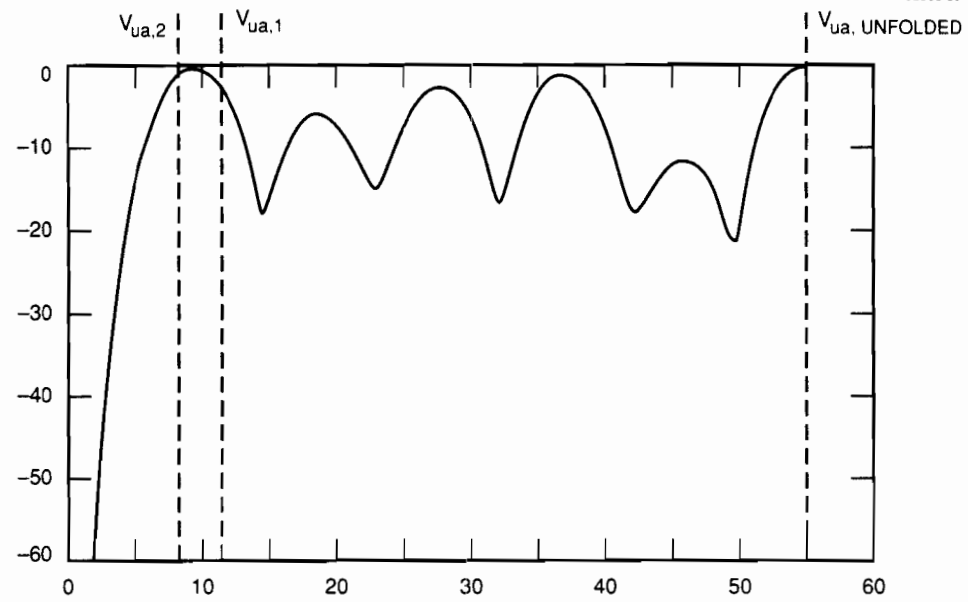
Figure 3.18b: $|G(\omega)|^2$ versus Doppler velocity - $c_1=5$, $c_2=7$, $N=4$ and all controllable zeroes at $z=1$



(MAGNITUDE)² (dB) vs DOPPLER VELOCITY (m/s)
 FILTER ID: 575

STAGGER RATIO 5:7	5 FILTER COEFFICIENTS
δ_T IS 0.45455 ms	RADAR FREQUENCY IS 3.00000 GHz
PRF 1 = 440.0 Hz, PRF 2 = 314.3 Hz	MAXIMALLY FLAT DESIGN

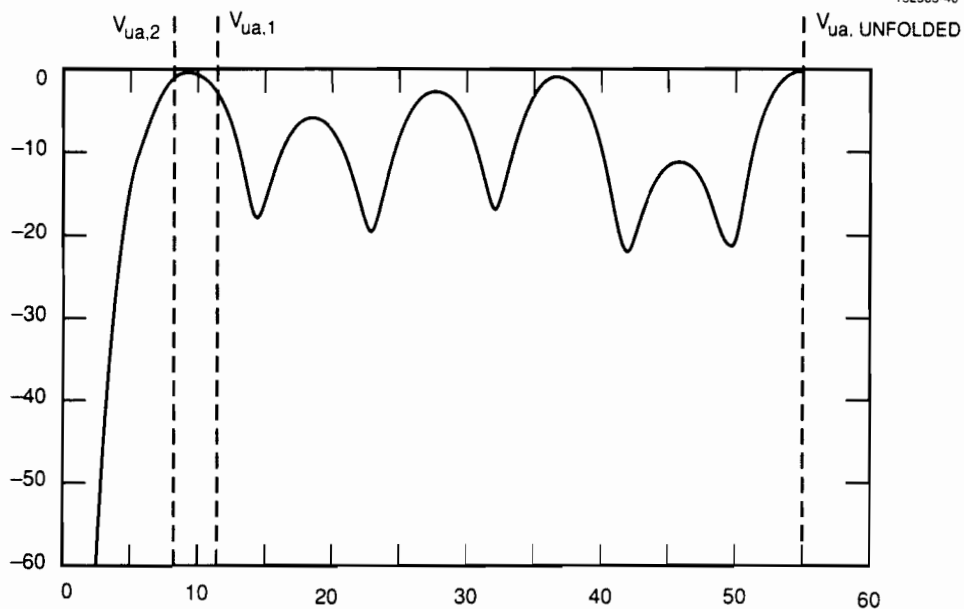
Figure 3.18c: $|G(\omega)|^2$ versus Doppler velocity - $c_1=5$, $c_2=7$, $N=5$ and all controllable zeroes at $z=1$



(MAGNITUDE)² (dB) vs DOPPLER VELOCITY (m/s)
FILTER ID: 576

STAGGER RATIO 5:7	6 FILTER COEFFICIENTS
δ_T IS 0.45455 ms	RADAR FREQUENCY IS 3.00000 GHz
PRF 1 = 440.0 Hz, PRF 2 = 314.3 Hz	MAXIMALLY FLAT DESIGN

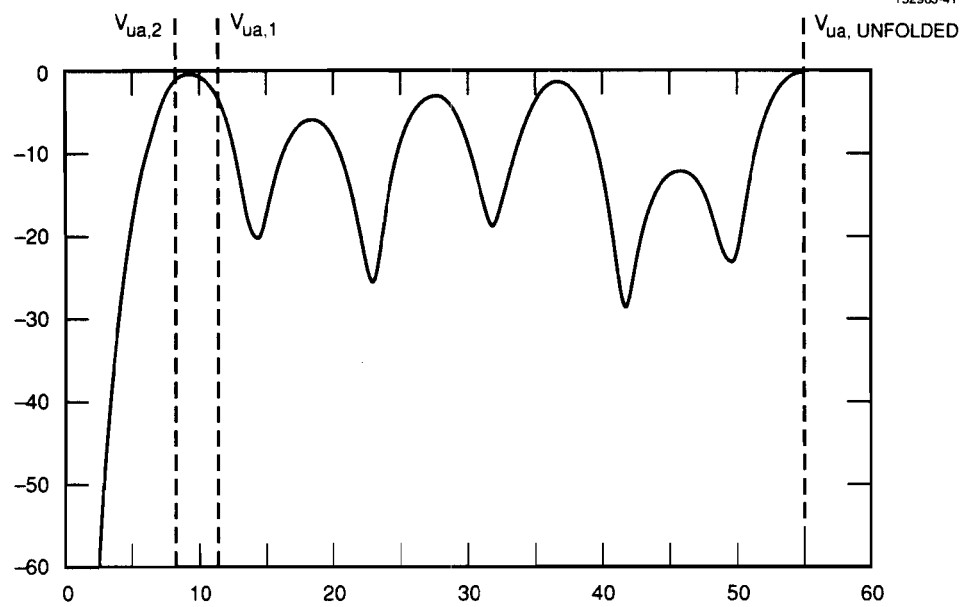
Figure 3.18d: $|G(\omega)|^2$ versus Doppler velocity - $c_1=5$, $c_2=7$, $N=6$ and all controllable zeroes at $z=1$



(MAGNITUDE)² (dB) vs DOPPLER VELOCITY (m/s)
 FILTER ID: 577

STAGGER RATIO 5:7	7 FILTER COEFFICIENTS
δ_T IS 0.45455 ms	RADAR FREQUENCY IS 3.00000 GHz
PRF 1 = 440.0 Hz, PRF 2 = 314.3 Hz	MAXIMALLY FLAT DESIGN

Figure 3.18e: $|G(\omega)|^2$ versus Doppler velocity - $c_1=5$, $c_2=7$, $N=7$ and all controllable zeroes at $z = 1$



(MAGNITUDE)² (dB) vs DOPPLER VELOCITY (m/s)
 FILTER ID: 578

STAGGER RATIO 5:7

δ_T IS 0.45455 ms

PRF 1 = 440.0 Hz, PRF 2 = 314.3 Hz

8 FILTER COEFFICIENTS

RADAR FREQUENCY IS 3.00000 GHz

MAXIMALLY FLAT DESIGN

Figure 3.18f: $|G(\omega)|^2$ versus Doppler velocity - $c_1=5$, $c_2=7$, $N=8$ and all controllable zeroes at $z=1$

4.0 STAGGERED PRT FILTER DESIGN TECHNIQUES

The current section of this report will describe several techniques for determining the staggered PRT filter's partial response sequences. Although, the techniques will be discussed in the context of clutter filter design, the *Coefficient Selection* and *OSCRM* techniques have general applicability.

4.1 DESIGN TECHNIQUE: COEFFICIENT SELECTION

A wide variety of tools exist for the design of FIR filters which operate on equispaced data, most notably the Parks-McClellan algorithm which was developed in the early 1970's [Parks72a]. The *Coefficient Selection* technique allows these equispaced FIR design tools to be employed in the design of Staggered PRT filters. Coefficient Selection operates as follows.

- 1) Values are selected for δ_T , c_1 and c_2 , and for the Staggered PRT filter length, N .
- 2) Equispaced FIR filter(s) are designed with the desired response for an intersample delay (PRT) of δ_T . If N is odd, a single FIR design with $d_{i,N-1}+1$ coefficients (i.e. an impulse response duration of $d_{i,N-1}\delta_T$ seconds) is required. If N is even, matched FIR designs with $d_{0,N-1}+1$ and $d_{1,N-1}+1$ coefficients (impulse response durations of $d_{0,N-1}\delta_T$ and $d_{1,N-1}\delta_T$ seconds, respectively) are required.
- 3) The Staggered PRT filter's partial response sequences are determined by time-aligning those sequences with the FIR design(s) and selecting coefficients from the FIR design(s) at the matching sampling instants. Denoting the FIR design for the case where N is odd as $\{f_l\}_{l=0}^{d_{i,N-1}}$, we have

$$h_{0,0} = f_0, h_{0,1} = f_{d_{0,1}}, \dots, h_{0,N-1} = f_{d_{0,N-1}}$$

$$h_{1,0} = f_0, h_{1,1} = f_{d_{1,1}}, \dots, h_{1,N-1} = f_{d_{1,N-1}}$$

In the case that N is even, and denoting the FIR designs with impulse response durations of $d_{0,N-1}\delta_T$ and $d_{1,N-1}\delta_T$ as $\{f_l^0\}_{l=0}^{d_{0,N-1}}$ and $\{f_l^1\}_{l=0}^{d_{1,N-1}}$, respectively, we have

$$h_{0,0} = f_0^0, h_{0,1} = f_{d_{0,1}}^0, \dots, h_{0,N-1} = f_{d_{0,N-1}}^0$$

$$h_{1,0} = f_0^1, h_{1,1} = f_{d_{1,1}}^1, \dots, h_{1,N-1} = f_{d_{1,N-1}}^1$$

Given c_1 , c_2 , N and δ_T , the staggered PRT partial response sequence generated from an equispaced FIR design by Coefficient Selection possesses the Discrete Fourier Transform (DFT) which most closely approximates that of the equispaced

FIR design in the sense of the l_2 norm. More concisely, the DFT is an isometric mapping from $l_2[0, M-1]$ onto itself.

$l_2[0, M-1]$ is the Hilbert Space of complex-valued sequences $r = \{r_l\}_{l=0}^{M-1}$. For any two elements of $l_2[0, M-1]$, r^1 and r^2 , the $l_2[0, M-1]$ inner product and norm are defined as

$$(r^1 | r^2) \triangleq \sum_{l=0}^{M-1} r_l^1 r_l^{2*}$$

$$\|r^1\| \triangleq \sqrt{(r^1 | r^1)}$$

respectively. It is clear that the DFT maps $l_2[0, M-1]$ to itself.

Define the DFT and Inverse DFT (IDFT), respectively, for $l_2[0, M-1]$ as

$$DFT \{r_l\} \triangleq \{R_k\} = \left\{ \frac{1}{\sqrt{M}} \sum_{l=0}^{M-1} r_l e^{-j2\pi kl/M} \right\}$$

$$IDFT \{R_k\} \triangleq \{r_l\} = \left\{ \frac{1}{\sqrt{M}} \sum_{k=0}^{M-1} R_k e^{j2\pi kl/M} \right\}$$

To establish that the DFT is an isometric mapping of $l_2[0, M-1]$ to itself, we must show that $\|r^1 - r^2\| = \|R^1 - R^2\|$ for all $r^1, r^2 \in l_2[0, M-1]$. Now,

$$\begin{aligned} \|R^1 - R^2\|^2 &= \sum_{k=0}^{M-1} \left| \frac{1}{\sqrt{M}} \sum_{l=0}^{M-1} r_l^1 e^{j2\pi kl/M} - \frac{1}{\sqrt{M}} \sum_{l=0}^{M-1} r_l^2 e^{j2\pi kl/M} \right|^2 \\ &= \sum_{k=0}^{M-1} \frac{1}{M} \left| \sum_{l=0}^{M-1} \rho_l e^{j2\pi kl/M} \right|^2, \quad \rho_l = r_l^1 - r_l^2 \\ &= \frac{1}{M} \sum_{k=0}^{M-1} \left[\sum_{l=0}^{M-1} |\rho_l|^2 + \sum_{\substack{l=0 \\ m \neq l}}^{M-1} \sum_{\substack{m=0 \\ m \neq l}}^{M-1} \rho_l \rho_m^* e^{j2\pi k(l-m)/M} \right] \\ &= \|r^1 - r^2\|^2 + \frac{1}{M} \sum_{\substack{l=0 \\ m \neq l}}^{M-1} \sum_{\substack{m=0 \\ m \neq l}}^{M-1} \left[\rho_l \rho_m^* \sum_{k=0}^{M-1} e^{j2\pi k(l-m)/M} \right] \end{aligned}$$

but,

$$\sum_{k=0}^{M-1} e^{j2\pi k(l-m)/M} = \frac{1 - (e^{j2\pi k(l-m)/M})^M}{1 - e^{j2\pi k(l-m)/M}} = 0, \quad m \neq l$$

Therefore,

$$\|R^1 - R^2\|^2 = \|r^1 - r^2\|^2 \quad (4.1)$$

Since r^1 and r^2 were arbitrary elements of $l_2[0, M-1]$, DFT: $l_2[0, M-1] \rightarrow l_2[0, M-1]$ is proven to be an isometry. This is a slightly modified

statement of Parseval's Theorem.

For a given stagger ratio and Staggered PRT filter length, equation 4.1 guarantees that each of the partial response sequences generated by the Coefficient Selection technique most closely approximate the transfer function(s) of the corresponding equispaced FIR design(s) *at the frequency-domain sampling points of the DFT*, in the sense of the $l_2[0, M-1]$ norm. Equation 4.1 does not, however, provide an indication of the Staggered PRT filter's characteristics at digital frequencies other than $\{2\pi k / M\}_{k=0}^{M-1}$, nor does it provide guidance in the choice of stagger ratio.

The desired frequency characteristic of clutter filters for weather radar applications is that of a high-pass filter with a narrow stopband, relative to the Nyquist interval, and a short transition region between the stopband and passband. Equispaced FIR filters, with some odd number M of coefficients, designed for these applications typically possess impulse responses such as the one depicted in Figure 4.1, in which

$$f_l = \begin{cases} \frac{-\alpha}{M-1}, & l = 0, \dots, M-1, \quad l \neq \frac{M-1}{2} \\ \alpha, & l = \frac{M-1}{2} \\ 0, & \text{otherwise} \end{cases}$$

where α is a multiplicative constant. When an equispaced FIR filter of this sort is employed for a Coefficient Selection design of a Staggered PRT filter, some guidance in the selection of a stagger ratio is provided by the fact that the zeroes of a complex polynomial are a continuous function of the polynomial's coefficients [Marden49a].

Consider two equispaced impulse response sequences of length M , $\{f_l\}_{l=0}^{M-1}$ and $\{g_l\}_{l=0}^{M-1}$, and define their Z-transforms to be $F(z)$ and $G(z)$, respectively. Let

$$\epsilon_l \triangleq g_l - f_l, \quad l = 0, \dots, M-1$$

Then the magnitude of the difference in their Z-transforms may be bounded as follows

$$|F(z) - G(z)| = \left| \sum_{l=0}^{M-1} \epsilon_l z^{-l} \right| \leq \sum_{l=0}^{M-1} |\epsilon_l z^{-l}| \leq \epsilon_{\max} \sum_{l=0}^{M-1} |z^{-l}|$$

where $\epsilon_{\max} \triangleq \max_l \{|\epsilon_l|\}$. If we evaluate the Z-transforms on the unit circle, $z = e^{j\omega}$, we obtain the following upper bound.

$$|F(\omega) - G(\omega)| \leq M \epsilon_{\max} \quad (4.2)$$

Once a value for N has been selected, equation 4.2 provides the following guidance for choosing a stagger ratio. The stagger ratio should be selected so that the

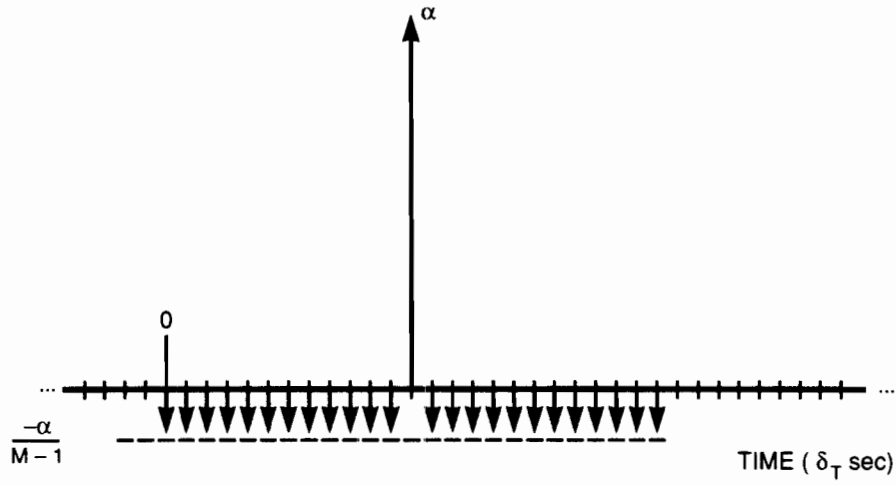


Figure 4.1: Equispaced FIR clutter filter impulse response, M odd

coefficient of maximum modulus in the equispaced design is incorporated in both of the partial response sequences. In particular, for the equispaced designs described in the preceding paragraph, the central coefficient in the impulse response should be incorporated in both of the partial response sequences.

Figures 4.2 through 4.4 provide a graphical display of equation 4.2 in the case of a Coefficient Selection design. Each figure consists of two plots "a" and "b". The "a" plots are z-plane zero plots of $|G(\omega)|^2$ for the various designs; the "b" plots are the corresponding frequency domain plots as a function of digital frequency. As the $|G(\omega)|^2$ are even functions of frequency, each "b" plot displays only the positive portion of the Nyquist interval $\omega \in [0, \pi]$.

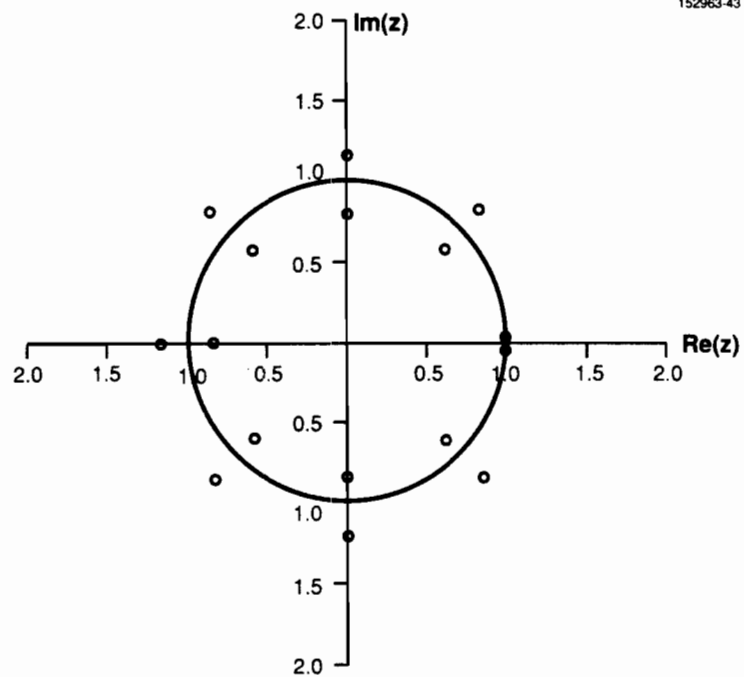
Figure 4.2 displays the equispaced FIR design employed, which possesses 17 filter coefficients. The filter was designed with the Parks-McClellan algorithm – the parameters provided to that algorithm appear on the bottom left-hand side of the plots. Each zero plotted in Figure 4.2a is actually a pair of zeroes. The effect of the zero pairs near $z = 1$ is clearly evident in Figure 4.2b; they generate the sharp notch at 0.03 radians per sample interval. The impulse response of this filter is similar to that shown in Figure 4.1.

Figure 4.3 displays $|G(\omega)|^2$ for the corresponding Staggered PRT design with $c_1=3$, $c_2=5$ and $N=5$. With this choice of Staggered PRT parameters, both partial response sequences incorporate the central FIR coefficient (as $h_{0,2}$ and $h_{1,2}$). Comparing Figures 4.2a and 4.3a, we see zero pairs for the FIR design beginning to diverge in the Staggered PRT design. The divergence is relatively benign for all the zero pairs except for the two pairs near $z = 1$. The corresponding effect in Figure 4.3b is that the passband characteristic of the Staggered PRT filter is close to that of the equispaced filter, while the depth of the stopband has been considerably reduced.

Figure 4.4 displays $|G(\omega)|^2$ for the corresponding Staggered PRT design with $c_1=2$, $c_2=4$ and $N=6$ (note that c_1 and c_2 are not relatively prime – this is reflected in the fact that Figure 4.4b displays a period of π for $|G(\omega)|^2$, indicating that this design is equivalent to a 1:2 stagger with a base sampling rate of $2\delta_T$). In this case, neither of the partial response sequences incorporates the central FIR coefficient. The divergence of the zeroes in Figure 4.4a relative to the equispaced design is so severe that the zero distribution has almost become angularly uniform. Figure 4.4b depicts a filter which possesses an allpass characteristic.

Unfortunately, the Z-Transforms of partial response sequences generated by the Coefficient Selection technique possess a local maximum for their error relative to the corresponding equispaced design in the frequency domain, at $\omega=0$ – the center of the desired stopband for clutter filters. This was evident in Figure 4.3.

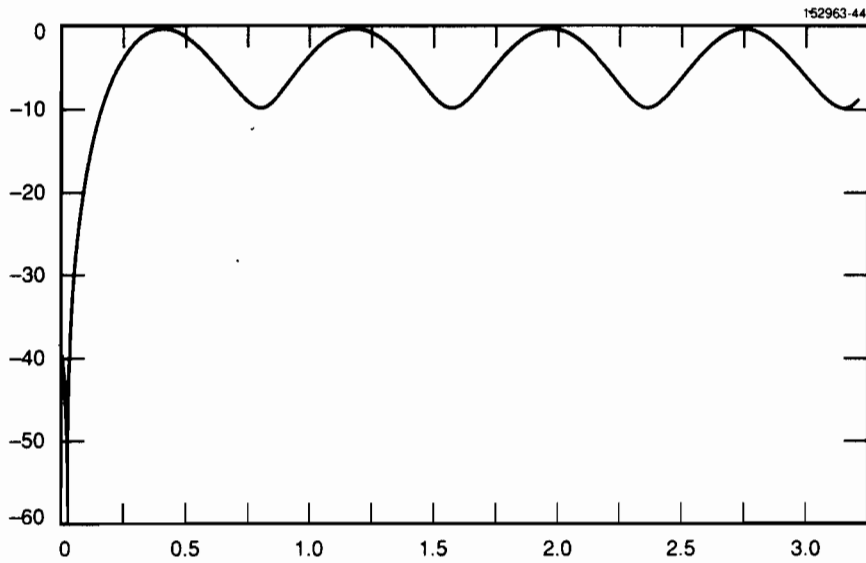
To see why this is so, let f_l and g_l be as before, and denote their Z-Transforms, evaluated on the unit circle $z = e^{j\omega}$, by $F(\omega)$ and $G(\omega)$. We impose the



Z-PLANE ZERO PLOT OF $C_0(z)C_0(1/z)+C_1(z)C_1(1/z)$ FOR FILTER 1117
 NYQUIST FREQUENCY IS $(2\delta_T)^{-1}$ Hz

STAGGER RATIO 1:1	M.M.S.E. DESIGN FROM FIR:
17 FILTER COEFFICIENTS	NFILT - 17 NBANDS - 2
4 ZEROS AT $z = 1$	EDGE: 0.00000 0.00909 0.02727 0.50000
$\delta_T = 1000.00000$ ms	WEIGHTS: 10.00 1.00

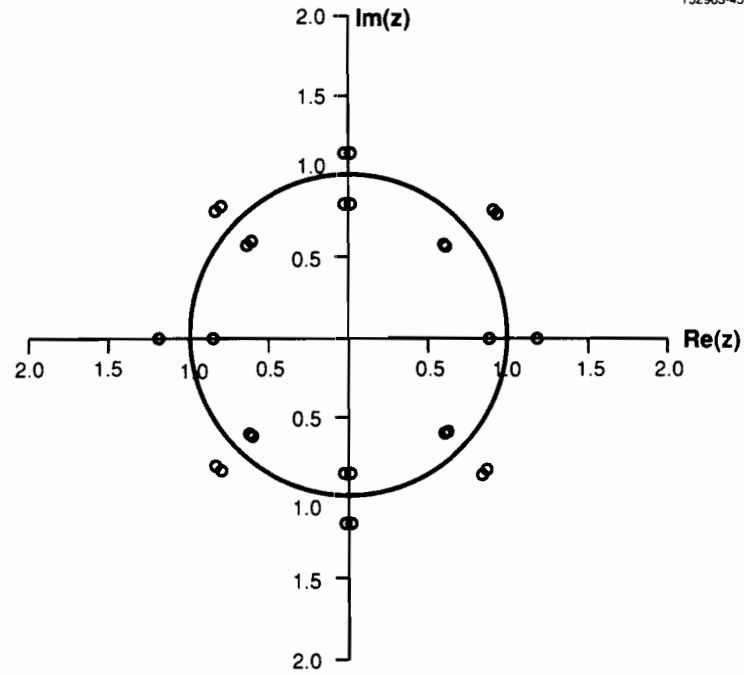
Figure 4.2a: Z-Plane zeroes of squared-magnitude response for 17 point equispaced FIR filter



(MAGNITUDE)² (dB) vs DIGITAL FREQUENCY (Radians Per Sample)
 FILTER ID: 1117

STAGGER RATIO 1:1	M.M.S.E. DESIGN FROM FIR:
δ_T IS 10000.00000 ms	NFILT = 17 NBANDS = 2
PRF 1 = 1.0 Hz, PRF 2 = 1.0 Hz	EDGES:
17 FILTER COEFFICIENTS	0.00000 0.00909 0.02727 0.50000
	WEIGHTS:
	10.0 1.00

Figure 4.2b: Squared-Magnitude response for 17 point equispaced FIR filter

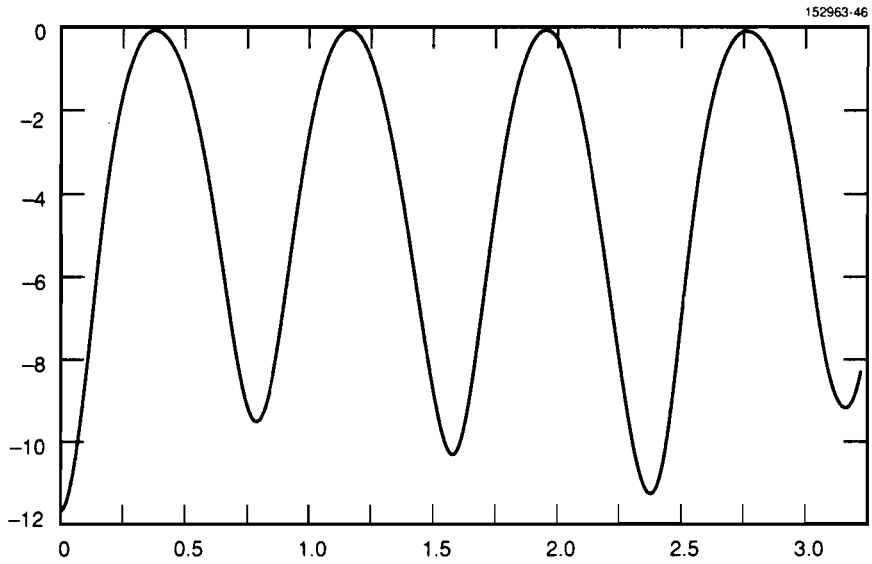


Z-PLANE ZERO PLOT OF $C_0(z)C_0(1/z)+C_1(z)C_1(1/z)$ FOR FILTER 355
 NYQUIST FREQUENCY IS $(2\delta_T)^{-1}$ Hz

STAGGER RATIO 3:5
 5 FILTER COEFFICIENTS
 0 ZEROS AT $z = 1$
 $\delta_T = 1000.00000$ ms

M.M.S.E. DESIGN FROM FIR:
 NFILT - 17 NBANDS - 2
 EDGE: 0.00000 0.00909 0.02727 0.50000
 WEIGHTS: 10.00 1.00

Figure 4.3a: Z-Plane zeroes of $|G(\omega)|^2$ for coefficient selection design -
 $c_1=3$, $c_2=5$ and $N=5$

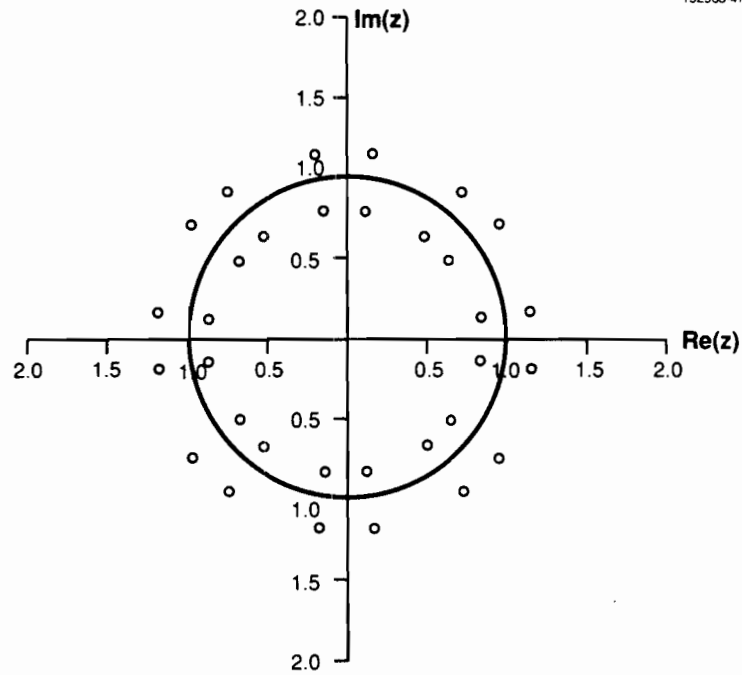


(MAGNITUDE)² (dB) vs DIGITAL FREQUENCY (Radians Per Sample)
 FILTER ID: 355

STAGGER RATIO 3:5
 δ_T IS 10000.00000 ms
 PRF 1 = 0.3 Hz, PRF 2 = 0.2 Hz
 5 FILTER COEFFICIENTS

M.M.S.E. DESIGN FROM FIR:
 NFILT = 17 NBANDS = 2
 EDGES:
 0.00000 0.00909 0.02727 0.50000
 WEIGHTS:
 10.0 1.00

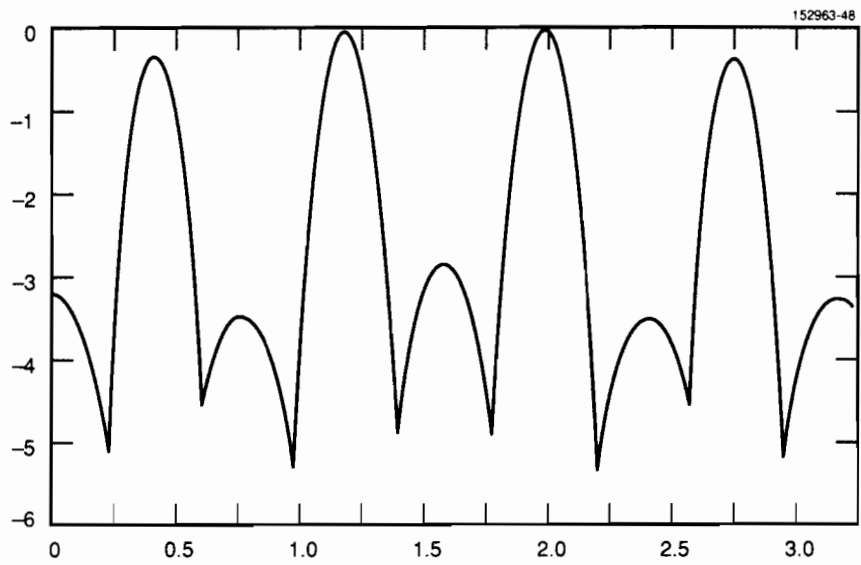
Figure 4.3b: $|G(\omega)|^2$ for coefficient selection design - $c_1=3$, $c_2=5$ and $N=5$



Z-PLANE ZERO PLOT OF $C_0(z)C_0(1/z)+C_1(z)C_1(1/z)$ FOR FILTER 246
 NYQUIST FREQUENCY IS $(2\delta_T)^{-1}$ Hz

STAGGER RATIO 2:4	M.M.S.E. DESIGN FROM FIR:
6 FILTER COEFFICIENTS	NFILT - 17 NBANDS - 2
0 ZEROES AT $z = 1$	EDGE: 0.00000 0.00909 0.02727 0.50000
$\delta_T = 1000.00000$ ms	WEIGHTS: 10.00 1.00

Figure 4.4a: Z-Plane zeroes of $|G(\omega)|^2$ for coefficient selection design -
 $c_1=2$, $c_2=4$ and $N=6$



(MAGNITUDE)² (dB) vs DIGITAL FREQUENCY (Radians Per Sample)
 FILTER ID: 246

STAGGER RATIO 2:4
 δ_T IS 10000.00000 ms
 PRF 1 = 0.5 Hz, PRF 2 = 0.3 Hz
 6 FILTER COEFFICIENTS

M.M.S.E. DESIGN FROM FIR:
 NFILT = 17 NBANDS = 2
 EDGES:
 0.00000 0.00909 0.02727 0.50000
 WEIGHTS:
 10.0 1.00

Figure 4.4b: $|G(\omega)|^2$ for coefficient selection design - $c_1=2$, $c_2=4$ and $N=6$

additional requirement that the f_l and g_l are real for all values of l . Define $D(\omega) \triangleq |F(\omega) - G(\omega)|^2$. $D(\omega)$ is then a real-valued, even, function of ω and necessarily possesses a local extremum at $\omega = 0$. When the equispaced filter is of the type depicted in Figure 4.1, $D(\omega)$ can be differentiated twice to show that this extremum is a local maximum.

Thus, we have the result that an application of the Coefficient Selection technique, in which the equispaced FIR coefficients *not* selected are all of the same sign, will lead to local maxima in the errors of the Z-transforms of the partial response sequences, relative to the equispaced design, at $\omega = 0$. This limits the applicability of the Coefficient Selection technique in designing Staggered PRT clutter filters.

4.2 DESIGN TECHNIQUE: MAXIMALLY FLAT RESPONSE

The Maximally Flat Response (MFR) design technique assigns all controllable zeroes of the Staggered PRT partial response sequences to $z=1$, resulting in a high-pass design with a deep notch at $\omega=0$. This technique is discussed in some detail by Thomas and Lutte [Thomas74a].

The average power transfer function $|G(\omega)|^2$ of a Staggered PRT filter of length N possesses $2(N-1)$ controllable zeroes. If all these zeroes are to be placed at $z=1$, then all the controllable zeroes of the partial response sequences must also be placed at $z=1$. The MFR technique achieves this distribution for the partial response sequences in a manner analogous to a Butterworth filter design.

MFR coefficients are independently generated for the two partial response sequences by setting $C_i(z)$ and its first $N-2$ derivatives to zero at $z=1$ for $i=0,1$; and then solving the resulting system of linear equations for $h_{i,1}, \dots, h_{i,N-1}$. Since the effect of $h_{i,0}$ in the $C_i(z)$ is that of a multiplicative constant (*i.e.* it does not effect the zero locations of $C_i(z)$), it may be chosen arbitrarily. We will select $h_{i,0}=1$, $i=0,1$. This results in the two systems of equations

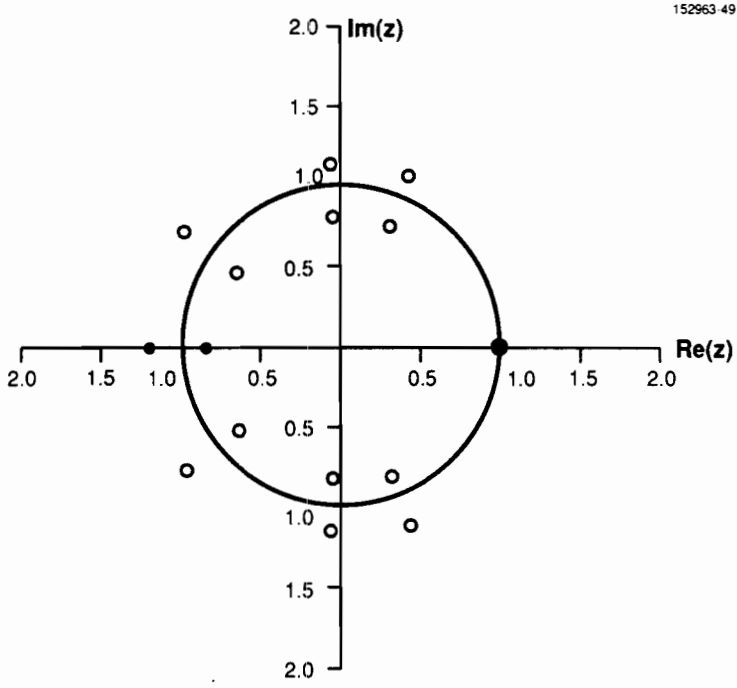
$$\begin{bmatrix} 1 & 1 & \dots & 1 \\ \beta_{i,1,1} & \beta_{i,1,2} & \dots & \beta_{i,1,N-1} \\ \cdot & \cdot & \cdot & \cdot \\ \cdot & \cdot & \cdot & \cdot \\ \beta_{i,N-2,1} & \beta_{i,N-2,2} & \dots & \beta_{i,N-2,N-1} \end{bmatrix} \begin{bmatrix} h_{i,1} \\ h_{i,2} \\ \cdot \\ \cdot \\ h_{i,N-1} \end{bmatrix} = \begin{bmatrix} -1 \\ 0 \\ \cdot \\ \cdot \\ 0 \end{bmatrix}, \quad i=0,1 \quad (4.3a)$$

where

$$\beta_{i,l,m} \triangleq \frac{d^l}{dz^l} \left(z^{-d_{i,m}} \right) \Big|_{z=1} \quad (4.3b)$$

Note that the factorial growth in $|\beta_{i,l,m}|$ with the row index, l , may cause the coefficient matrix in 4.3a to become ill-conditioned. This ill-conditioning is evident in the designs of Figures 3.11 where the controllable zeroes are clustered about, rather than collocated at, $z=1$ for $N>3$.

As MFR places all controllable zeroes of $|G(\omega)|^2$ for a Staggered PRT filter at $z=1$, the passband characteristics of such filters are wholly determined by the stagger ratio and filter length. Figure 4.5 displays $|G(\omega)|^2$ for an MFR design with $c_1=4$, $c_2=5$ and $N=3$. Figure 4.5a displays the z -plane zero plot for this filter. The cluster of controllable zeroes may be observed at $z=1$. Figure 4.5b displays $|G(\omega)|^2$ in the Doppler velocity domain, for a radar frequency of 3 GHz and base sampling interval δ_T of 0.26471 ms (Nyquist velocity of 94 m/s), over an entire Nyquist interval. The passband characteristic of this filter is a typical one for

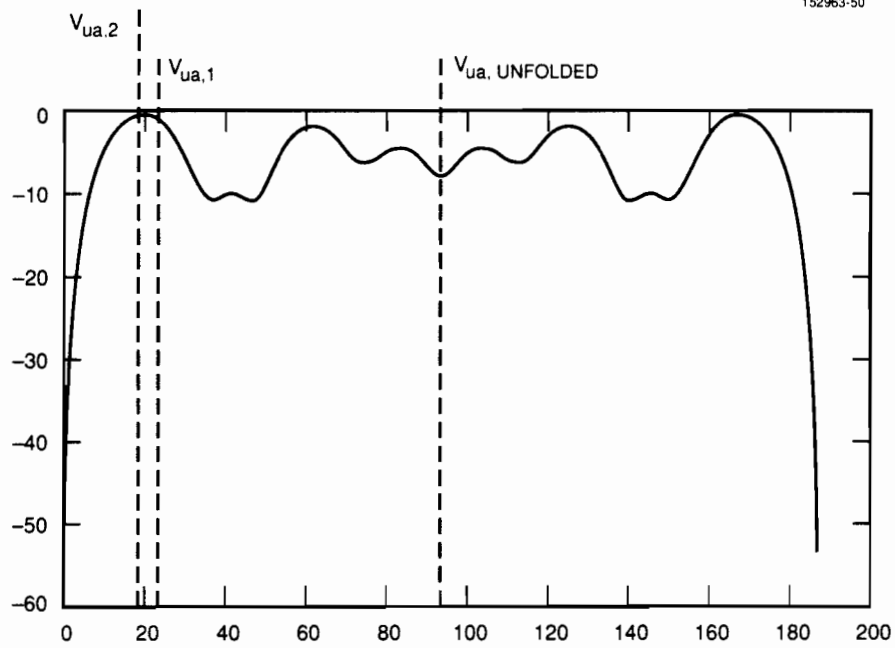


Z-PLANE ZERO PLOT OF $C_0(z)C_0(1/z)+C_1(z)C_1(1/z)$ FOR FILTER 66
NYQUIST FREQUENCY IS $(2\delta_T)^{-1}$ Hz

STAGGER RATIO 4:5
3 FILTER COEFFICIENTS

4 ZEROES AT $z = 1$
MAXIMALLY FLAT DESIGN

Figure 4.5a: Z-Plane zeroes of $|G(\omega)|^2$ for MFR design - $c_1=4$, $c_2=5$ and $N=6$



(MAGNITUDE)² (dB) vs DOPPLER VELOCITY (m/s)
 FILTER ID: 27

STAGGER RATIO 4:5

δ_T IS 0.26471 ms

PRF 1 = 944.4 Hz, PRF 2 = 755.5 Hz

3 FILTER COEFFICIENTS

RADAR FREQUENCY IS 3.00000 GHz

MAXIMALLY FLAT DESIGN

Figure 4.5b: $|G(\omega)|^2$ for MFR design - $c_1=4$, $c_2=5$ and $N=6$

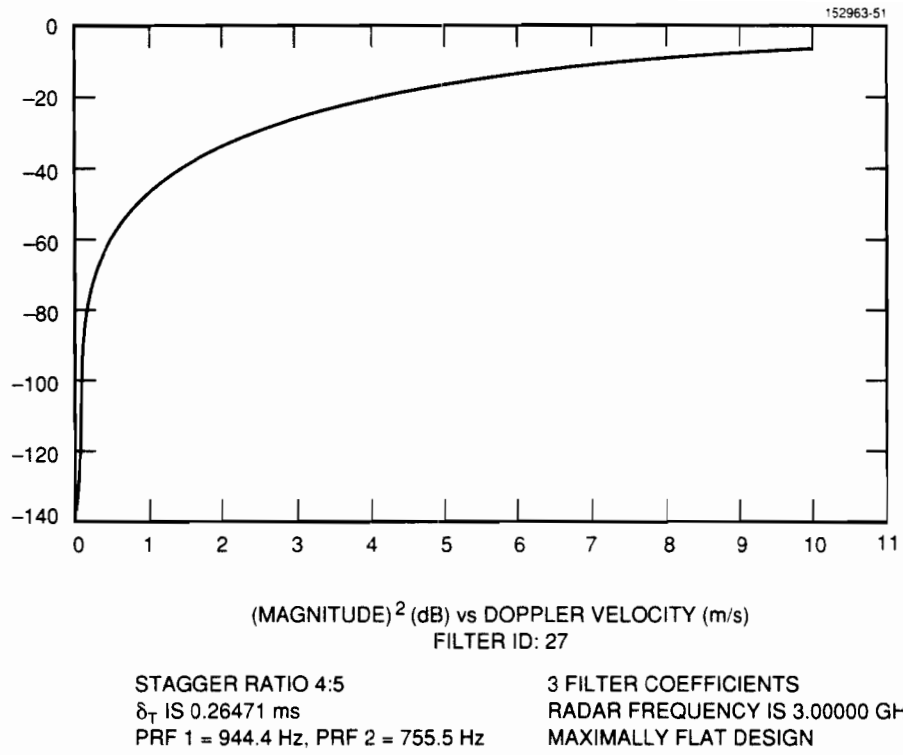
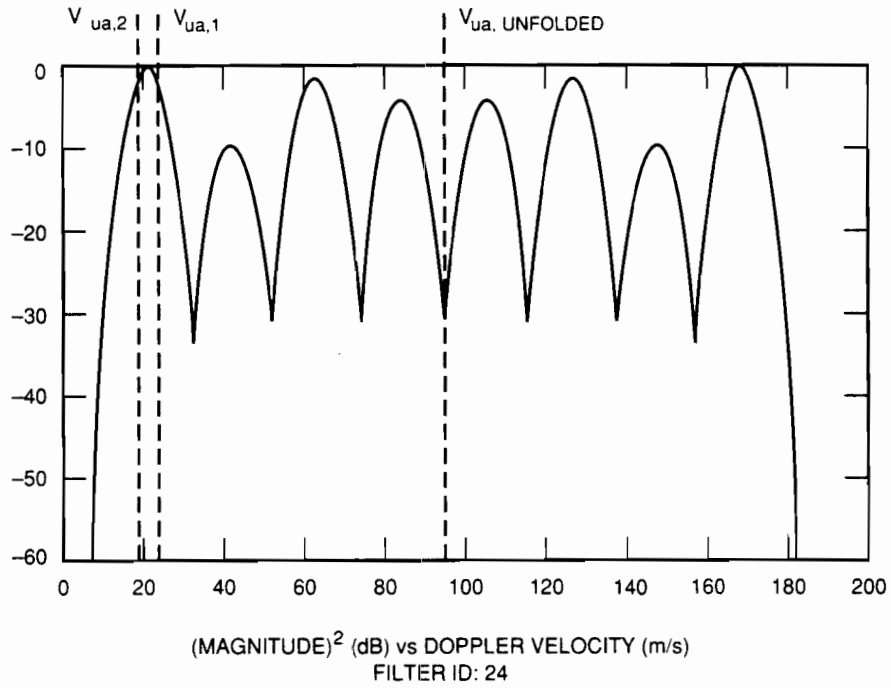


Figure 4.5c: $|G(\omega)|^2$ for MFR design - $c_1=4$, $c_2=5$ and $N=6$

Staggered PRT filters with small values of N . Figure 4.5c is a magnified version of Figure 4.5b, for Nyquist velocities up to 10 m/s. Since scan-modulated, distributed clutter for S-Band weather radars has a spectrum width on the order of 0.25 m/s, we see that this filter provides adequate clutter rejection. The filter has a wide transition region, however, with the 3 dB passband edge located at approximately 15 m/s or at 0.16 of the Nyquist velocity. Even if δ_T were reduced so that the Nyquist velocity were, say, 50 m/s, the filter's stopband and transition band would still cause unacceptable attenuation of weather spectra.

Figure 4.6 displays a Doppler velocity domain plot for an MFR design which possesses the same stagger ratio as the design of Figure 4.5, but with $N=10$. Note the increased width of the stopband, and the increased passband ripple resulting from the additional uncontrollable zeroes. Recall the examples at the end of section 3.3.3 in which stopband width increases were achieved at the expense of moving the passband edge upwards. For larger values of N , the first passband ripple – whose location remains essentially unchanged – serves to fix the passband edge, but the passband ripples are unacceptably deep in these cases.

The MFR design technique is of limited utility in designing clutter filters for weather radar applications, as it does not provide the designer with sufficient control of the filter's stopband and transition region characteristics.



STAGGER RATIO 4:5	10 FILTER COEFFICIENTS
δ_T IS 0.26471 ms	RADAR FREQUENCY IS 3.00000 GHz
PRF 1 = 944.4 Hz, PRF 2 = 755.5 Hz	MAXIMALLY FLAT DESIGN

Figure 4.6: $|G(\omega)|^2$ for MFR design - $c_1=4$, $c_2=5$ and $N=10$

4.3 DESIGN TECHNIQUE: OUTPUT SIGNAL TO CLUTTER RATIO MAXIMIZATION

Unlike the Coefficient Selection and MFR design techniques which are both deterministic approaches to the design of Staggered PRT clutter filters, the Output Signal to Clutter Ratio Maximization (OSCRM) technique selects partial response sequences for the Staggered PRT in such a manner as to maximize the signal to clutter ratio (SCR) in the filter's output sequence.

Given a wide-sense stationary input sequence $\{x_k\} \triangleq \{x(\Delta_k \delta_T)\}$, the staggered PRT filter's output at time $\Delta_l \delta_T$ is

$$y_l = \sum_{k=0}^{N-1} x_{l-k} h_{i,k} \quad , \quad i=l \div 2$$

where $a \div b$ denotes a modulo b . Equivalently, $y_l = \mathbf{h}_i^H \mathbf{x}_l$, $i=l \div 2$ where $\mathbf{x}_l \triangleq [x_l \cdots x_{l-(N-1)}]^T$, $\mathbf{h}_i \triangleq [h_{i,0} \cdots h_{i,N-1}]^H$, and superscript \mathbf{H} 's and \mathbf{T} 's indicate Hermetian and standard transposes, respectively. From equation 3.6 we see that the lag zero autocorrelation of the filter's output sequence is

$$\begin{aligned} R_{yy}(0) &= \mathbf{E}_X \{ |y_l|^2 \} = \frac{1}{2} \mathbf{E}_{X,l \text{ even}} \{ \mathbf{h}_i^H \mathbf{x}_l (\mathbf{h}_i^H \mathbf{x}_l)^H \} + \frac{1}{2} \mathbf{E}_{X,l \text{ odd}} \{ \mathbf{h}_i^H \mathbf{x}_l (\mathbf{h}_i^H \mathbf{x}_l)^H \} \\ &= \frac{1}{2} \left[\mathbf{h}_0^H \mathbf{E}_{X,l \text{ even}} \{ \mathbf{x}_l \mathbf{x}_l^H \} \mathbf{h}_0 + \mathbf{h}_1^H \mathbf{E}_{X,l \text{ odd}} \{ \mathbf{x}_l \mathbf{x}_l^H \} \mathbf{h}_1 \right] \end{aligned} \quad (4.4a)$$

$$= \frac{1}{2} [\mathbf{h}_0^H \mathbf{R}_0 \mathbf{h}_0 + \mathbf{h}_1^H \mathbf{R}_1 \mathbf{h}_1] \quad (4.4b)$$

where

$$\mathbf{R}_i \triangleq \begin{bmatrix} R_{xx}(d_{i,0}-d_{i,0}) & R_{xx}(d_{i,0}-d_{i,1}) & \cdots & R_{xx}(d_{i,0}-d_{i,N-1}) \\ R_{xx}(d_{i,1}-d_{i,0}) & R_{xx}(d_{i,1}-d_{i,1}) & \cdots & R_{xx}(d_{i,1}-d_{i,N-1}) \\ \vdots & \vdots & \ddots & \vdots \\ R_{xx}(d_{i,N-1}-d_{i,0}) & R_{xx}(d_{i,N-1}-d_{i,1}) & \cdots & R_{xx}(d_{i,N-1}-d_{i,N-1}) \end{bmatrix} \quad (4.4c)$$

Weather radar signals contaminated by clutter may be considered as the sum of two independent signals – the sampled returns due to hydrometeors or other particulates in the atmosphere, $\{x_k^w\}$, and the sampled returns due to clutter, $\{x_k^c\}$. We make the assumption that both of these signals may be considered wide-sense stationary over an azimuth dwell time (this assumption becomes increasingly less valid with increasing radar slant range due to beam broadening); and we neglect any non-linearities in the radar receiver which would correlate the weather and clutter signals. The output sequence of the Staggered PRT filter is then the sum of the independent contributions of the filtered weather and clutter processes.

Given the second order statistics of the weather and clutter processes, the SCR at the filter's output is a scalar function of the partial response sequences h_i . Denoting the autocorrelation matrices corresponding to equation 4.4c for the input weather and clutter processes as \mathbf{R}_i^w and \mathbf{R}_i^c , respectively, we see that the output SCR for $i = l \div 2$ is given by

$$\text{SCR}(\mathbf{h}_i) \triangleq \frac{\mathbf{h}_i^H \mathbf{R}_i^w \mathbf{h}_i}{\mathbf{h}_i^H \mathbf{R}_i^c \mathbf{h}_i} \quad (4.5)$$

Later on in this section of the report, we will require models for the weather and clutter power spectral densities which are even functions of Doppler frequency. The corresponding matrices \mathbf{R}_i^w and \mathbf{R}_i^c are then real, symmetric and positive semi-definite. The clutter power spectrum will be modeled as Gaussian with a non-zero spectrum width. This is sufficient to guarantee that \mathbf{R}_i^c will be positive-definite and therefore invertible. In order to simplify the derivation of the OSCRM technique, it will be assumed for the remainder of this section that \mathbf{R}_i^w and \mathbf{R}_i^c are real and symmetric and that \mathbf{R}_i^c is invertible. These assumptions in turn imply real \mathbf{h}_i in the context of OSCRM.

The gradient of $\text{SCR}(\mathbf{h}_i)$ is

$$\begin{aligned} \nabla \text{SCR}(\mathbf{h}_i) &= \frac{\nabla \left(\mathbf{h}_i^T \mathbf{R}_i^w \mathbf{h}_i \right) \left(\mathbf{h}_i^T \mathbf{R}_i^c \mathbf{h}_i \right) - \nabla \left(\mathbf{h}_i^T \mathbf{R}_i^c \mathbf{h}_i \right) \left(\mathbf{h}_i^T \mathbf{R}_i^w \mathbf{h}_i \right)}{\left(\mathbf{h}_i^T \mathbf{R}_i^c \mathbf{h}_i \right)^2} \\ &= 2 \frac{\mathbf{R}_i^w \mathbf{h}_i \left(\mathbf{h}_i^T \mathbf{R}_i^c \mathbf{h}_i \right) - \mathbf{R}_i^c \mathbf{h}_i \left(\mathbf{h}_i^T \mathbf{R}_i^w \mathbf{h}_i \right)}{\left(\mathbf{h}_i^T \mathbf{R}_i^c \mathbf{h}_i \right)^2} \end{aligned}$$

Setting the preceding equation to zero and premultiplying by $\left(\mathbf{R}_i^c \right)^{-1}$, we obtain

$$\left(\mathbf{R}_i^c \right)^{-1} \mathbf{R}_i^w \mathbf{h}_i \left(\mathbf{h}_i^T \mathbf{R}_i^c \mathbf{h}_i \right) = \left(\mathbf{h}_i^T \mathbf{R}_i^w \mathbf{h}_i \right) \mathbf{h}_i$$

or

$$\left(\mathbf{R}_i^c \right)^{-1} \mathbf{R}_i^w \mathbf{h}_i = \left\{ \frac{\mathbf{h}_i^T \mathbf{R}_i^w \mathbf{h}_i}{\mathbf{h}_i^T \mathbf{R}_i^c \mathbf{h}_i} \right\} \mathbf{h}_i = \text{SCR}(\mathbf{h}_i) \mathbf{h}_i \quad (4.6)$$

Equation 4.6 is particularly interesting in that it is an eigenvalue-eigenvector expression for the matrix $\left(\mathbf{R}_i^c \right)^{-1} \mathbf{R}_i^w$ - with eigenvalues $\text{SCR}(\mathbf{h}_i)$ and eigenvectors \mathbf{h}_i . Since we arrived at this result by evaluating $\nabla \text{SCR}(\mathbf{h}_i)$, the desired partial response sequence h_i is the eigenvector of $\left(\mathbf{R}_i^c \right)^{-1} \mathbf{R}_i^w$ corresponding to the eigenvalue of maximum modulus. Results similar to this one, with different derivations, may be found in works of Cadzow [Cadzow80a], and Keeping and Sureau [Keeping78a]

The OSCRM design technique operates as follows.

- 1) Select values for c_1 , c_2 and the filter length N .
- 2) Select models for the weather and clutter spectra which yield real and symmetric \mathbf{R}_i^w and \mathbf{R}_i^c , and a positive-definite \mathbf{R}_i^c .
- 3) For $i = 0, 1$, determine the eigenvalues and eigenvectors of the matrix $\left(\mathbf{R}_i^c\right)^{-1} \mathbf{R}_i^w$. The h_i are then the eigenvectors corresponding to the eigenvalues of maximum modulus for $i = 0, 1$, while the clutter improvement factors for the *assumed* weather and clutter models are the corresponding eigenvalues.

The use of OSCRM requires that some assumptions be made about the statistics of the weather and clutter processes. For land-based weather radar there are basically two types of ground-based clutter: scan-modulated distributed clutter such as trees; and scan-modulated discrete clutter such as isolated buildings and radio towers. At S-Band, with a one degree beam and antenna rotation rates on the order of 3 RPM, the spectrum for distributed clutter is Gaussian and centered at zero frequency with a standard deviation of ≈ 0.25 m/s, while the spectrum for discrete clutter is non-Gaussian and somewhat narrower. The clutter model employed in the OSCRM technique is the generally wider, distributed clutter model. The selection of a model for the weather spectrum is more difficult. Although it is Gaussian, its moments are a function of the prevailing atmospheric conditions. For this purposes of OSCRM, we will employ the generalized weather spectrum depicted in Figure 4.7.

The inputs to OSCRM are then the stagger ratio, N , the clutter spectrum width, σ_c , and the four breakpoints of the generalized weather spectrum, w_1, w_2, w_3 and w_4 . Of course, $0 \leq w_1 \leq w_2 \leq w_3 \leq w_4 \leq \frac{\pi}{\delta_T}$ Hz. When OSCRM is used to generate clutter filters, the values of the parameters w_3 and w_4 are relatively unimportant, as it is the Doppler interval over which the weather and clutter spectra *coexist* that drives the OSCRM design. The OSCRM also includes a parameter α_{sc} which determines the SCR at the Staggered PRT filter's input. For a typical clutter filter design, however, $w_3 - w_2 \gg \sigma_c$ and $w_1 \approx w_2 \approx \sigma_c$, so that α_{sc} has little effect on the resulting design.

Figure 4.8 depicts an OSCRM design for a 3 GHz (S-Band) radar with $\delta_T = 0.45455$ ms, corresponding to a Nyquist velocity of 55 m/s. The stagger ratio in this case is 2:3, with a filter length of $N=3$. Figure 4.8a displays the z-plane zero distribution for $|G(\omega)|^2$, while Figure 4.8b displays the corresponding Doppler domain plot. The text blocks on the lower right-hand corner of the plots display the

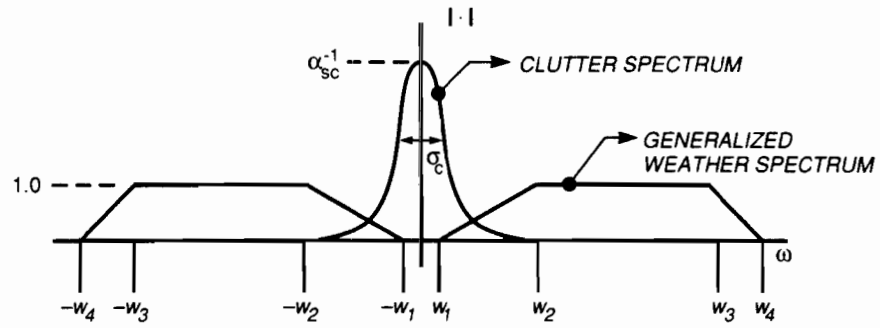
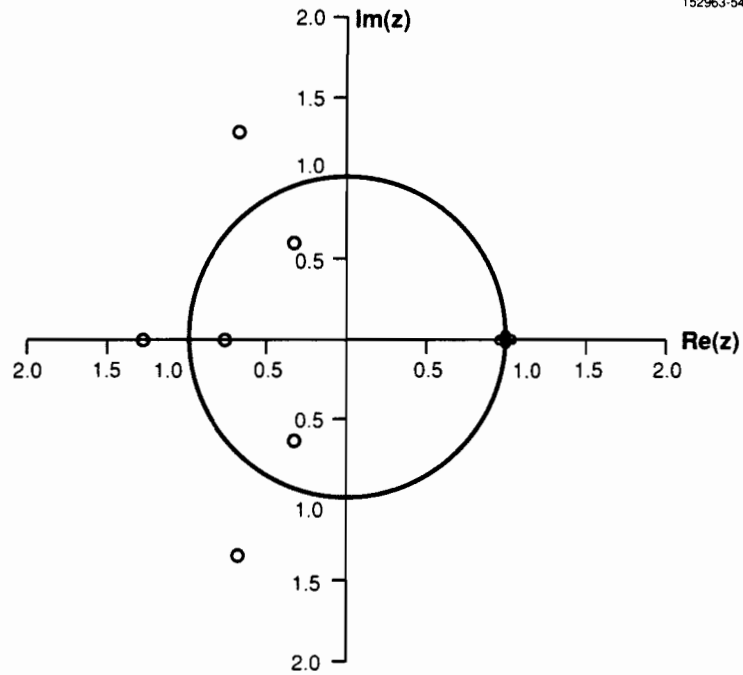


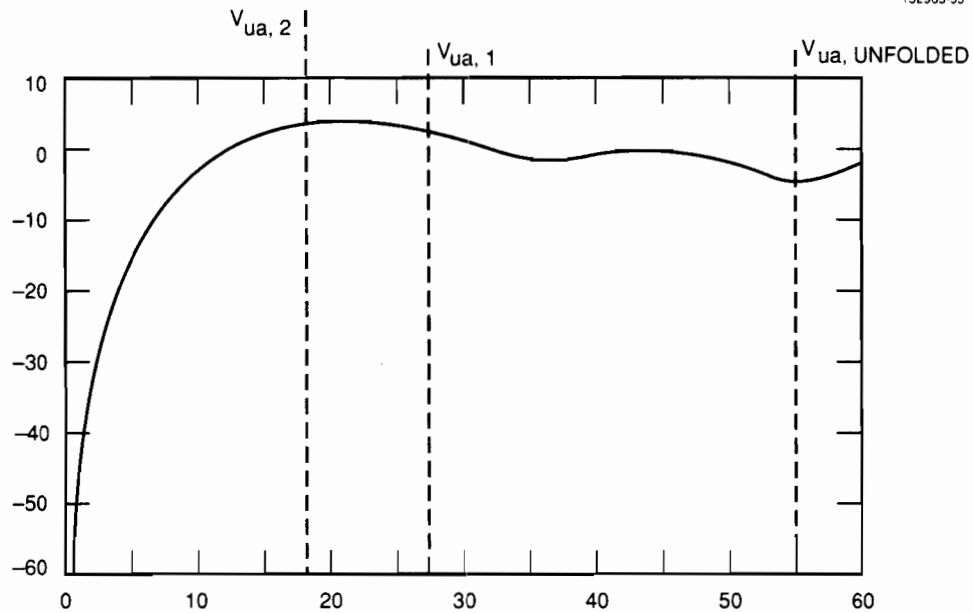
Figure 4.7: Doppler domain input parameters for OSCR design technique



Z-PLANE ZERO PLOT OF $C_0(z)C_0(1/z) + C_1(z)C_1(1/z)$ FOR FILTER 233
 NYQUIST FREQUENCY IS $(2\delta_T)^{-1}$ Hz

STAGGER RATIO 2:3	AUTOCORRELATION-BASED DESIGN:
3 FILTER COEFFICIENTS	INPUT S/C POWER RATIO: -10.0 dB
4 ZEROES AT $z = 1$	OUTPUT S/C POWER RATIOS: 62.2 dB, 62.2 dB
	NORMALIZED CLUTTER WIDTH: 0.00273
	NORMALIZED W-SPECTRUM BREAKPOINTS:
	0.00000 0.00200 0.85000 1.00000

Figure 4.8a: Z-Plane zeroes of $|G(\omega)|^2$ for OSCR design - $c_1=2$, $c_2=3$ and $N=3$



(MAGNITUDE)² (dB) vs DOPPLER VELOCITY (m/s)
 FILTER ID: 233

STAGGER RATIO 2:3	AUTOCORRELATION-BASED DESIGN:
δ_T IS 0.45455 ms	INPUT S/C POWER RATIO: -10.0 dB
PRF 1 = 1100.0 Hz, PRF 2 = 733.3 Hz	OUTPUT S/C POWER RATIOS: 62.2 dB,
3 FILTER COEFFICIENTS	62.2 dB
RADAR FREQUENCY IS 3.00000 GHz	NORMALIZED CLUTTER WIDTH: 0.00273
	NORMALIZED W-SPECTRUM BREAKPOINTS:
	0.00000 0.00200 0.85000 1.00000

Figure 4.8b: $|G(\omega)|^2$ for OSCR design - $c_1=2$, $c_2=3$ and $N=3$

OSCRM parameters with σ_c and the w_i normalized to the Nyquist velocity. The unnormalized values are $\sigma_c=0.15$ m/s, $w_1=0$ m/s, $w_2=0.11$ m/s, $w_3=47$ m/s and $w_4=55$ m/s. These w_i were selected to generate a generalized weather spectrum which essentially coexists with the clutter spectrum, but with a diminished weighting for the weather about zero velocity. α_{sc} , the input SCR, was set to -10 dB.

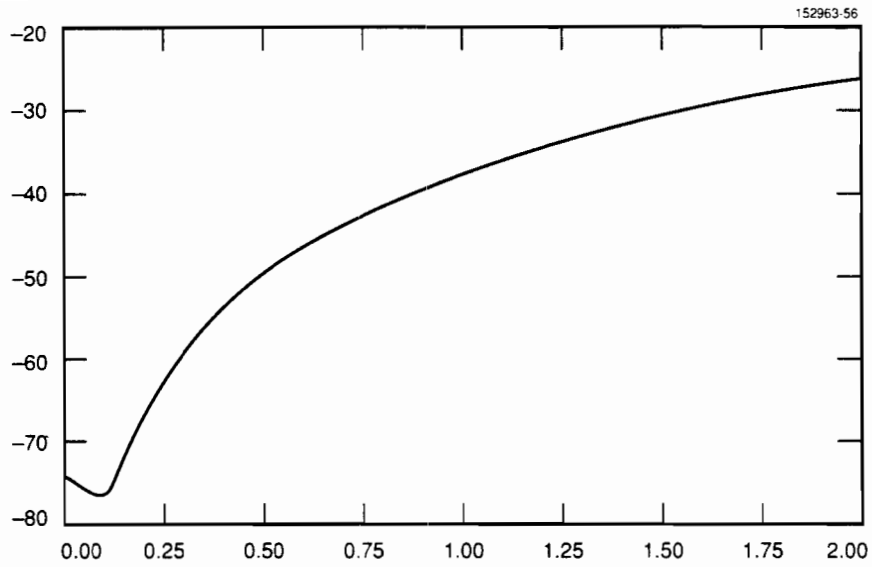
The output SCR's for h_0 and h_1 , maximum modulus eigenvalues of the $(\mathbf{R}_i^c)^{-1} \mathbf{R}_i^w$, appear in the lower right-hand text block as 62.2 dB for $i = 0,1$, indicating a clutter improvement factor of 72.2 dB for the assumed weather and clutter spectra. An equispaced FIR filter with three coefficients would not generally provide this amount of clutter rejection. Comparing Figure 4.8a with the corresponding MFR design in Figure 3.14a, we see that the OSCRM design technique generates a looser cluster of controllable zeroes at $z=1$. This is a result of the OSCRM's attempt to cancel clutter with a non-zero spectrum width; Figure 4.8b correspondingly displays a wider stopband than Figure 3.14b. The transition region and passband characteristics of the design are largely determined by the uncontrollable zeroes, however, so that Figures 4.8b and 3.14b agree in these two respects.

Figure 4.9 displays the clutter improvement factor of the design depicted in Figure 4.8 for the distributed clutter model as a function of the clutter spectrum width in m/s. Note that the clutter rejection exceeds 40 dB for spectrum widths up to ≈ 0.8 m/s. Also note the minimum in the rejection characteristic at σ_c .

Figure 4.10 displays the clutter improvement factor for scan-modulated discrete clutter targets as a function of antenna rotation rate. Four data points are plotted. The data displayed in Figure 4.10 were calculated with the assumption of an antenna with a uniformly illuminated circular aperture [Skolnik80a]. The numbers next to each datum in the figure indicate the angular distance swept out to either side of the target in the simulation. The filter's improvement factor for this class of clutter is acceptable for weather radar applications.

Figures 4.11a and 4.11b display the bias introduced by the filter for R_0 reflectivity estimates, as a function of the mean velocity of the weather spectrum. Figure 4.11a displays the bias for a spectrum width of 4 m/s, while Figure 4.11b was generated for a spectrum width of 7 m/s. Note that while the performances depicted are comparable for mean velocities greater than 10 m/s, the biases induced by incursions of the weather spectra into the transition region and stopband are greater for narrower spectrum widths, as expected.

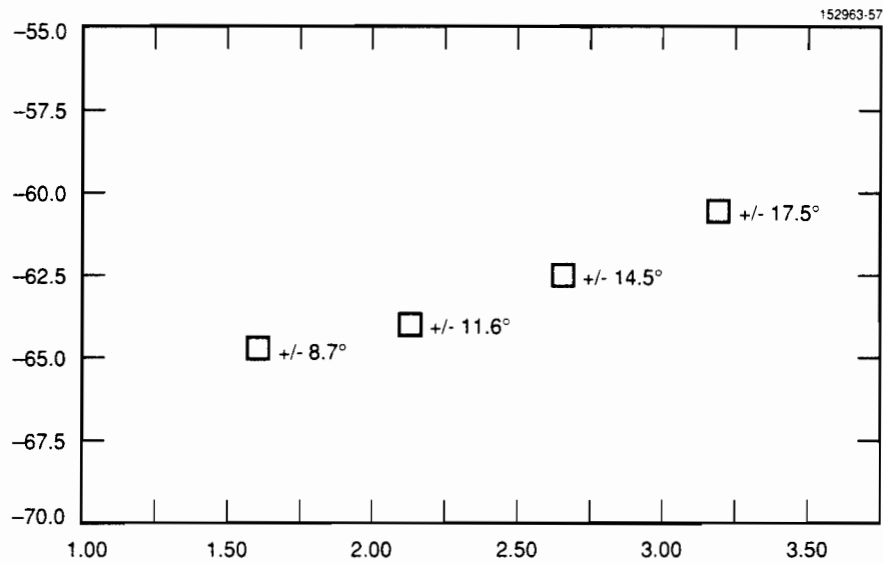
Figure 4.12 depicts an OSCRM design which is identical to that of Figure 4.8 except that the stagger ratio is 5:7 rather than 2:3. The point of this figure is to show that the passband and transition region characteristics are strongly dependent upon the choice of stagger ratio. The design displayed in Figure 4.12 possesses a transition region which is half the width of that displayed in Figure 4.8. This is achieved, however, at the expense of doubling the peak-to-peak passband ripple



NORMALIZED TYPE A CLUTTER REJECTION (dB) vs
 CLUTTER SPECTRUM WIDTH (m/s)
 FILTER ID: 233

STAGGER RATIO 2:3	AUTOCORRELATION-BASED DESIGN:
δ_T IS 0.45455 ms	INPUT S/C POWER RATIO: -10.0 dB
PRF 1 = 1100.0 Hz, PRF 2 = 733.3 Hz	OUTPUT S/C POWER RATIOS: 62.2 dB,
3 FILTER COEFFICIENTS	62.2 dB
RADAR FREQUENCY IS 3.00000 GHz	NORMALIZED CLUTTER WIDTH: 0.00273
	NORMALIZED W-SPECTRUM BREAKPOINTS:
	0.00000 0.00200 0.85000 1.00000

Figure 4.9: Distributed clutter rejection for OSCR design of figure 4.8

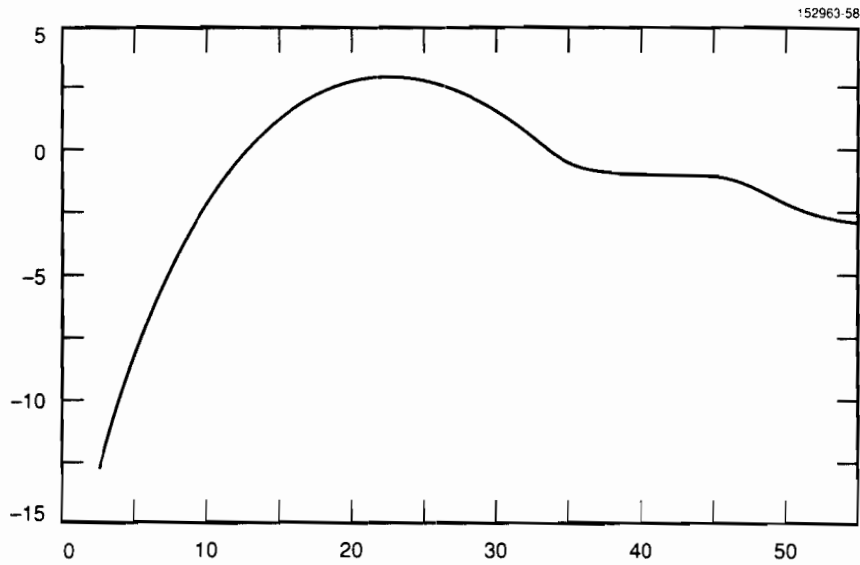


NORMALIZED TYPE B CLUTTER REJECTION (dB) vs
 ANTENNA ROTATION RATE (rpm)
 FILTER ID: 233

STAGGER RATIO 2:3	AUTOCORRELATION-BASED DESIGN:
δ_T IS 0.45455 ms	INPUT S/C POWER RATIO: -10.0 dB
PRF 1 = 1100.0 Hz, PRF 2 = 733.3 Hz	OUTPUT S/C POWER RATIOS: 62.2 dB,
3 FILTER COEFFICIENTS	62.2 dB
RADAR FREQUENCY IS 3.00000 GHz	NORMALIZED CLUTTER WIDTH: 0.00273
	NORMALIZED W-SPECTRUM BREAKPOINTS:
	0.00000 0.00200 0.85000 1.00000

ONE-WAY, HALF-POWER, ANTENNA BEAMWIDTH IS 1.0°

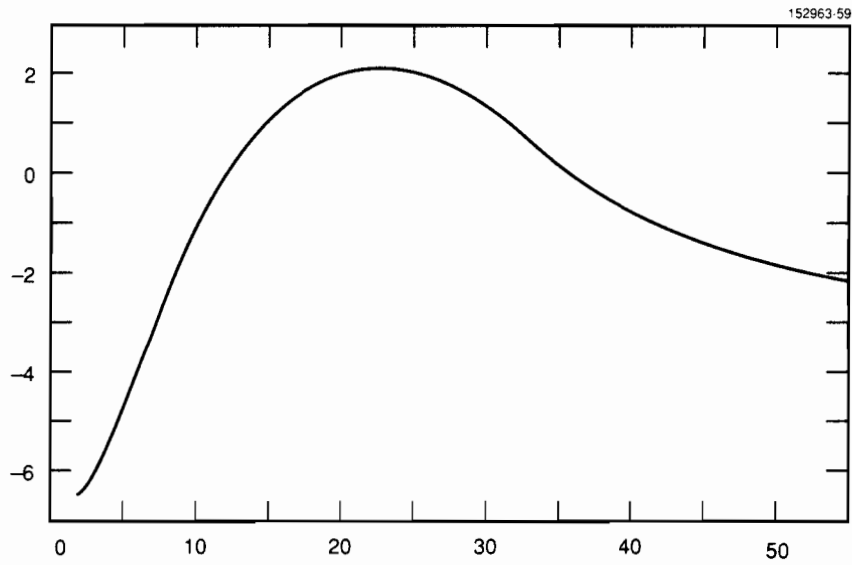
Figure 4.10: Discrete clutter rejection for OSCR design of figure 4.8



REFLECTIVITY ESTIMATE ERROR (dBz) vs MEAN WEATHER VELOCITY (m/s)
 FILTER ID: 233

WEATHER SPECTRUM WIDTH IS 4.0 m/s	AUTOCORRELATION-BASED DESIGN:
MINIMUM DISPLAYED VELOCITY: 2.0 m/s	INPUT S/C POWER RATIO: -10.0 dB
STAGGER RATIO 2:3	OUTPUT S/C POWER RATIOS: 62.2 dB,
δ_T IS 0.45455 ms	62.2 dB
PRF 1 = 1100.0 Hz, PRF 2 = 733.3 Hz	NORMALIZED CLUTTER WIDTH: 0.00273
3 FILTER COEFFICIENTS	NORMALIZED W-SPECTRUM BREAKPOINTS:
RADAR FREQUENCY IS 3.00000 GHz	0.00000 0.00200 0.85000 1.00000
NYQUIST SPECTRAL FOLDING ENFORCED	

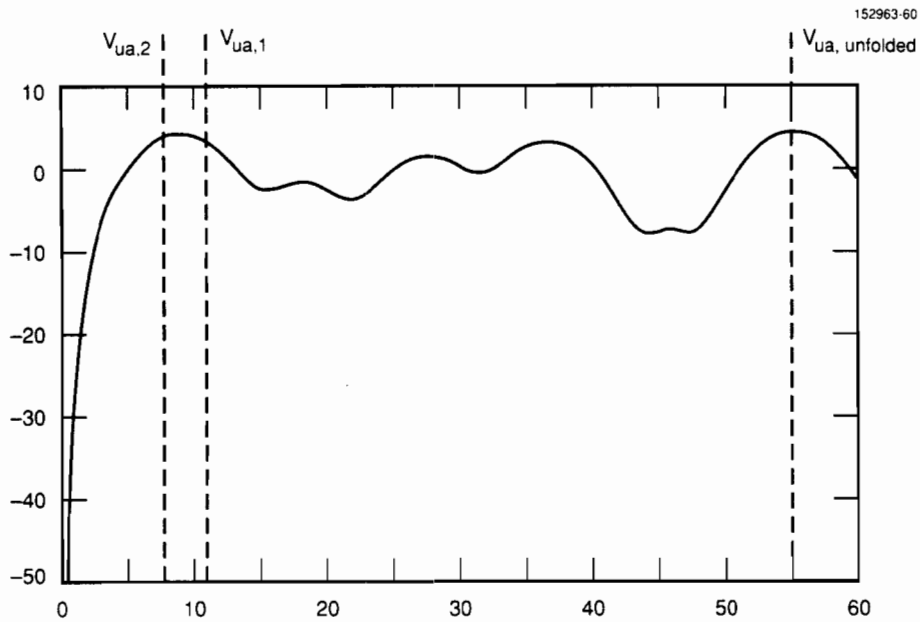
Figure 4.11a: Reflectivity estimate bias for OSCR design of figure 4.8 - $\sigma_v = 4$ m/s



REFLECTIVITY ESTIMATE ERROR (dBz) vs MEAN WEATHER VELOCITY (m/s)
 FILTER ID: 233

WEATHER SPECTRUM WIDTH IS 7.0 m/s	AUTOCORRELATION-BASED DESIGN:
MINIMUM DISPLAYED VELOCITY: 2.0 m/s	INPUT S/C POWER RATIO: -10.0 dB
STAGGER RATIO 2:3	OUTPUT S/C POWER RATIOS: 62.2 dB,
δ_T IS 0.45455 ms	62.2 dB
PRF 1 = 1100.0 Hz, PRF 2 = 733.3 Hz	NORMALIZED CLUTTER WIDTH: 0.00273
3 FILTER COEFFICIENTS	NORMALIZED W-SPECTRUM BREAKPOINTS:
RADAR FREQUENCY IS 3.00000 GHz	0.00000 0.00200 0.85000 1.00000
NYQUIST SPECTRAL FOLDING ENFORCED	

Figure 4.11b: Reflectivity estimate bias for OSCR design of figure 4.8 - $\sigma_v = 7$ m/s



(MAGNITUDE)² (dB) vs DOPPLER VELOCITY (m/s)
 FILTER ID: 573

STAGGER RATIO 5:7	AUTOCORRELATION-BASED DESIGN:
δ_T IS 0.45455 ms	INPUT S/C POWER RATIO: -10.0 dB
PRF 1 = 440.0 Hz, PRF 2 = 314.3 Hz	OUTPUT S/C POWER RATIOS: 46.5 dB,
3 FILTER COEFFICIENTS	46.5 dB
RADAR FREQUENCY IS 3.00000 GHz	NORMALIZED CLUTTER WIDTH: 0.00273
	NORMALIZED W-SPECTRUM BREAKPOINTS:
	0.00000 0.00200 0.85000 1.00000

Figure 4.12: $|G(\omega)|^2$ for OSCRM design - $c_1=5$, $c_2=7$ and $N=3$

relative to Figure 4.8. The clutter improvement factor for this design is 56.5 dB.

Within the constraints of Staggered PRT filters, the OSCRM technique appears to be the most effective design technique. It allows the designer to match the filter's magnitude response to both the weather and clutter spectra; although the resulting lag c_1 and lag c_2 transfer functions are subject to the phase difficulties discussed earlier.

5.0 CONCLUSIONS

We have seen that weather radars like the TDWR operate at S-Band or C-Band (2-7 GHz); and that accurate Doppler measurements for phenomena such as gustfronts require an unambiguous velocity of at least 12 m/s. This minimum unambiguous velocity corresponds to maximum unambiguous ranges of approximately 300 and 150 km at S-Band and C-Band, respectively. We noted that regions of significant reflectivity could be sensed beyond 300 km at low elevation angles, and hence that obscuration of low reflectivity, in-trip, phenomena by high-reflectivity, out-of-trip, weather would occasionally occur. We cited studies in which microburst windspeeds above 30 m/s had been observed, and concluded that Doppler weather radars operating at S and C-Bands must contend with degrees of both range obscuration and velocity aliasing. A distinction was made between relative and absolute velocity de-aliasing; it was stated that absolutely de-aliased velocity observations are required for certain automated weather detection functions (*e.g.* the Sectorized Uniform Wind Algorithm). We showed that a clutter rejection capability in excess of 50 dB is required if a 10 dB signal to clutter ratio is to be maintained for low-reflectivity, low-altitude, phenomena.

We have also seen that mean velocity estimates generated from a radar pulse train with two PRT's may be combined to form an estimate which is unambiguous over a velocity interval larger than that corresponding to either of the two PRT's. For two relatively prime positive integers, c_1 and c_2 , estimates from a pulse train with embedded PRT's of $c_1\delta_T$ and $c_2\delta_T$ may be combined to form estimates with a Nyquist interval corresponding to a PRT of δ_T . Two such pulse trains were described, the Batch PRT scheme in which the azimuth dwell time is divided into two blocks of equispaced PRT pulses; and the Staggered PRT scheme in which the PRT alternates from pulse to pulse. The Staggered PRT scheme has the advantage over the Batch PRT scheme of spatial coherency for velocity estimates at the two PRT's; and we noted that the Batch PRT scheme may not effectively support velocity de-aliasing in the presence of azimuthal shear.

5.1 BATCH PRT

With azimuth dwell times of 40 to 50 ms (20 to 25 degree/sec azimuth scanning rates), time-domain clutter rejection techniques such as FIR filtering do not seem practical with a Batch PRT sampling scheme. This is due to the desire for a narrow filter transition region and a sufficient number of samples at the filter's output to generate autocorrelation estimates with small variances. A clutter rejection technique based on the windowed periodogram of the radar return sequence was described; and an expression was developed which characterized the performance of a data taper in this application. The taper performance was expressed as a function of the ratio of the filter cut-off frequency and the clutter spectrum width. This same expression can be used to characterize the performance of data tapers in minimizing

biases of the spectral characteristics of the weather process, in particular the spectrum width.

S-Band clutter rejection examples were provided for the cases of single PRT and Block PRT schemes with 40 and 50 ms azimuth dwell times. We saw that the performance of a given data taper for this application seemed to be driven by its frequency-domain sidelobe characteristics rather than its main lobe width. For the single PRT case, the requisite clutter rejection was available at scanning rates of 20 and 25 degrees/sec with a 3 m/s passband edge and the Blackman or Dolph-Chebyshev tapers. For the Batch PRT scheme with the same range of dwell times, however, the necessary rejection was only available with a passband edge on the order of 6 m/s, which would not be acceptable for subsequent de-aliasing operations. In the absence of a substantially improved data taper design, we concluded that either the azimuth dwell time must be increased beyond 50 ms or the 50 dB rejection requirement relaxed, if the Batch PRT scheme was to be viable.

5.2 STAGGERED PRT

A filter structure capable of processing data sequences with the unequal inter-sample delays embedded in a Staggered PRT pulse train was described. The filter is comprised of two linear time-invariant FIR filters, but the overall structure is time-varying. Elements of a general theory for these filters were developed, with a particular emphasis on the processing of stochastic signals. One of the distinguishing features of these filters was that a minority of the zeroes of the filter's Z-Transform were controllable. It was seen that this filter structure possessed three effective power transfer functions, depending upon the lag at which the autocorrelation function of the filter's output was computed. The power transfer function at lags $p(c_1+c_2)$, $p \in \mathbf{I}$ was observed to be real and even, while the power transfer functions at lags $p(c_1+c_2)+c_2$ and $p(c_1+c_2)+c_1$, $p \in \mathbf{I}$ generally possessed non-zero phase characteristics. For clutter filtering applications with short impulse response durations in the component FIR filters (*i.e.* all controllable zeroes near $z=1$), we saw that the selection of stagger ratio determined both the filter's passband performance and its z-plane zero distribution.

The phase characteristics of the lag c_1 and lag c_2 transfer functions, and their interaction with velocity estimation, were discussed in section 3.2.2. We saw that a linear phase characteristic was possible for even values of N , and that the estimators of equations 3.8 could then be employed to produce correctly de-aliased velocity estimates. It was noted that discontinuous "linear" phase characteristics seem to be more common than truly linear phase characteristics and that equations 3.8 do not correct for phase discontinuities. Even values of N also resulted in discrepancies in the magnitude responses of the lag $p(c_1+c_2)$ and lag $p(c_1+c_2)+c_1$ transfer functions. We showed that the magnitude responses of these transfer functions could be matched perfectly with odd N and $h_0=h_1$.

Three Staggered PRT filter design techniques were presented along with representative designs. The first technique, Coefficient Selection, generated an appropriate equispaced FIR design and converted that design to a Staggered PRT partial response sequence by time-alignment. We saw that although the DFT is an isometry – equivalently, that such a partial response sequence was a minimum norm approximation to the FIR equispaced design in the time and DFT domains – the partial response sequence’s Z-Transform will typically possess a local maximum in its relative error at $\omega=0$ for clutter filter designs. The second design technique, MFR, placed all controllable zeroes of the filter at the origin. The resulting designs possessed a deep notch at $\omega=0$, but MFR did not afford the designer with adequate stopband and transition region control. The final design technique was the OSCRM technique, which maximized the filter’s output signal to clutter ratio based on spectral models for the weather and clutter processes. A sample OSCRM design was presented, and its rejection performances for both scan-modulated distributed and discrete clutter were seen to be satisfactory. Pulse-pair reflectivity estimate errors for this design were also evaluated.

The sample filter designs presented in this report all possessed partial response sequences with a small number of coefficients. A number of designs were attempted with larger numbers of coefficients (10 to 50) in the hope that filters with narrower transition regions could be realized. In all these cases, the increased passband ripple resulting from the large number of uncontrollable zeros offsets any performance benefits that might result from a narrower transition region.

5.3 FURTHER RESEARCH

Before the Staggered PRT scheme can be declared to be either appropriate or inappropriate for Doppler weather radar applications, an improved understanding of the properties of staggered PRT filters and their interaction with Doppler moment estimation will be required. The two most outstanding issues in this respect are the z-plane distribution of the filters’ uncontrollable zeroes, and the phase responses of the lag c_1 and lag c_2 transfer functions. In regard to the former issue, the $C_i(z)$ possess a great deal of structure and one would initially anticipate some success in analytically characterizing the z-plane locations as a function of the stagger ratio – especially for those cases in which all controllable zeroes are placed at $z=1$. The problem, however, has resisted a solution. A seemingly promising approach would be a linear systems analysis of the staggered PRT filter as a single-input, multi-output, system. There are results available for the eigenvalues of sparse matrices which might then be applied to determine the zero locations.

In section 3.3.2 we showed that linear phase (possibly with jump discontinuities) was guaranteed for $C_0(e^{j\omega\delta_T})C_1^*(e^{j\omega\delta_T})$ with an odd value of N and odd, in the sense of that section, h_i . It would be surprising if this constituted the entirety of lag c_1 transfer functions with linear phase. If one could select the h_i so that $C_0(e^{j\omega\delta_T})$

and $C_1(e^{j\omega\delta_T})$ had the same phase characteristic, for instance, one would have a lag c_1 transfer function with zero phase. The design techniques presented in this report independently generated h_0 and h_1 . A staggered PRT filter design technique which simultaneously generated the partial response sequences, incorporating constraints on the lag c_1 and lag c_2 phase responses, would be valuable.

Alternatively, a staggered IIR allpass filter could be employed to adjust the phase characteristics of the lag c_1 and lag c_2 phase responses. Preliminary results have shown that such filters, applied in advance of the partial response sequences, can effect, for instance, a phase characteristic with regions of zero slope. The IIR filters evaluated to date average over input and output samples separated by $(c_1+c_2)\delta_T$, however, and thus possess Nyquist intervals which are smaller than those of the overall Staggered PRT filter. When $C_0(e^{j\omega\delta_T})C_1^*(e^{j\omega\delta_T})$ has linear phase, the result is a net lag c_1 phase response which is periodic within the interval $(-\pi\delta_T^{-1}, \pi\delta_T^{-1}]$, with regions of zero and non-zero slope.

It was noted in section 3.3.2 that properly de-aliased velocity estimates from the staggered PRT filter's output sequence could possess a bias. It was suggested that this results from variations in the lag c_1 and lag c_2 transfer functions' passband magnitude response. An alternative estimation technique is to use the de-aliased staggered PRT estimate to "steer" an accurately aliased velocity estimate to the proper Nyquist interval. This latter estimate would be obtained from an equispaced clutter filter operating at a decimated sampling rate, say $d_e\delta_T$, relative to δ_T . The equispaced filter could be designed to have a great deal less passband variation than the staggered PRT filter, as well as a narrower transition band. We will refer to this combination of equispaced and staggered PRT filters as a *composite* filter.

An equispaced pulse sequence would be embedded in the staggered PRT sequence to form the composite sequence of Figure 5.1, where $c_1=2$, $c_2=3$ and $d_e=3$. This composite sequence has a period of $\text{LCM}\{d_e, c_1+c_2\}\delta_T$ (where LCM denotes Least Common Multiple) and a pulse density that is slightly higher than that of the staggered PRT sequence - in the case of Figure 5.1, 60% versus 40% of the available pulse locations at PRT δ_T . We note that Figure 5.1 includes some pulse spacings of δ_T which would increase the likelihood of obscuration. Figure 5.2 is an overlay of an OSCRM $|G(\omega)|^2$ and the squared magnitude response of a 29 point equiripple clutter filter design ($c_1=2$, $c_2=2$, $N=3$ and $d_e=3$). v_u is 55 m/s ($\lambda=10$ cm) for this example and the first alias of the equispaced filter's stopband is evident at $2/3v_u=362/3$ m/s. For narrow spectrum widths and mean velocities near this aliased stopband, only the staggered PRT filter's velocity estimate will be available.

The velocity estimation procedure is depicted in Figure 5.3. The received pulse train is decomposed into its staggered and equispaced components. The top chain in

- COMPOSITE SAMPLE SEQUENCE IS DECOMPOSED INTO EQUISPACED AND STAGGERED PRT SEQUENCES

- STAGGERED PULSE INTERVALS: $C_1\delta_T, C_2\delta_T$

- EQUISPACED PULSE INTERVAL: $d_e\delta_T$

C_1, C_2, d_e ARE INTEGERS

e.g., $C_1 = 2, C_2 = 3, d_e = 3$

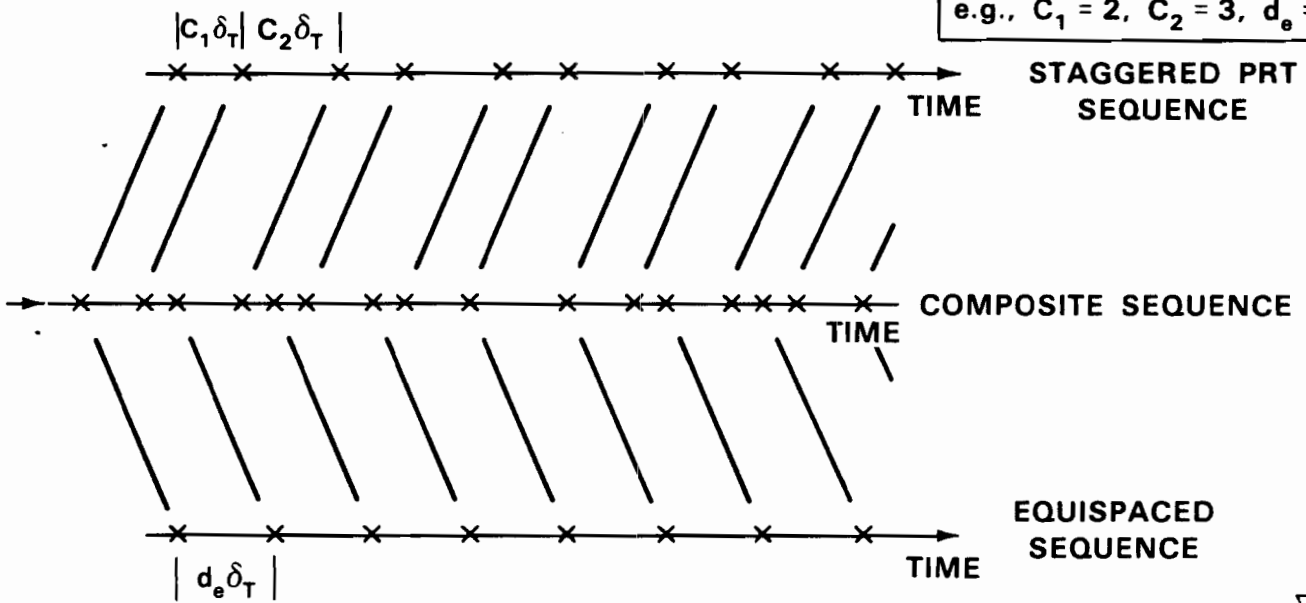
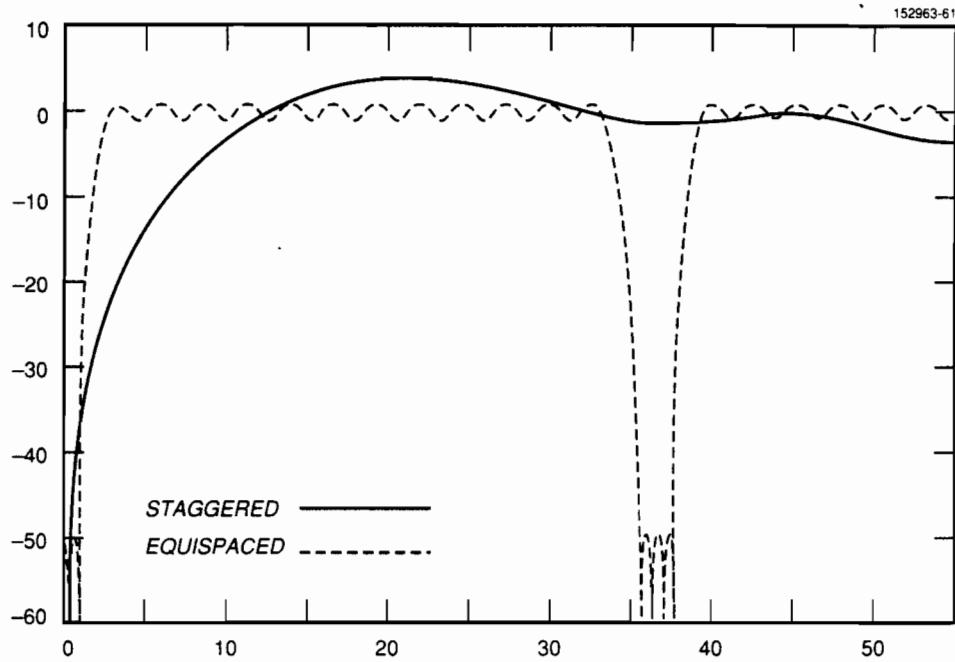


Figure 5.1: Sample association for composite pulse sequence - $c_1=2, c_2=3$ and $d_e=3$



COMPOSITE (MAGNITUDE)² RESPONSES (dB) vs DOPPLER VELOCITY (m/s)

FILTER IDs: STAGGERED - 233
 EQUISPACED - 3303
 δ_T IS 0.45455 ms
 RADAR FREQUENCY IS 3.000 GHz
 STAGGER RATIOS:
 STAGGERED FILTER - 2:3
 EQUISPACED DECIMATION RATE - 3

Figure 5.2: Composite filter transfer functions - $c_1=2$, $c_2=3$, $d_e=3$, $N=3$ and an equispaced filter with 29 coefficients

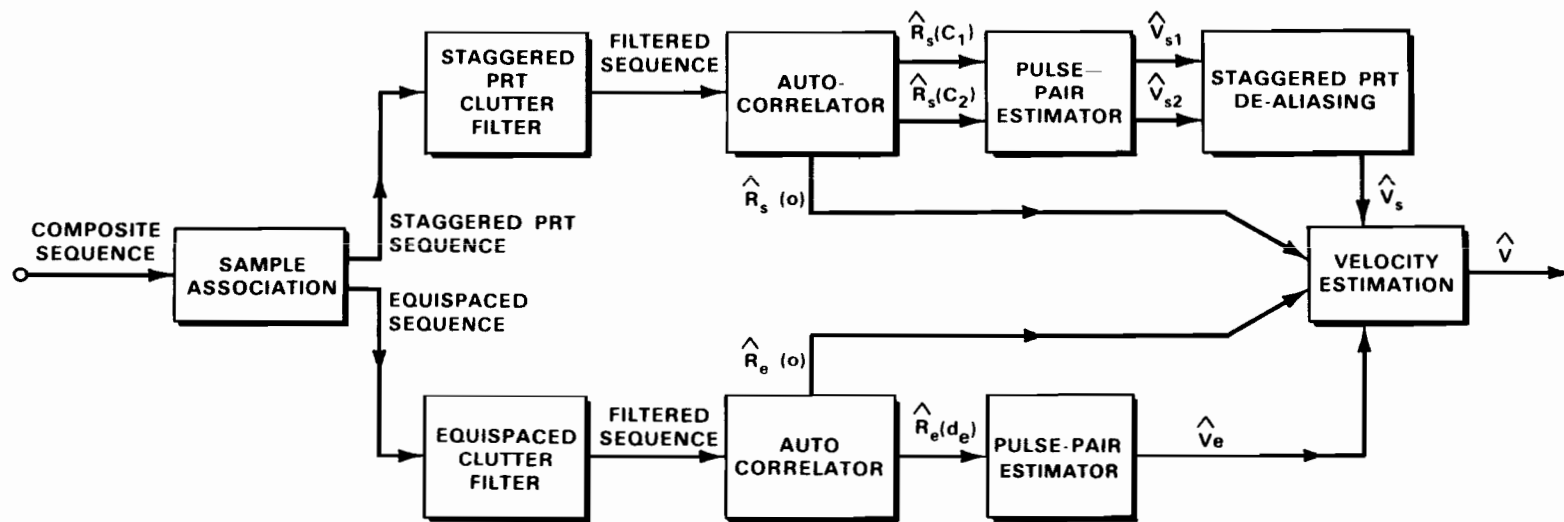


Figure 5.3: Composite filter structure for velocity estimation

the filter is the staggered PRT velocity estimation scheme described in this report; the bottom chain is conventional pulse-pair estimation at the output of the equispaced filter. The two velocity estimates, labeled \hat{v}_s and \hat{v}_e , for staggered and equispaced, are combined in the block labeled *velocity estimation* to produce the final estimate. The mechanism of that block is diagrammed in Figure 5.4. The ratio of the lag zero staggered and equispaced autocorrelation estimates, $R_s(0)/R_e(0)$, is compared to a threshold K . If that ratio is $\leq K$, the staggered PRT velocity estimate is used to determine the proper Nyquist interval for the equispaced velocity estimate. If the ratio is $>K$, the weather is assumed to have aliased to the equispaced filter's stopband, and the staggered PRT velocity estimate is used.

Figure 5.5 provides an example of the velocity estimate errors for the composite filter of Figure 5.2 assuming infinite data and no clutter. $|G(\omega)|^2$ was substituted for the lag c_1 and lag c_2 transfer functions – errors due to the phase characteristics of those transfer functions are not considered here. The weather spectrum width is 1 m/s and $K=1.1$. The horizontal dashed lines in the figure identify velocity regions where $R_s(0)/R_e(0) \leq K$, the estimates in the velocity regions identified by the horizontal solid lines are obtained directly from the staggered PRT filter. As expected, the staggered PRT estimates are relied upon in the region around the alias of the equispaced filter's stopband. They are also relied upon for mean velocities from 14 to 32 m/s, due to the relatively higher passband gain of the staggered PRT filter in that region. The magnitudes of the errors displayed in this figure, ≤ 0.55 m/s, are considerably less than those of the staggered PRT velocity estimates (*e.g.* as in Figure 3.10); there are also encouraging preliminary results for the estimation of reflectivity and spectrum width with a composite filter. Composite filtering schemes merit further investigation, but improved control over the phase responses of the lags c_1 and c_2 transfer functions will also be necessary in this context.

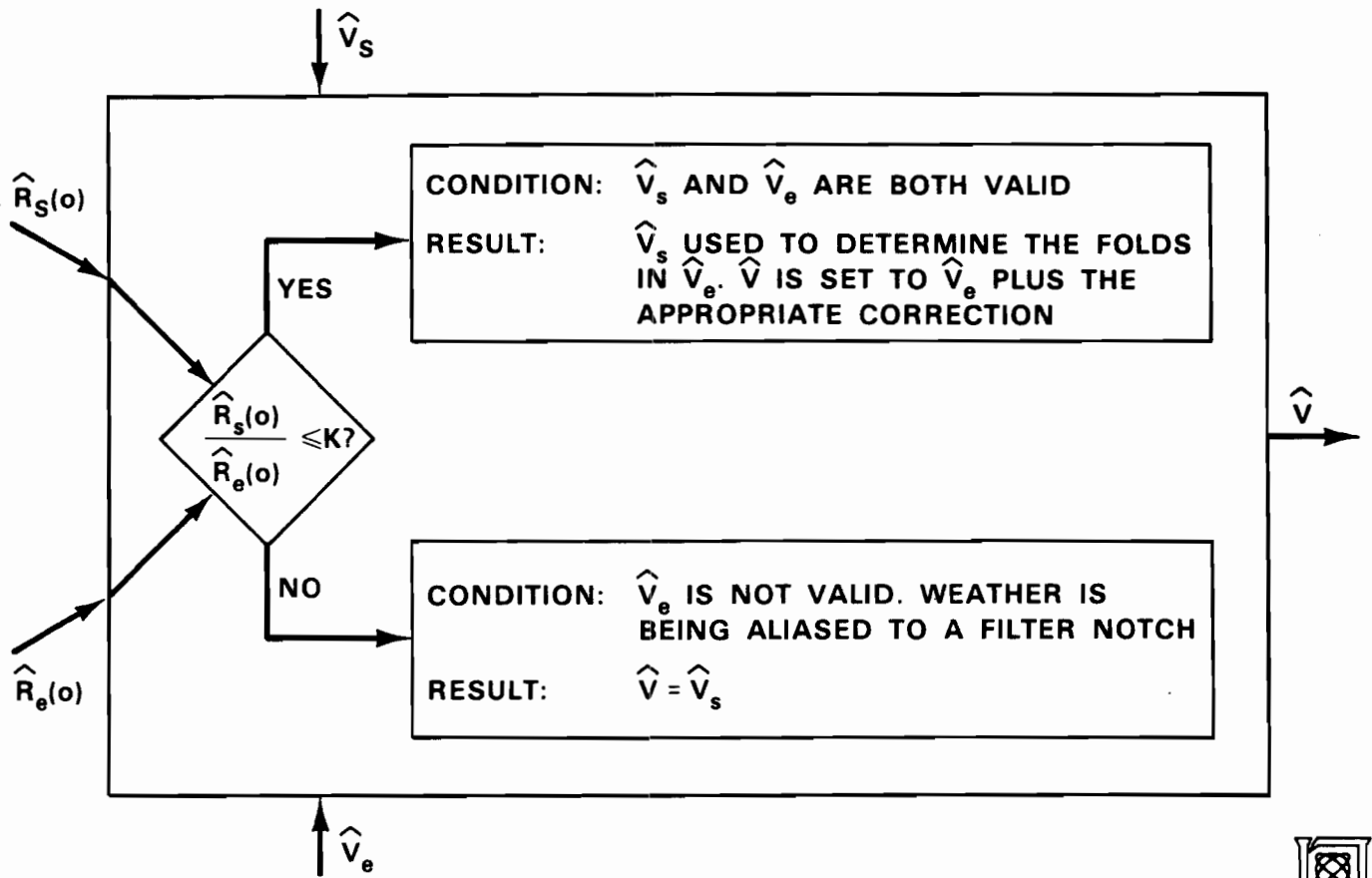
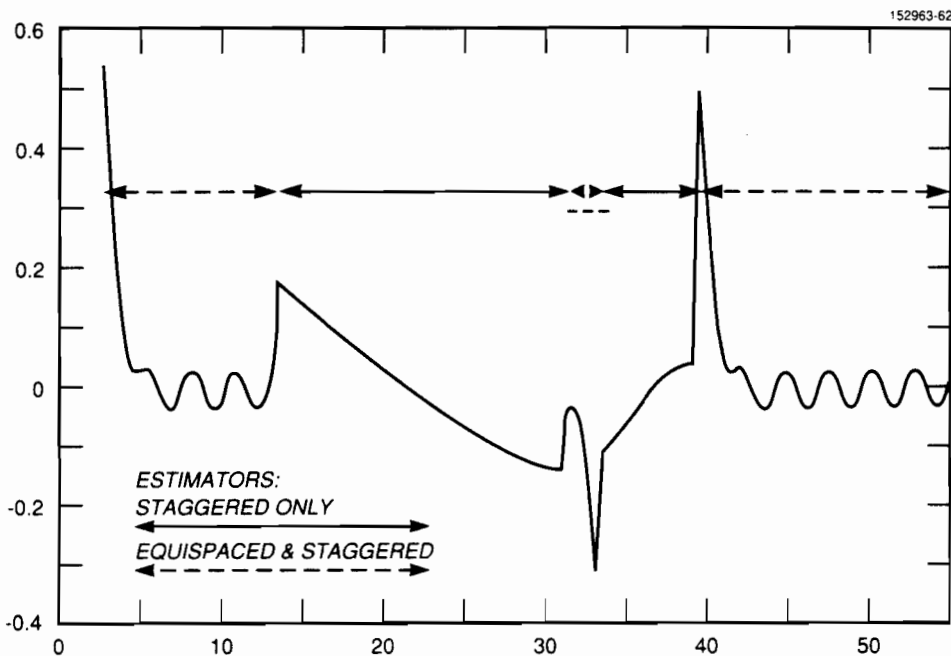


Figure 5.4: Combining staggered and equispaced velocity estimates



MEAN VELOCITY ESTIMATE ERROR (m/s) vs MEAN WEATHER VELOCITY (m/s)
 FILTER IDs: STAGGERED - 233, EQUISPACED - 3303

WEATHER SPECTRUM WIDTH IS 1.0 m/s
 MINIMUM DISPLAYED VELOCITY: 3.0 m/s
 δ_T IS 0.45455 ms
 RADAR FREQUENCY IS 3.000 GHz
 STAGGER RATIOS:
 STAGGERED FILTER - 2:3
 EQUISPACED DECIMATION RATE - 3

ESTIMATOR IS BASED UPON THE LAG
 ESTIMATE FROM THE SELECTED FILTER (S).
 STAGGERED TO EQUISPACED FILTERS POWER
 RATIO SWITCHING THRESHOLD: 1.10
 VELOCITY MODULUS LIMIT IS 65.0
 NYQUIST SPECTRAL FOLDING ENFORCED

Figure 5.5: Velocity estimate errors for composite filter of figure 5.2, $\sigma_v = 1$ m/s, $\log c_1$ and c_2 transfer functions replaced by $|G(\omega)|^2$

Appendix A: Gust Front Spectrum Width Data

A gust front is the leading edge of the outflow produced when a thunderstorm downdraft reaches the earth's surface and propagates horizontally. Early and reliable detection of gust fronts requires accurate Doppler measurements, as a gust front's initial reflectivity signature is often obscured by that of its parent storm [Klinge84a]. Table A.1 displays seasonal data on gust front spectrum widths from four regions East of the Rocky Mountains. All measurements were made within 100 km of the radar and are in units of m/s. The data displayed in the table are:

AvgAvg -

per-tilt average gust front spectrum widths, averaged over all tilts containing a given gust front, then averaged over all gust fronts in the region;

MaxAvg -

per-tilt maximum gust front spectrum widths, averaged over all tilts containing a given gust front, then averaged over all gust fronts in the region;

and **Peak -**

peak gust front spectrum width observed in a region.

Gust Front Spectrum Width Data								
Region and Source †	May-September				October-April			
	Number of Events	AvgAvg	MaxAvg	Peak	Number of Events	AvgAvg	MaxAvg	Peak
Memphis FL-2	12	N/M	4.7	N/M	0	-	-	-
Huntsville FL-2	7	2.1	3.4	5.5	5	2.5	4.3	5.5
NSSL [Klinge84a] ‡	6	5.6	9.7	15.0	4	6.6	11.1	13.0
Denver FL-2	11	2.8	4.0	6.0	0	-	-	-

TABLE A.1

† FL-2 is the FAA S-Band Doppler weather radar testbed; NSSL is the National Severe Storms Laboratory; N/M indicates that values were not measured by the storm analyst. The FL-2 data were compiled at Lincoln Laboratory by Paul J. Biron, Robert G. Hallowell, Mark A. Isaminger, J. Patrick Sanford and the author.

‡ Dr. Dusan Zrnić of NSSL indicates that these values may have a positive bias due to clutter contamination and the fact that the lag zero autocorrelation estimates used in computing NSSL's spectrum width display are not corrected for system noise.

The Memphis, Huntsville and Denver data are consistent in all three categories with an average AvgAvg value of 2.5 m/s and average MaxAvg value of 4.1 m/s. The overall peak value for those regions is 6 m/s. The magnitude of the bias, if any, in the NSSL data is unknown. And, if the NSSL measurements are accurate, such energetic gust fronts would likely contain high amounts of debris and hence possess prominent reflectivity signatures. We propose that reflectivity measurements along with accurate Doppler measurements for weather of spectrum widths up to 6 m/s will be sufficient for the detection of gust fronts.

References

Cadzow80a.

J.A. Cadzow, *Generalized Digital Matched Filtering*, IEEE Paper 00942898/80/00000307, 1980.

Doviak84a.

R.J. Doviak and D.S. Zrnić, *Doppler Radar and Weather Observations*, Academic Press, New York, 1984.

Evans83a.

J.E. Evans, "Ground Clutter Cancellation for the NEXRAD System," Lincoln Laboratory Project Report ATC-122, October 1983.

Fujita85a.

T.T. Fujita, "The Downburst: Microburst and Macrobust," University of Chicago Satellite and Mesometeorology Research Project, Chicago, 1985.

Harris78a.

F.J. Harris, "On the Use of Windows for Harmonic Analysis with the Discrete Fourier Transform," *Proceedings of the IEEE*, vol. 66, #1, pp. 51-83, January 1978.

Herrmann73a.

O. Herrmann, L.R. Rabiner, and D.S.K. Chan, "Practical Rules for Optimum Finite Impulse Response Low-Pass Digital Filters," *Bell System Technical Journal*, vol. 52, pp. 768-800, July-August 1973.

Jasik61a.

H. Jasik, "Fundamentals of Antennas," in *Antenna Engineering Handbook*, ed. H. Jasik, pp. 2-1 to 2-51, McGraw-Hill, New York, 1961.

Keeping78a.

K.J. Keeping and J.C. Sureau, "Control of Sidelobes in Cylindrical Arrays," Lincoln Laboratory Technical Note 1978-22, June 1978.

Klinge84a.

D.L. Klinge, "A Gust Front Case Studies Handbook," Lincoln Laboratory Project Report ATC-129, August 1984.

Mann86a.

D.R. Mann, J.E. Evans, and M.W. Merritt, *Clutter Suppression for Low Altitude Windshear Detection by Doppler Weather Radar*, 23rd Conference on Radar Meteorology, Snowmass, CO, September 1986.

Marden49a.

M. Marden, *The Geometry of the Zeroes of a Polynomial in a Complex Variable*, American Mathematical Society, New York, 1949.

Merritt87a.

M.W. Merritt, Personal Communication, Lincoln Laboratory, January 1987.

Miller70a.

K.S. Miller and M.M. Rochwarger, "On Estimating Spectral Moments in the Presence of Colored Noise," *IEEE Transactions on Information Theory*, vol. IT-16, #3, pp. 303-309, May 1970.

Nathanson69a.

F.E. Nathanson, *Radar Design Principles – Signal Processing and the Environment*, McGraw-Hill, New York, 1969.

Parks72a.

T.W. Parks and J.H. McClellan, "A Program for the Design of Linear Phase Finite Impulse Response Filters," *IEEE Transactions on Audio and Electroacoustics*, vol. AU-20, #3, pp. 195-199, August 1972.

Passarelli81a.

R.E. Passarelli, P. Romanik, S.G. Geotis, and A.D. Siggia, *Ground Clutter Rejection in the Frequency Domain*, 20th Conference on Radar Meteorology, Boston, November 1981.

Rinehart87a.

R.E. Rinehart, J.T. DiStefano, and M.M. Wolfson, "Preliminary Memphis FAA/Lincoln Laboratory Operational Weather Studies Results," Lincoln Laboratory Project Report ATC-141, April 1987.

Sirmans76a.

D. Sirmans, D.S. Zrnić, and W. Bumgarner, *Estimation of Maximum Unambiguous Doppler Velocity by Use of Two Sampling Rates*, 17th Conference on Radar Meteorology, 1976.

Skolnik80a.

M.I. Skolnik, *Introduction to Radar Systems, Second Edition*, McGraw-Hill, New York, 1980.

Thomas72a.

H.W. Thomas and N.P. Lutte, "Z-Transform Analysis of Nonuniformly Sampled Digital Filters," *Proceedings of the IEE*, vol. 119, #11, pp. 1559-1567, November 1972.

Thomas74a.

H.W. Thomas and N.P. Lutte, "Design of MTI Filters with Staggered PRF: A Pole-Zero Approach," *Proceedings of the IEE*, vol. 121, #12, pp. 1460-1466, December 1974.

Uyeda85a.

H. Uyeda and D.S. Zrnić, "Automatic Detection of Gust Fronts," Department of Transportation Report DOT/FAA/PM-85/11, April 1985.

Vasiloff84a.

S. Vasiloff, M. Istok, and R.J. Doviak, "Thunderstorm Phenomena and Weather Radar Scanning Strategies," National Severe Storms Laboratory, December 1984.

Wilk80a.

K.E. Wilk and J.T. Dooley, "FAA Radars and their Display of Severe Weather (Thunderstorms)," Department of Transportation Report FAA-RD-80-65, July 1980.

Witt87a.

A. Witt and S.D. Smith, *Development and Testing of the Gust Front Algorithm*, NOAA Environmental Research Laboratories, National Severe Storms Laboratory, Norman, Oklahoma, August 1987. Accepted for Publication by the Federal Aviation Administration

Zrnić79a.

D.S. Zrnić, "Estimation of Spectral Moments for Weather Echoes," *IEEE Transactions on Geoscience Electronics*, vol. GE-17, #4, pp. 113-128, October 1979.